SALT ROCK DEFORMATION AND EVOLUTION: DAMAGE DEVELOPMENT AND HEALING IN ROCK SALT

MSc Thesis by V. Donadio

Utrecht University

Faculty of Geosciences

October, 2017

Abstract

Rock salt formations have already proven to be excellent caprocks for containing gas and oil over geological timescales. Upon mechanical damage, the high ductility of salt formations ensures that porosity and permeability evolve to very low values over time (e.g. Hunsche and Hampel, 1999). In addition, fluid-assisted diffusive mass transfer processes, such as dissolution-precipitation and recrystallization processes, further reduce pore-connectivity and permeability, ensuring healing and sealing (Houben et al., 2013). This self-healing capacity could potentially make rock salt caverns ideal storage locations for compressed air, hydrogen, natural gas and nuclear waste. However, damage induced during salt mining may impact cavern sealing integrity, forming a permeable zone in witch porosity will increase due to microcracking.

The aim of this project is to investigate crack evolution and healing properties to predict the timescale at which cracks will close again, and by which processes, to guarantee the safety of the storage.

Microstructure analysis on intact and damaged rock salt provides an overview of the different deformation mechanisms that might affect rock formations. The starting material is characterized by a dilatant behaviour in which intergranular cracks and triple junctions are dominant; while at high confining pressure salt rock undergoes non-dilatant behaviour at in which recrystallization processes might modify the entire microstructure. The material deformed at low confining pressure provides information about the transitional phase between dilatant and non-dilatant behaviour, showing both dislocation structures and recrystallized grains over relict of old ones.

Measurements of seismic velocities under compression and time-lapse X-ray tomography are used to monitor the microcracks evolution and healing. Compression experiments on Beberthal sandstone are done as control experiment to assess if crack density and fracture network can be quantified by wave velocities measurements under triaxial compression and then used on salt rock. The experiment represents a great tool to analyse crack evolution, and consequently healing, by monitoring the change in seismic velocities and therefore an in-depth analysis is suggested, but could not be executed due to time-constraints.

CT-scanning imaging are done on compacted aggregates of granular rock salt to monitor cracks and investigate its healing, without induce damage to the sample. Prior to the experiment, a theoretical model is derived in this study to predict the healing behaviour of microcracks that contain a fluid film at the crack surface. A comparison between the samples scanned at different days show differences in crack size and evolution, confirming that healing processes occurred during the time. The quantitative crack measurements on sample VD14 (2 and 3 days exposure of cracks to brine) are eventually compared with the theoretical data on the progress of crack healing obtained using different values of diffusion coefficient and thickness of the fluid film. In some cases quantitative results show lower values of crack healing then the theoretical values obtained using 1,96E-22 as value for DCδ/a (found

using D= 10E-9 m^2/s and δ= 280E-9 m from Houben et al., 2013) and are more similar to the ones obtained using a value of 7,00E-25 for DCδ/a (found using D= 10E-18 m^2/s and δ= 1E-9 m from Koelemeijer et al., 2012); this is probably due to a different thickness of the fluid film at the crack surface. Further research is suggested to estimate and predict with more precision the evolution of cracks in salt rock.

Table of contents:

1. Introduction

Rock salt is a sedimentary rock that forms in arid climates from the evaporation of oceans and saline lake waters. Salt formations have four major characteristics (Wong et al., 2007):

- Due to high sedimentation rates, they often form thick layers;
- They deform plastically;
- Their porosity is very low, generally less than 1%, with permeability ranging between 10^{-7} and 10^{-4} mD ($9.869\ 10^{-23}$ m^2 and $9.869\ 10^{-20}$ m^2);
- They have a high density near the surface, lower below 500m.

Its low permeability and its potential for healing/sealing due to its ductile rheological properties (Houben et al., 2013), make rock salt an excellent seal for hydrocarbon reservoirs and it could potentially represent a good storage location for compressed air, hydrogen, natural gas and nuclear waste. However, the integrity of salt rock formations might be damaged during the construction of a disposal site. In fact, mining processes disturb the original stress equilibrium of the rock leading to the formation of a permeable zone known as the excavation damaged or disturbed zone (EDZ or EdZ) (Houben et al., 2013), in which the hydraulic and mechanical properties of salt rock change leading to increase in porosity and permeability due to the development of micro-cracking. The EDZ results to be the area in which occurs a redistribution of the in situ stresses and reorganization of rock structures (Tsang et al., 2004). Furthermore, Tsang at al., describing the geohydromechanical processes in the zone directly adjacent to the excavated volume, make a distinction between the excavation disturbed zone (EdZ) and the excavation damaged zone (EDZ), defining the first as "a zone with hydromechanical and geochemical modifications, without major changes in flow and transport properties" and the second as "a zone in which hydromecanical and geochemical modifications induce significant changes in flow and transport properties" (i.e. increase in permeability). The consequently fracture creation and propagation might undermine the sealing property of the formation and lead to potential leakage; and, according to their study, this effect in the EdZ could be important for the long-term period, while in the EDZ could be significant only in the short period due to the self healing property of rock salt.

It is clear that the understanding of the mechanical behaviour of salt rock and its integrity in this zone is crucial for long-term storage.

1.1. Dilatancy boundary and creep behaviour

Rock salt deforms plastically without the formation and propagation of dilating cracks as long as the state of stresses remains within the non-dilatant stress domain (Schulze et al., 2001). However, when rock salt is mechanically loaded, it can deform within two different stress-dependent domains (Schulze et al., 2001): compaction and dilatancy (Figure 1). These domains are separated by the dilatancy boundary at which point there is almost no change in volume. For stress states below the dilatancy boundary (compaction domain) micro-cracks are compacted and closed (Hunsche and Hampel, 1999; Schulze et al., 2001), leading to a decrease of permeability. On the other hand, with the increase of stresses, above the boundary, the volume of the rock would increase due to micro-cracks opening, leading to a consequently increase in permeability and decrease in seal capacity. In addition, the micro-acoustic emission rate increases above the dilatancy boundary and seismic wave velocities decrease (Hunsche and Hampel, 1999). Figure 1 shows differential stress versus confining pressure obtained from a strength test using the V_s maximum as indicator for the dilatancy boundary (Schulze et al., 2001). The study also indicates that, under compressional loading, microcracks are aligned almost parallel to the compression axis and vice-versa under extensional loading.

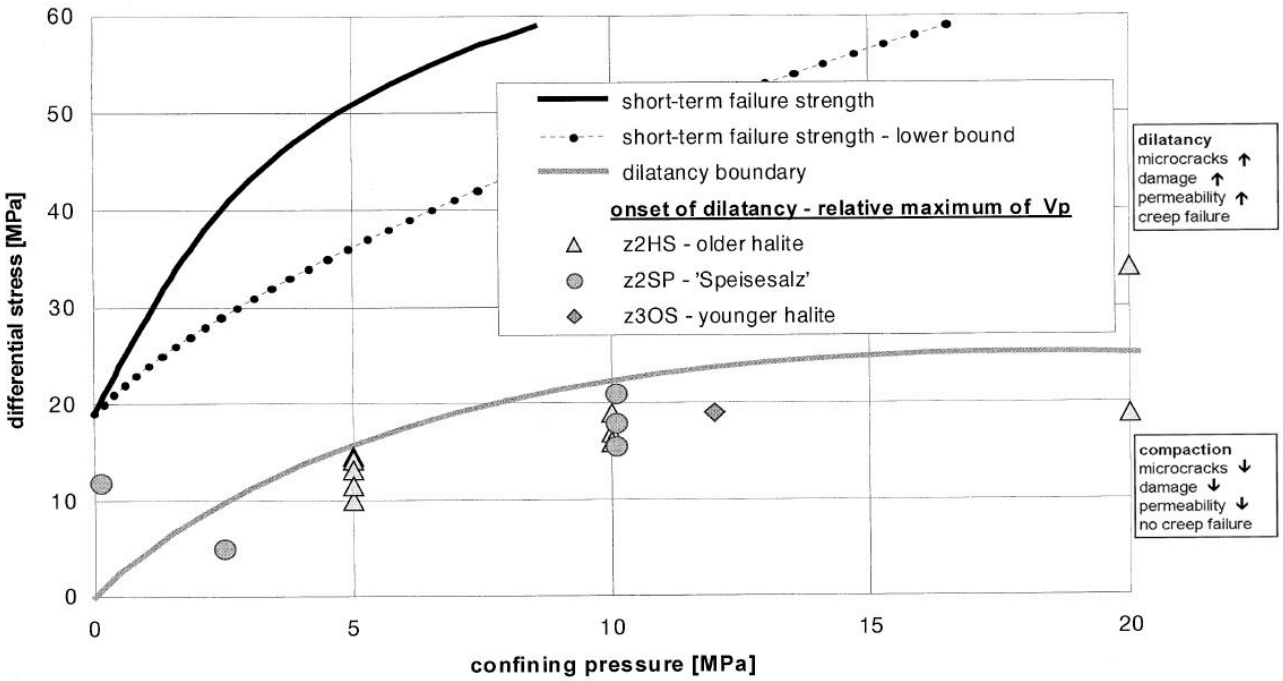

Figure 1: Dilatancy boundary in rock salt. Strength test in compressional mode at 30°C, confining pressure of 5 MPa and axial strain rate 10^{-5} s^{-1} (modified from Schulze et al., 2001).

In previous studies, fundamental importance is given to the dilatancy boundary and creep behaviour of rock salt. Alkan et al. (2007) investigate the dilatancy boundary combining compression tests and acoustic emission measurements, obtaining consistent results in both of the cases. The stress-strain behaviour is described in five stages (Figure 2):

- Stage 1: visco-elastic deformation: closure of primary pores and cracks with increasing compaction (reversible stage);
- Stage 2: elastic deformation: linear increases in the axial and volumetric strains;
- Stage 3: brittle-ductile transition, crack initiation: the cracks begin to open and grow, high increase of axial strain;
- Stage 4: brittle-ductile transition, damage initiation: point of maximum compression, permanent damage;
- Stage 5: plastic behaviour: increase of volumetric strain, visco-plastic behaviour of the rock salt.

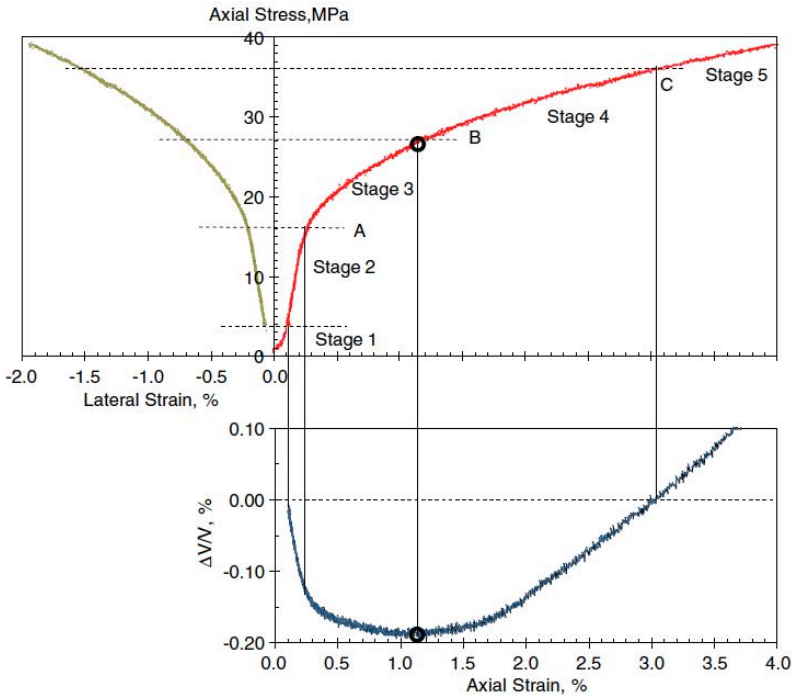

Figure 2: Stress-strain behaviour for rock salt deformed at restored in situ temperature and axial stress up to 40 MPa with an axial strain rate of $1x10^{-5}$ min^{-1} to simulate the effect of excavation of the salt mine (Alkan et al., 2007).

Differently from Schulze at al. (2001) who consider the dilatancy boundary independent from loading rate, loading geometry or type of rock salt, Alkan et al. (2007) confirm the dependence of the dilatancy boundary on stress loading rate and pore pressure. According to their study, the value for dilatancy boundary slightly decreases with increasing the loading rate and dilatancy is accelerated by high pore pressure.

1.2. Microcracks development and crack healing

Rock salt consists of halite grains of various size and texture. At in situ conditions, cracks are mostly closed, but during deformation microstructural processes can modify the equilibrium of the rock salt.

So that, the grain boundaries may open under the applied differential stress creating a potential pathway of discontinuities, especially if connected between each other. A study of the microcrack network development under triaxial compression (Ding et al., 2017) demonstrate that, at room temperature and low confining pressure, grain boundary microcracking results the dominant brittle deformation mechanism and tends to develop sub-parallel to the loading direction. At sufficiently high deviatoric stress, rock salt undergoes a semi brittle behaviour and with increasing stress crystal plasticity represents the dominant deformation mechanism (Urai et al., 2008; Urai and Spiers, 2007)
Furthermore, the presence of fluid films within the grain boundaries could enhance deformation processes. In fact, fluid films not only facilitate solution, precipitation and diffusion processes, but enhance recrystallization at the grain boundaries (Heege et al., 2005). At the same way, microcracking disrupts grain boundary films and restrains both migration and solution-precipitation. (Urai et al., 2008). In the case of deformation by solution-precipitation creep, in presence of fluid films within the grain boundaries, grains dissolve at the boundaries and the material is transported along the wall; after diffusion, the material crystallizes at interfaces under low normal stress (Hackl and Ilić, 2005; Urai & Spiers, 2007). The transport of precipitated material through the fluid film represents one of the healing mechanisms in rock salt. In fact, according to Houben et al. (2013), crack healing and sealing can occur by three different physical mechanisms:

- Mechanical healing due to compaction of the bulk rock by elastic deformation or plastic flow;
- Diffusive healing by diffusion of transported material through the fluid film;
- Crack healing by recrystallization.

Mechanical healing is expected to dominate in the early stages after the final waste disposal, when the normal stress is high (Liedtke and Bleich, 1985, Koelemeijer et al., 2012) and could be enhanced by the presence of brine. In fact, according to Liedtke and Bleich (1985) adding brine (3 wt%) and using high loads (up to 70 MPa), mechanical healing can occur until around 30 days. While diffusive healing is expected to be important in the longer term (Houben et al., 2013). Crack healing by recrystallization involves the migration of pre-existing grain boundaries (occurring in condition of high temperature or presence of fluid film at the boundary) and their new formation leading to a modification of the microstructure (Drury and Urai, 1990; Chen et al., 2013).
Thanks to the natural healing properties of rock salt, cracks will progressively disconnect leading to a consequently decrease in permeability, therefore it is key to be able to predict the timescale at which the healing process will occur and by which processes.

1.3. Objectives and approach

The aim of the project is to study the self-healing capacity of rock salt in the presence of brine. To that end, the development of micro-cracks by brittle processes and consequently the healing capacity of by mass transfer processes are investigated. The project is focused on how fast the self-healing can occur in damaged salt and if it is possible to quantify the rate of such healing using CT-scan imaging.

Wave velocity measurement under triaxial compression on sandstone were made as a control experiment for rock salt at the Christian-Albrechts University of Kiel (collaboration with Dr. H. Bahadur Motra). Microstructural analysis was performed by using conventional optical (thin section) imaging, followed by time-lapse X-ray tomography to study the evolution of the healing process.

2. Typical microstructure observed in intact and damaged rock salt

To understand the impact of deformation on crack formation in rock salt, microstructural analysis were performed on undeformed and deformed samples of Speizesalz. For the deformed samples, one low confining pressure (3 MPa) and one high confining pressure (30 MPa) sample was selected. Together the samples are representative for the type of deformation one would expect in an EDZ and the undisturbed host formation.

Thin sections of Speizesalz rock salt were analysed with the Leica microscope by using both reflective and transmitted light. The first thin section represents undeformed rock salt taken 231-251 cm from the mine wall into the salt formation, the second rock salt deformed at 3 MPa effective confining pressure (i.e. representative for the EDZ close to the excavation point) and the last deformed at 30 MPa effective confining pressure (i.e. representative for the EDZ away from the excavation point).

2.1. Undeformed material (B5-4C-5-2)

Images in reflected light show halite grains from subidiomorphic to irregular with a size around 3-10 mm and irregular grain boundaries. Figure 3a shows irregular halite grain (in white) and grains with impurities (in greyish). Grain boundaries are characterized by fluid inclusions of few micron diameter and weak subgrain structure is visible around the grains (Figure 3a-b).

In general, fluid inclusions are present at the grain boundaries in the whole thin section (around 80%), Figure 3c-d, with overprints of fluid inclusions of what seem to be an old grain boundary in 3c. The section presents a different development of subgrain structures at the scale of microns, Figure 3e-f shows some subgrain development, while in 3c the subgrain structure is poorly developed. In general the subgrain structure appears to be free from inclusions.

Some areas of the thin section present grain boundaries triple junction, some of them intersecting at 120° (Figure 3g) and intergranular cracks (Figure 3h).

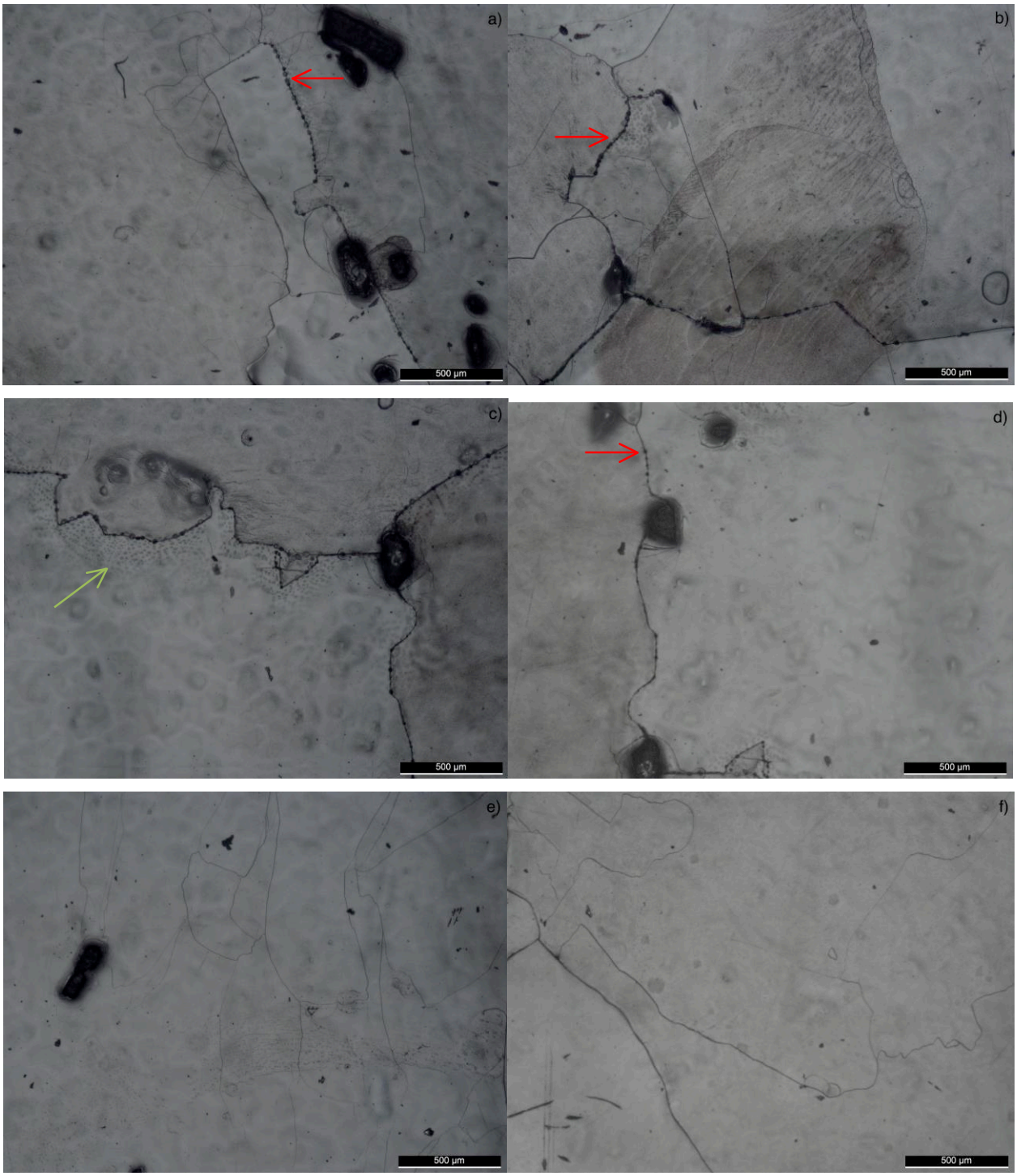
a)
500 µm
b)
500 µm
c)
500 µm
d)
500 µm
e)
500 µm
f)
500 µm

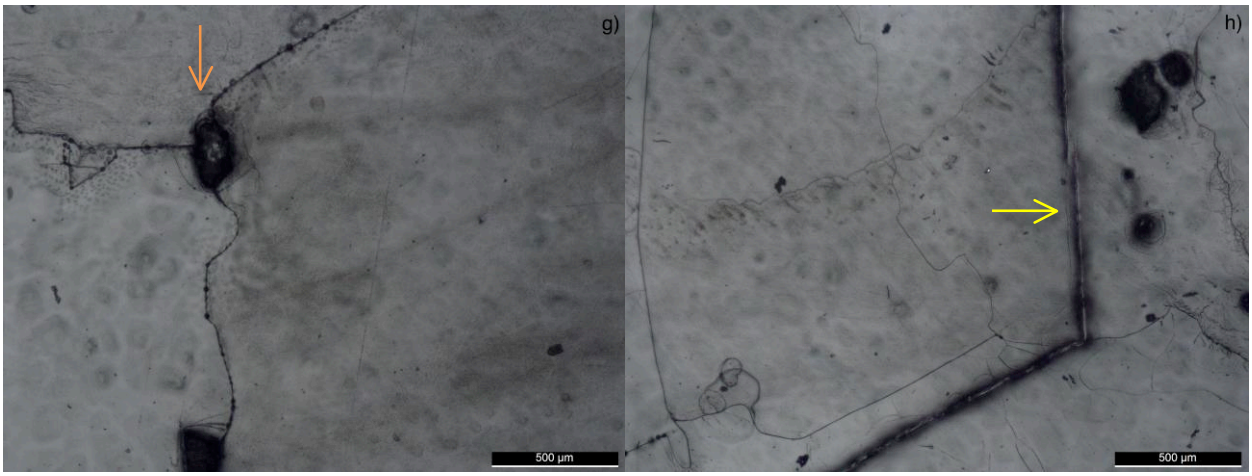

Figure 3: Reflected light, undeformed rock salt (B5-4C-5-2). a) Halite grain with fluid inclusions at the grain boundary (red arrow); b) fluid inclusion at the grain boundary and weak subgrain structure; c) overprints of fluid inclusion near the grain boundary (green arrow); d) subgrain structure almost absent; e-f) subgrain structure well developed; g) 120° triple junction (orange arrow); h) intergranular crack (yellow arrow).

In transmitted light fluid inclusions are clearly visible not only at the grain boundaries but also within the grains. In some cases, grain boundaries separate a fluid-rich crystal to a fluid-free crystal, as shown in Figure 4a, where a grain with no fluid inclusion is in contact with fluid-rich crystals by a lobate-shaped grain boundary. The subgrain structure seems well developed in the whole 4a, while in other cases it is absent in the fluid-free grains (Figure 4b-c). In general, fluid inclusion have the shape of 'bubbles' or tubes, some of them aligned in bends, especially along grain boundaries, while other seem to form a network of parallel bends (Figure 5-6). Intergranular microcrack is visible in Figure 5.

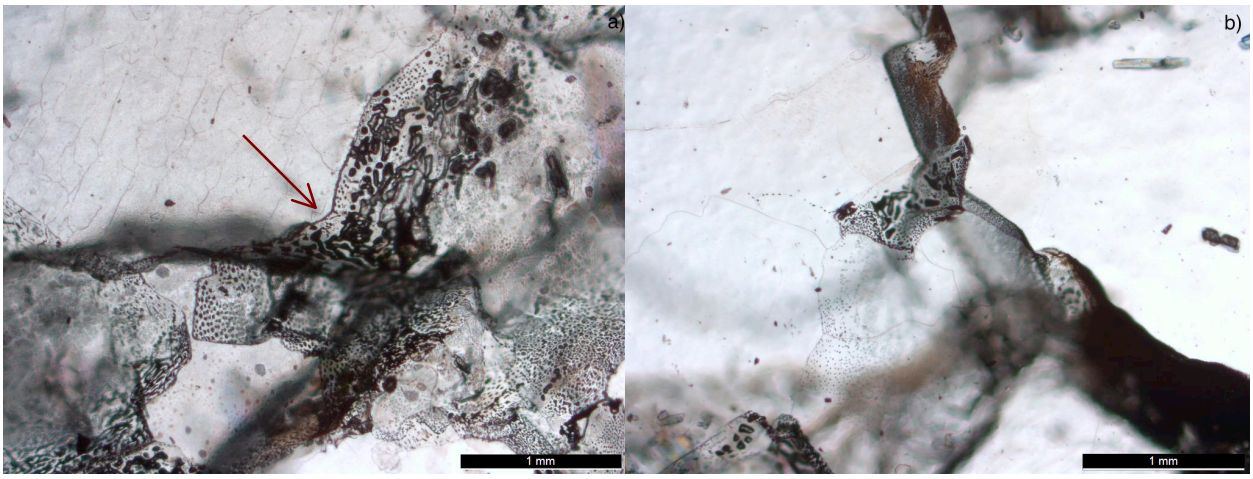

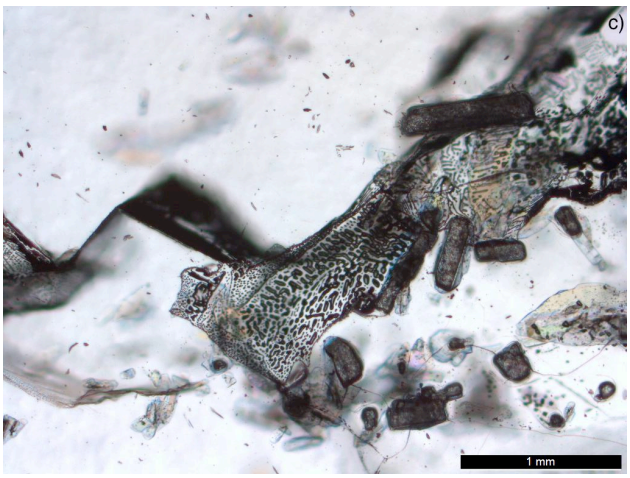

Figure 4: Transmitted light, undeformed rock salt (B5-4C-5-2). a) Grain boundary (brown arrow) that separate a fluid-free crystal (on the top) from a fluid-rich crystal (on the bottom); b) 'bubble'-shaped fluid inclusions; c) tubular-shaped fluid inclusion.

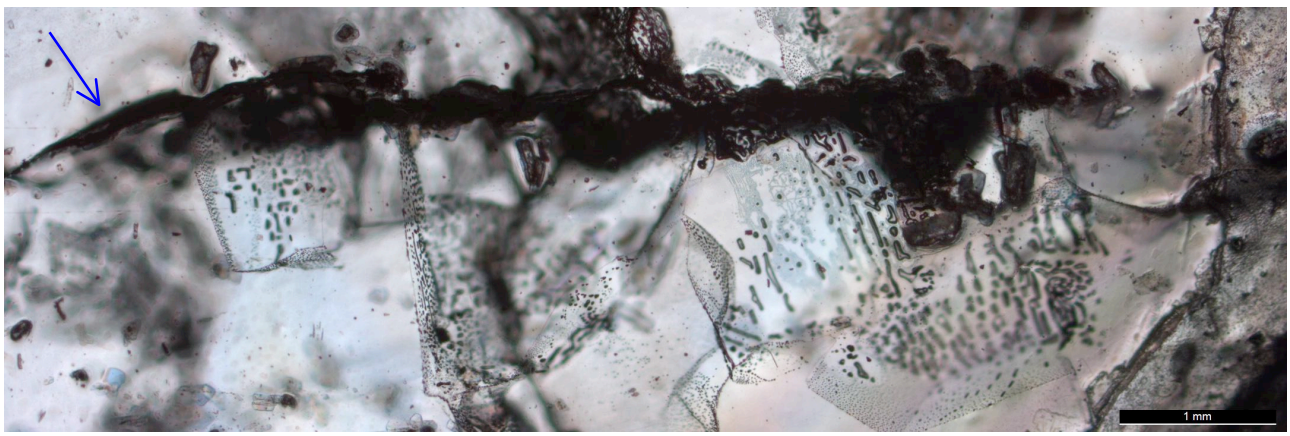

Figure 5: Parallel bend-shaped and tubular-shaped inclusions, intergranular crack (blue arrow), undeformed rock salt (B5-4C-5-2)

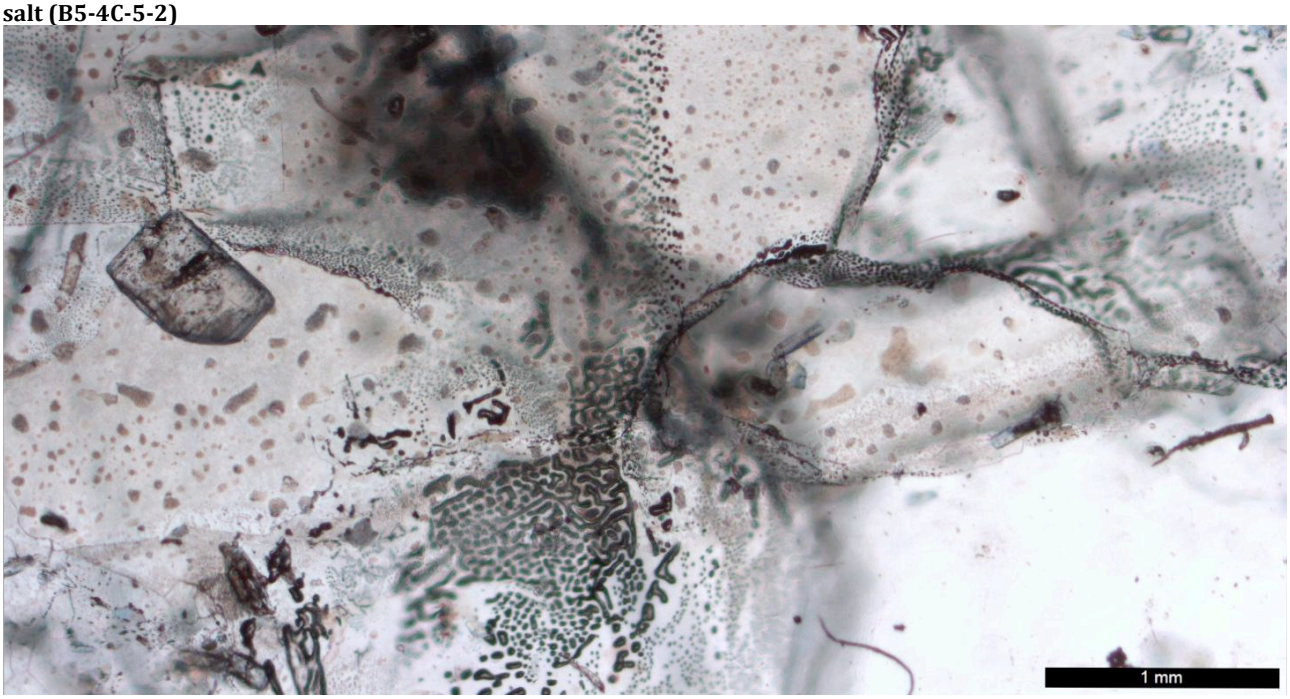

Figure 6: Fluid inclusions along grain boundaries, undeformed rock salt (B5-4C-5-2). Note the network of tubular and 'bubble'-shaped inclusions.

2.2. Material deformed at low effective confining pressure (SP205-1)

In reflected light the microstructure of rock salt deformed at low confining pressure (3 MPa) appears to be similar to the undeformed material, halite grains are irregular and subgrain structure is noticeable, but in this case it is strongly developed. Subidiomorphic grain of halite surrounded by fluid inclusions at its grain boundaries is shown in Figure 7a. Subgrain structure is well developed especially in the areas near the boundary and the left boundary seems dilated in respect to the rest. Well developed subgrain structure along the grain boundaries is visible in other areas of the thin section, where the boundaries are filled with fluid and dilation is noticeable on the top right side and on the left side (Figure 7b) and top right and top left side in Figure 7c.

Grain boundaries result irregular and in some cases intersect at 120° triple junction, as in 7d-e; in 7d note the presence of fluid inclusions in the crack on the right border (bright side), while on the left border (dark side) the crack does not contain fluid and results dilated. Moreover, some areas present dark bends of intergranular cracks within halite crystals with well-developed subgrain structures (Figure 8). The subgrain structure is not uniform in the whole thin section, as in the case of Figure 9 where a halite crystal (subgrain structure-free) is surrounded by grains in which the subgrain structure is strongly visible.

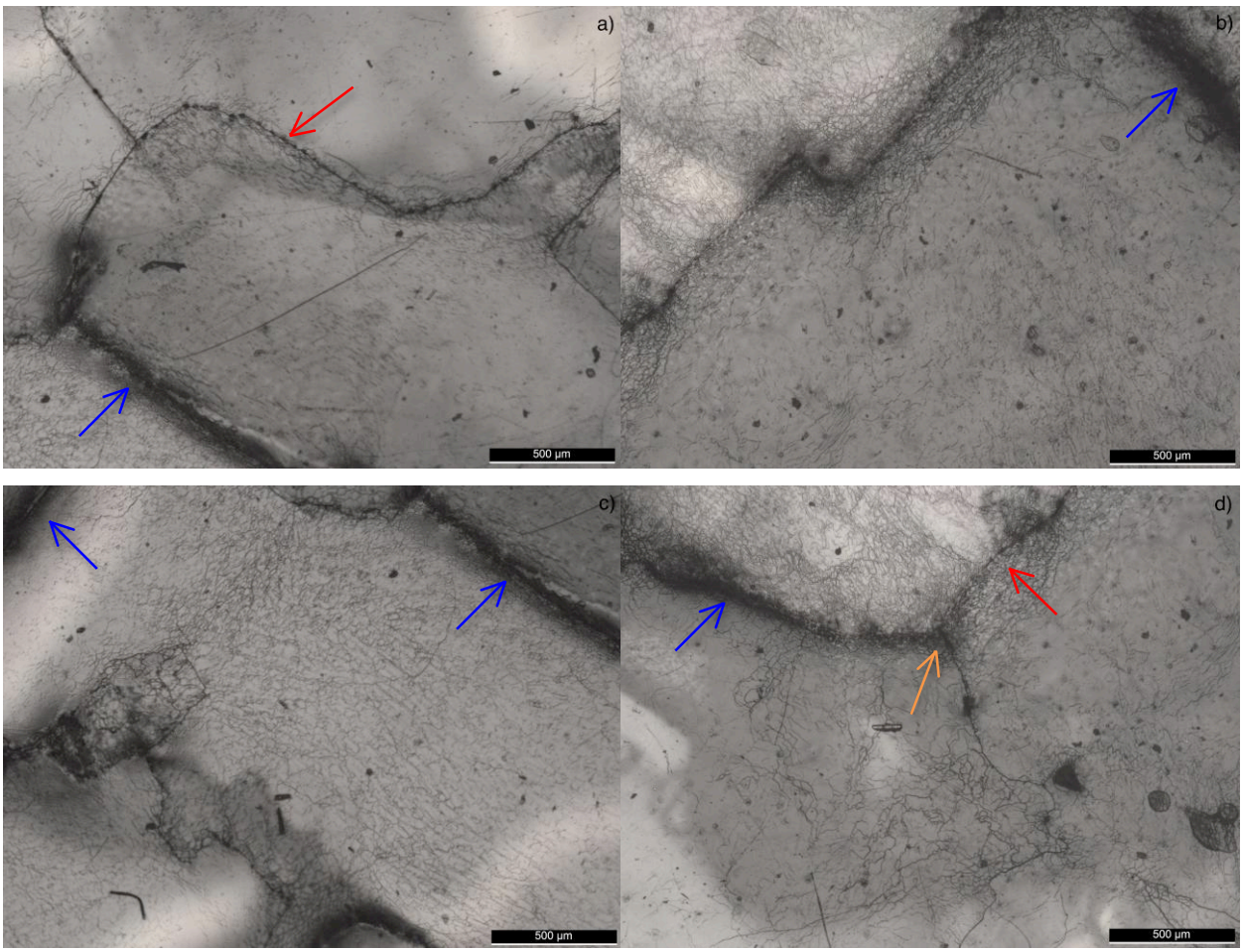

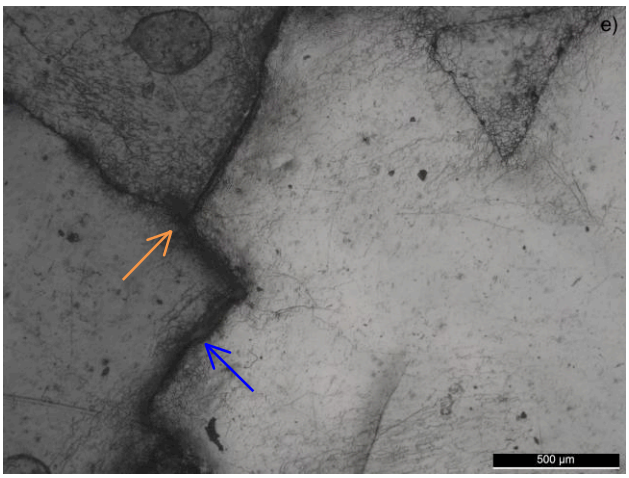

Figure 7: Reflected light, deformed rock salt (SP205-1). a) Subidiomorphic grain of halite with fluid inclusions (red arrow) and dilation (blue arrow) at the grain boundary; b) Well developed subgrain structure and dilation (blue arrow); c) Well developed subgrain structure and dilation (blue arrows); d) 120° triple junction (orange arrow), dilation at the grain boundary (blue arrow) and fluid inclusions (red arrow); e) triple junction (orange arrow) and dilation (blue arrow).

Figure 8: Reflected light, intergranular crack (yellow arrow) and well developed subgrain structure, deformed rock salt (SP205-1).

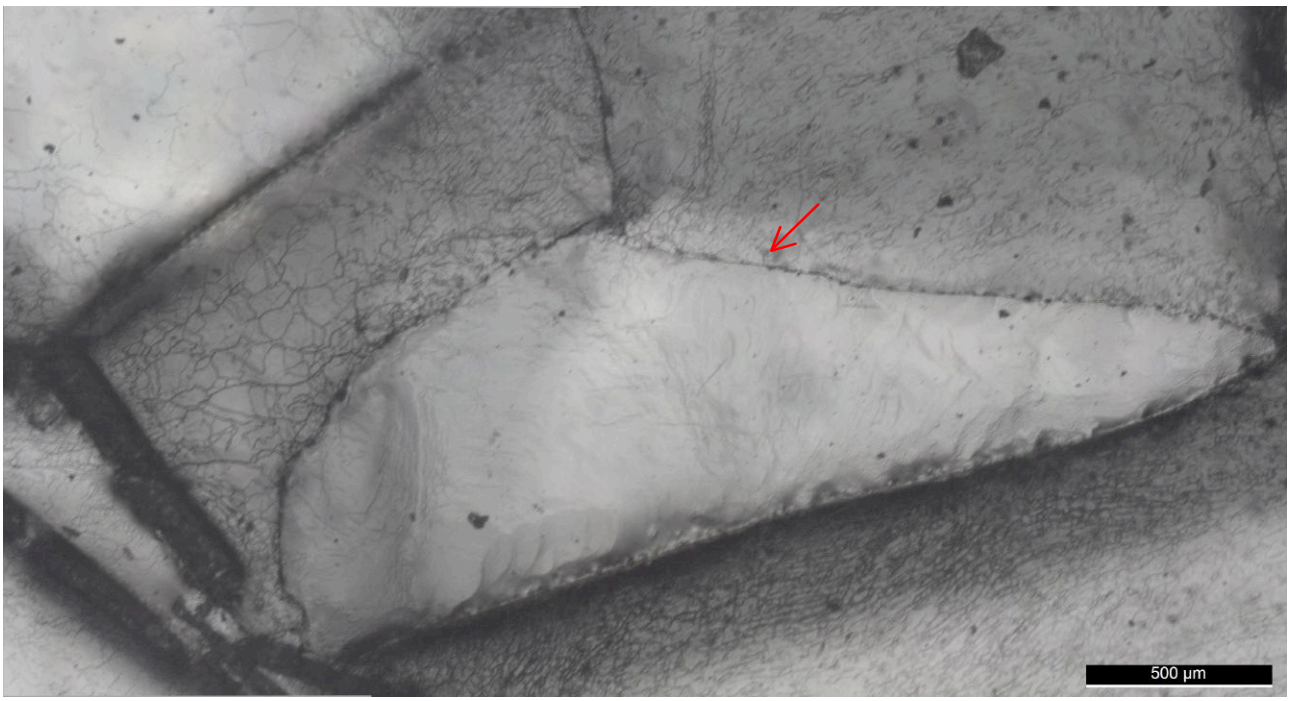

Figure 9: Reflected light, deformed rock salt (SP205-1). Halite crystal surrounded by grains with well-developed subgrain structure; note fluid inclusions at the halite boundary (red arrow).

Transmitted light shows a network of dark dilated cracks along the grain boundaries, not present in the undeformed material (Figure 10-11). Fluid inclusions are not visible as in the previous thin section, and in the whole section cracks result dilated. In addition, intergranular microcracks are still visible (Figure 12).

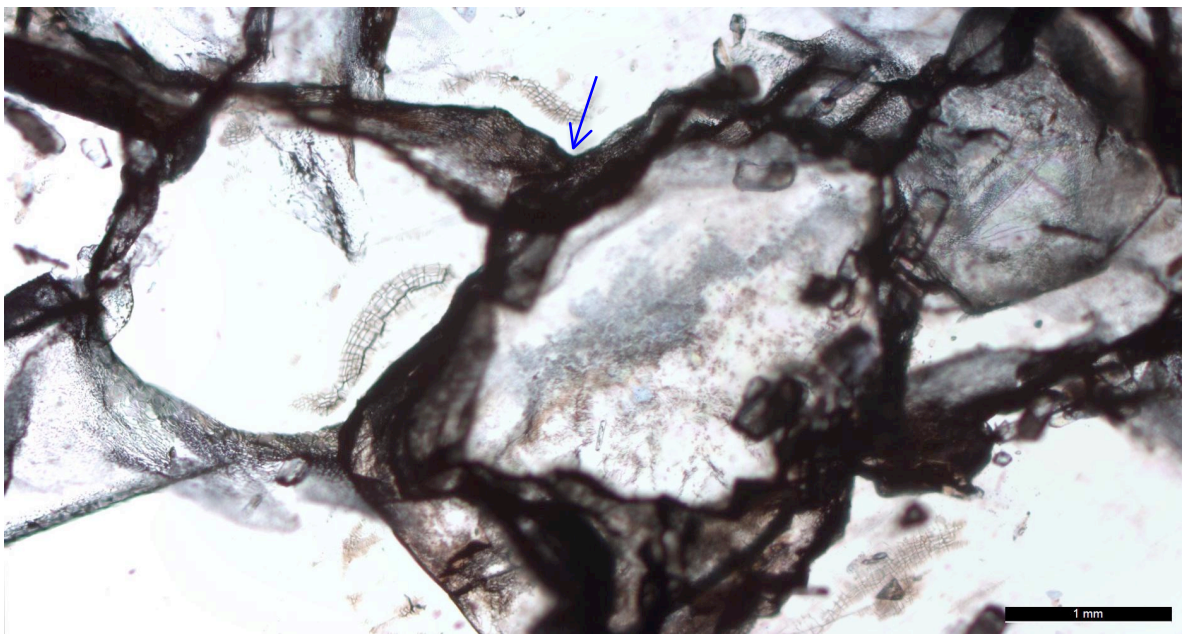

Figure 10: Transmitted light, dilation of cracks at the grain boundaries (blue arrow), deformed rock salt (SP205-1).

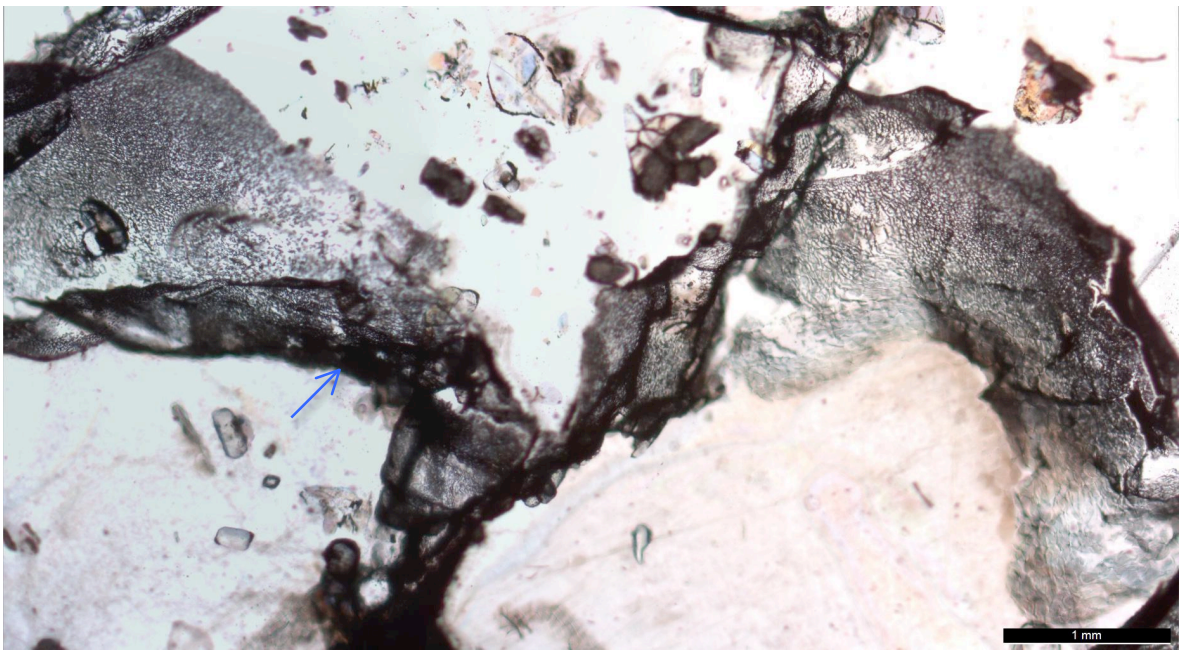

Figure 11: Transmitted light, dilation of cracks at the grain boundaries, deformed rock salt (SP205-1).

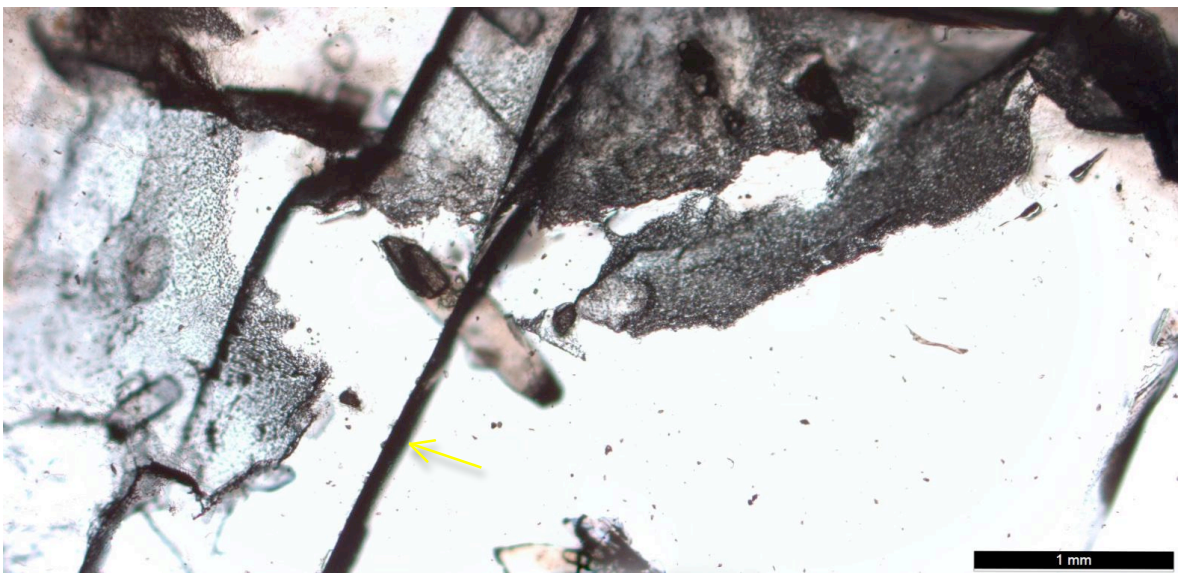

Figure 12: Transmitted light, intergranular cracks (yellow arrow), deformed rock salt (SP205-1).

2.3. Material deformed at high effective confining pressure (SP203)

In reflected light material deformed under high confinement (30 MPa) shows a different microstructure compared to the previous two, especially to the undeformed material. Grains appear very irregular, with sharp boundaries and subgrain development is not uniform everywhere (Figure 13), in some areas it is well developed and in others almost absent (Figure 14). Less fluid inclusions are present at the grain boundaries and some of them seem to be within the grains in the form of overprint, probably representing an old grain boundary (Figure 15). In general, it seems that older grains have been replaced by new recrystallized grains and intergranular microcracks are absent in

the whole thin section. At some grain boundaries we can notice dilation of the crack that result dislocated and empty, meaning that the fluid escaped (Figure 16).

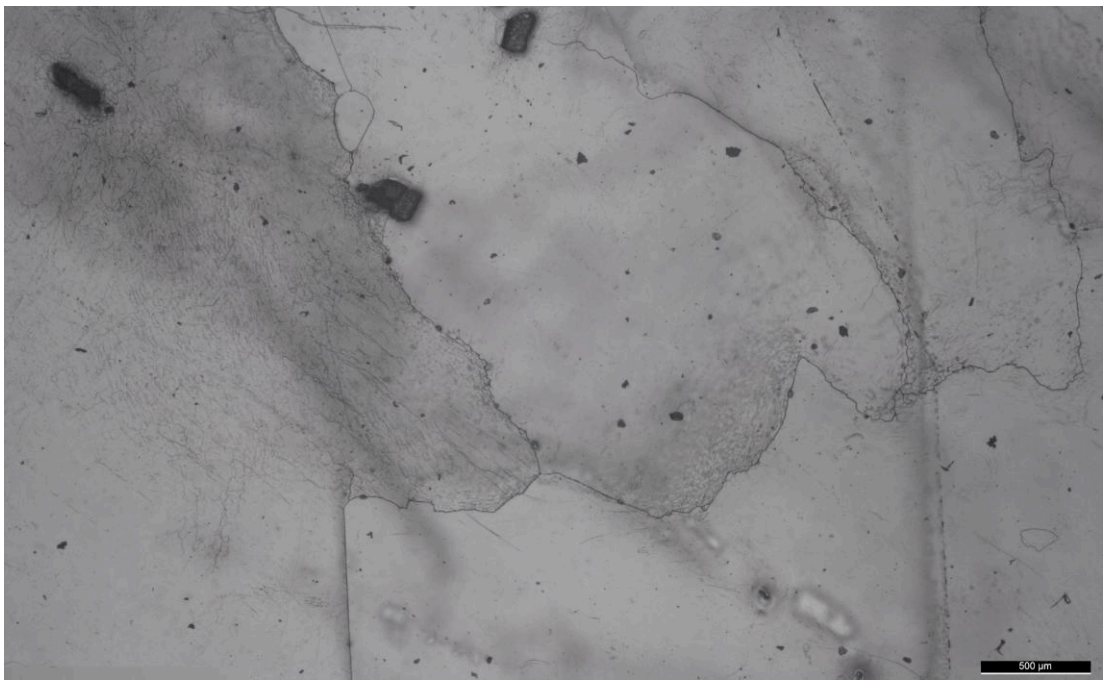

Figure 13: Reflected light, irregular grains with sharp boundaries and different evolution of subgrain structure, well developed on the left side; deformed rock salt (SP203).

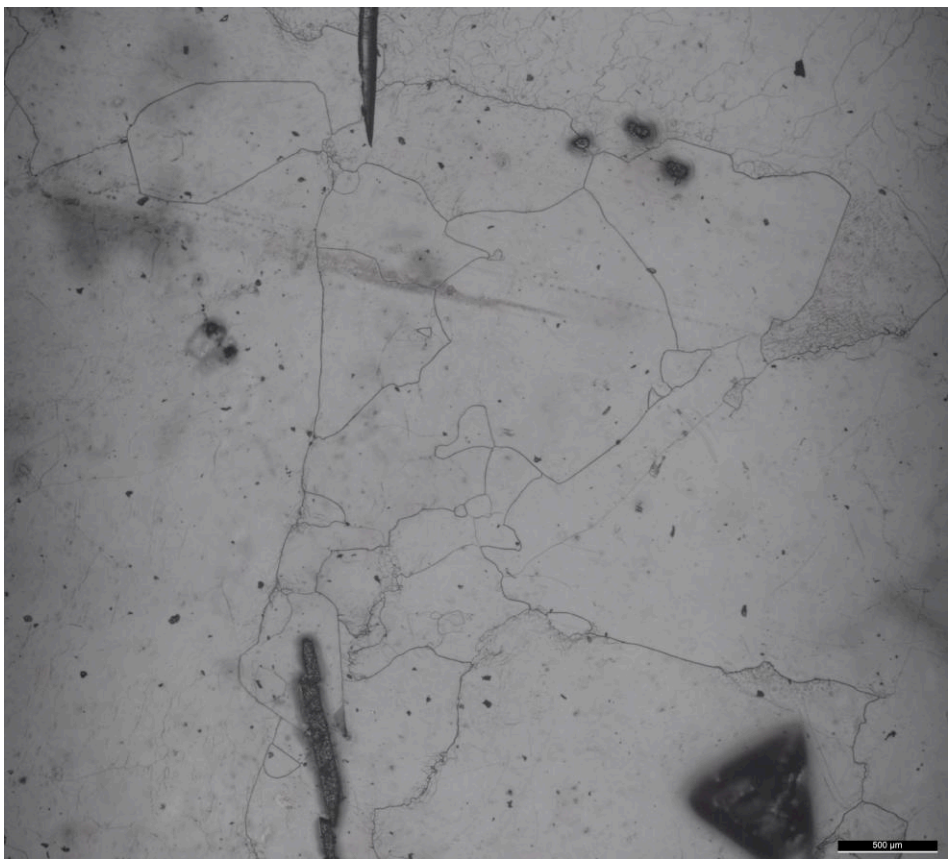

Figure 14: Reflected light, subgrain structure, deformed rock salt (SP203).

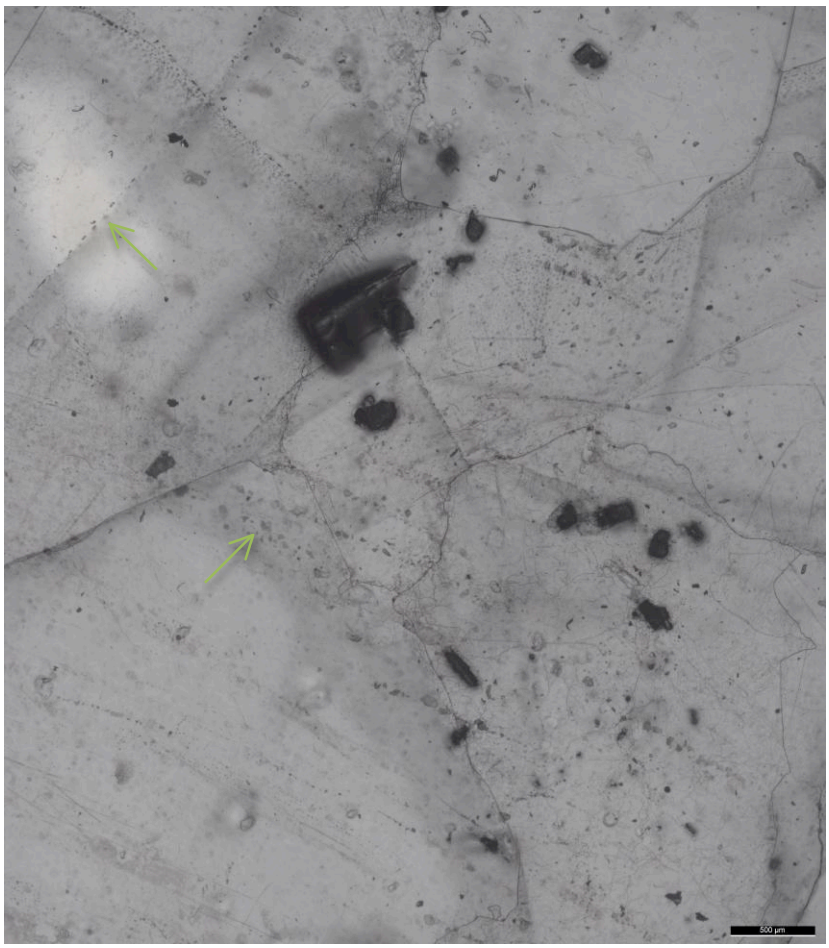

Figure 15: Reflected light, irregular grains with overprint of inclusions within the grain (green arrows), deformed rock salt (SP203).

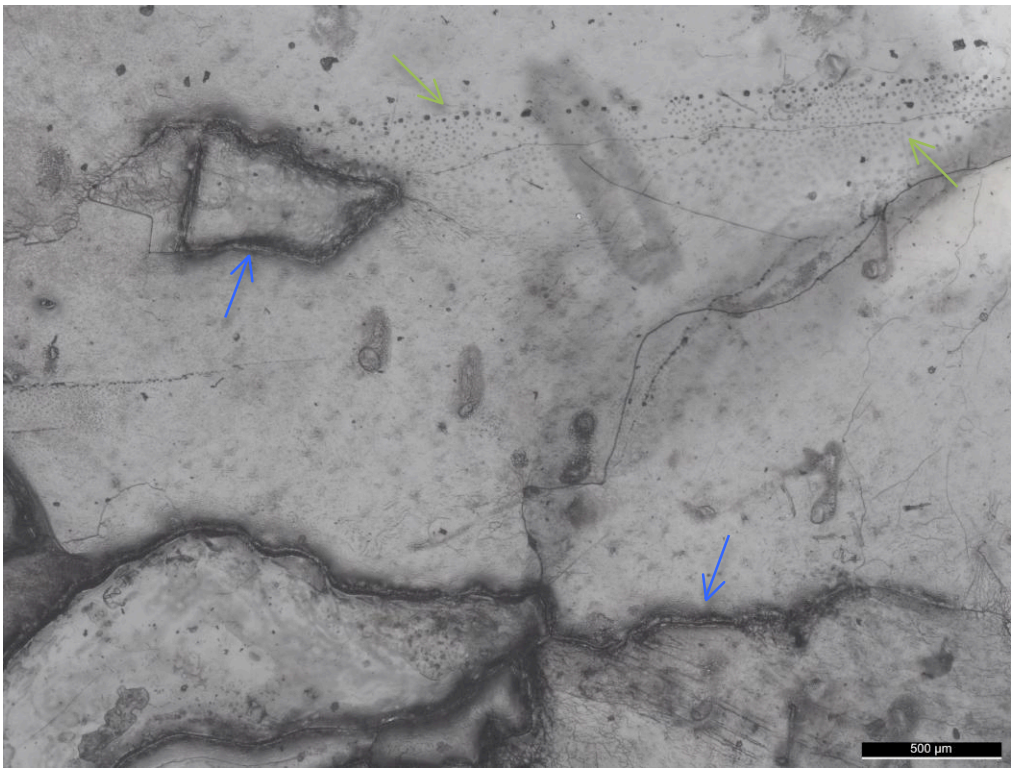

Figure 16: Reflected light, irregular grains with dilated cracks at the grain boundaries and overprint of inclusions within the grains (green arrows), deformed rock salt (SP203).

Transmitted light confirms what seen in incident light, note the absence of a network of inclusions, differently from the starting material. The section does not show intergranular cracks, while few fluid inclusions are still visible (Figure 16a-b-c).

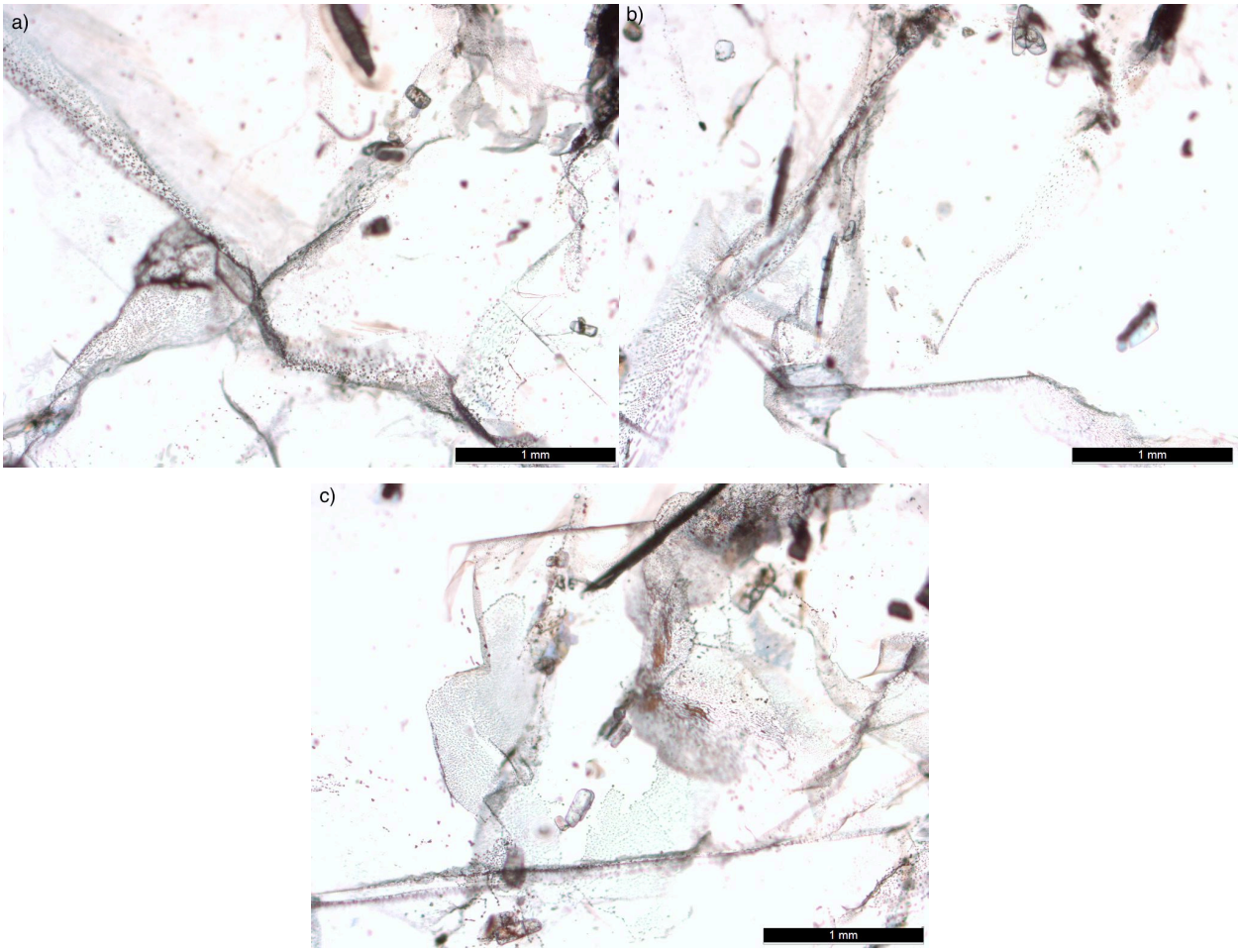

Figure 17: Transmitted light, deformed rock salt (SP203). Note the absence of intergranular cracks.

2.4. Summary of observations

The thin sections give an overview of the deformation mechanisms that might occur in rock salt under different state of stress. The starting material is characterized by fluid inclusions in almost the whole section that form a network within the grain boundaries. This network is rare or almost absent in the material deformed at 3 and 30 MPa in which fluid inclusions are noticeable, but they do not show a pattern. In particular, in the material deformed at 30 MPa fluid escaped and as consequence cracks seem empty and dilated. The subgrain structure results weak in the starting material and it is strongly developed in both of the deformed material. The presence of intergranular cracks and triple junctions at the grain boundaries (i.e. dislocation structures) is clearly visible in the starting material, while the material deformed at high confining pressure

shows evidence of recrystallization process with modification of the microstructure and overprints of inclusions showing grain boundary migration. The material deformed at low confining pressure is characterized by both intergranular cracks/triple junctions and new recrystallized grains/overprints of inclusions, meaning that the section might represent a transition between the undeformed material and the material deformed at 30 MPa. Previous studies (Spiers et al., 1986; Peach at al., 2001), define this behaviour a transition from a dilatant behaviour (starting material) to a non-dilatant behaviour, as seen in the thin section deformed at 30 MPa.

3. Monitoring microcracking using wave velocities: Control experiment on Beberthal sandstone

To assess the development of microcracks in dry rock salt and the progressive healing with time upon the addition of NaCl-saturated brine, we planned to perform acoustic measurements (P- and S-wave velocities, acoustic emission) under triaxial compression on 5x5x5 cm cubes of rock salt. The experiments consist in mainly two steps. First, compression under 3D stress will damage the samples and the crack development will be monitored by acoustic velocity measurements. To that end, hydrostatic stress representative for 1-2 km depth (50-75 MPa) will be applied to the samples, while tracking V_p-V_s velocities during all stress steps; then the stress will be reduced in one direction until zero to induce crack damage. The second step includes three different experiments:

- Increase the stress again to the original value to inspect mechanical closure and healing;
- Unload and saturate with fluid;
- Reload partially to obtain a partial mechanical closure of the cracks and then saturate the sample with fluid.

A change in wave velocities during compression will give not only information about the evolution of cracks within the sample (i.e. crack healing), but also about further damages that might occur during compression at higher pressure. In a previous study on seismic velocities and anisotropy (Yang et al. 2016), anisotropy in salt rock is not observed and other studies confirm that the influence of structural anisotropy decreases with increment in stress levels (Dubey et al., 2008); but we can not exclude its importance in microcracks evolution. Furthermore, The relationship between the dilatancy boundary and the permeability may play an important role in terms of time needed for salt rock to heal itself.

Prior to the rock salt experiment, triaxial experiments on of 5x5x5 cm cubes of sandstone were performed at the Christian-Albrechts University of Kiel (collaboration with Dr. H. Bahadur Motra) to assess if the method can be used to quantify crack density and fracture networks in rock salt. Beberthal sandstone was chosen as the material to perform proof of concept tests due to its low porosity (around 5-6%) and homogeneity (no presence of foliation). Measurements of P and S-wave velocities were made using the pulse transmission technique and done simultaneously in three orthogonal directions (X, Y, Z).

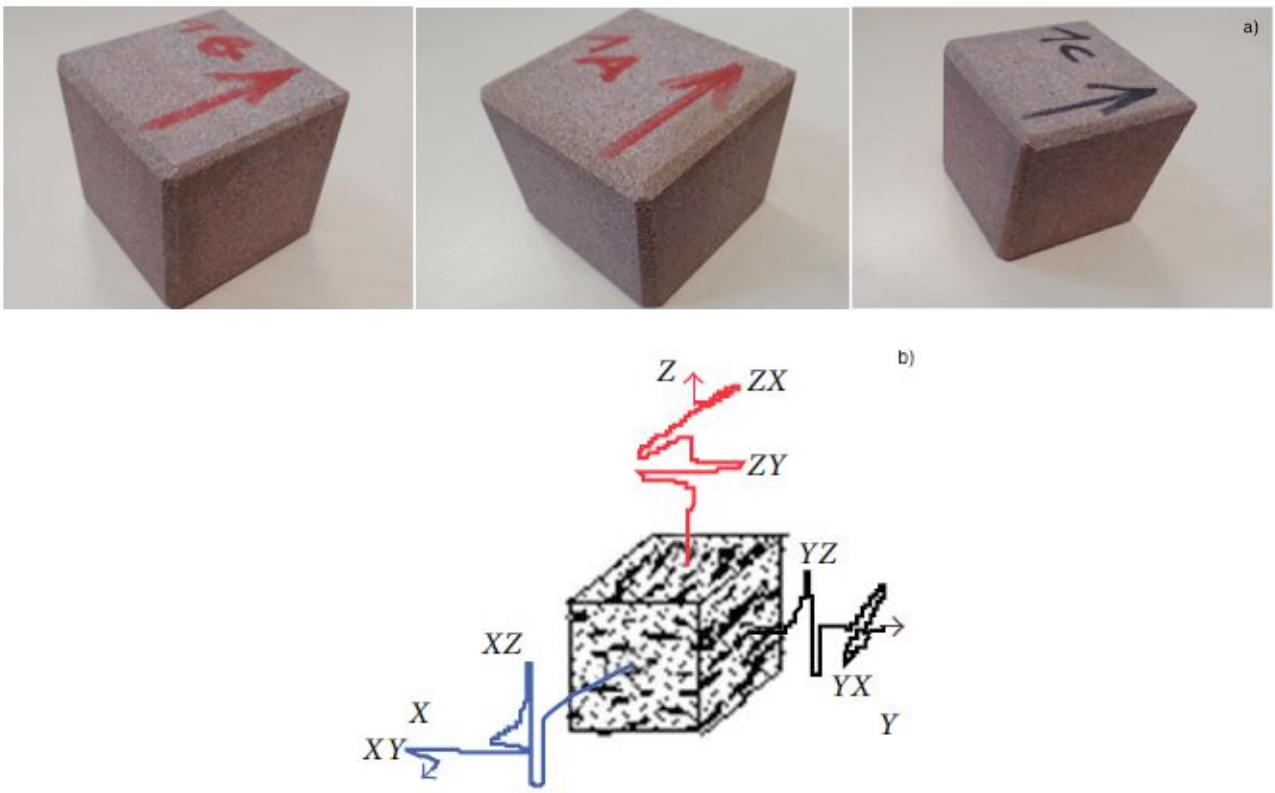

Figure 18: a) Samples used in the experiments, the arrow indicates the foliation normal; b) Direction of measurements, according to the structural frame X, Y, Z (XY is foliation, X is lineation and Z is foliation normal). (Kern, 2001).

3.1. Machine and preparation

P- S- wave velocities measurements were made on cubic samples in a multianvil apparatus (Figure 19) using the pulse transmission technique with transducers operating at 2 MHz for P-wave and 1 MHz for S-wave (Kern et al, 1997; Kern, 2011; Kern et al., 2015). Six pistons in the three orthogonal directions are pressed onto the samples to obtain a near-hydrostatic stress and the heat is transmitted from the pistons to the sample through a furnace to achieve a homogeneous temperature distribution (Figure 19d) (Kern et al., 1997). The machine allows simultaneous measurement of seismic velocity and their directional dependence and shear wave splitting is measured by two sets of oriented transducers with perpendicular planes (Kern et al., 1997; Kern, 2011). So that, the complete dataset comprises nine velocities: three P-wave velocities and six S-wave velocities along with volume change that is obtained from the piston displacement.

The first step is crucial to the success of the experiments. In fact, the six pistons need to be in contact with the sample, aligned and perfectly perpendicular to each other to be able to measure wave velocities (Figure 4c). Furthermore, the samples were covered in graphite to avoid friction and to

ensure a better conduction between the pistons and the sample to accurately measure P- and S-wave velocities. The sensor are situated at the end of the machine; for this reason, to have information about the pistons, a sample with well known V_p-V_s characteristics has been used to obtain the characteristics of the pistons that need to be subtracted from the results. Once the pistons are in contact with the sample and the signal of V_p and V_s is clear the experiment can start. For each wave measurements, we obtained three measurements for P-wave and six for S-wave.

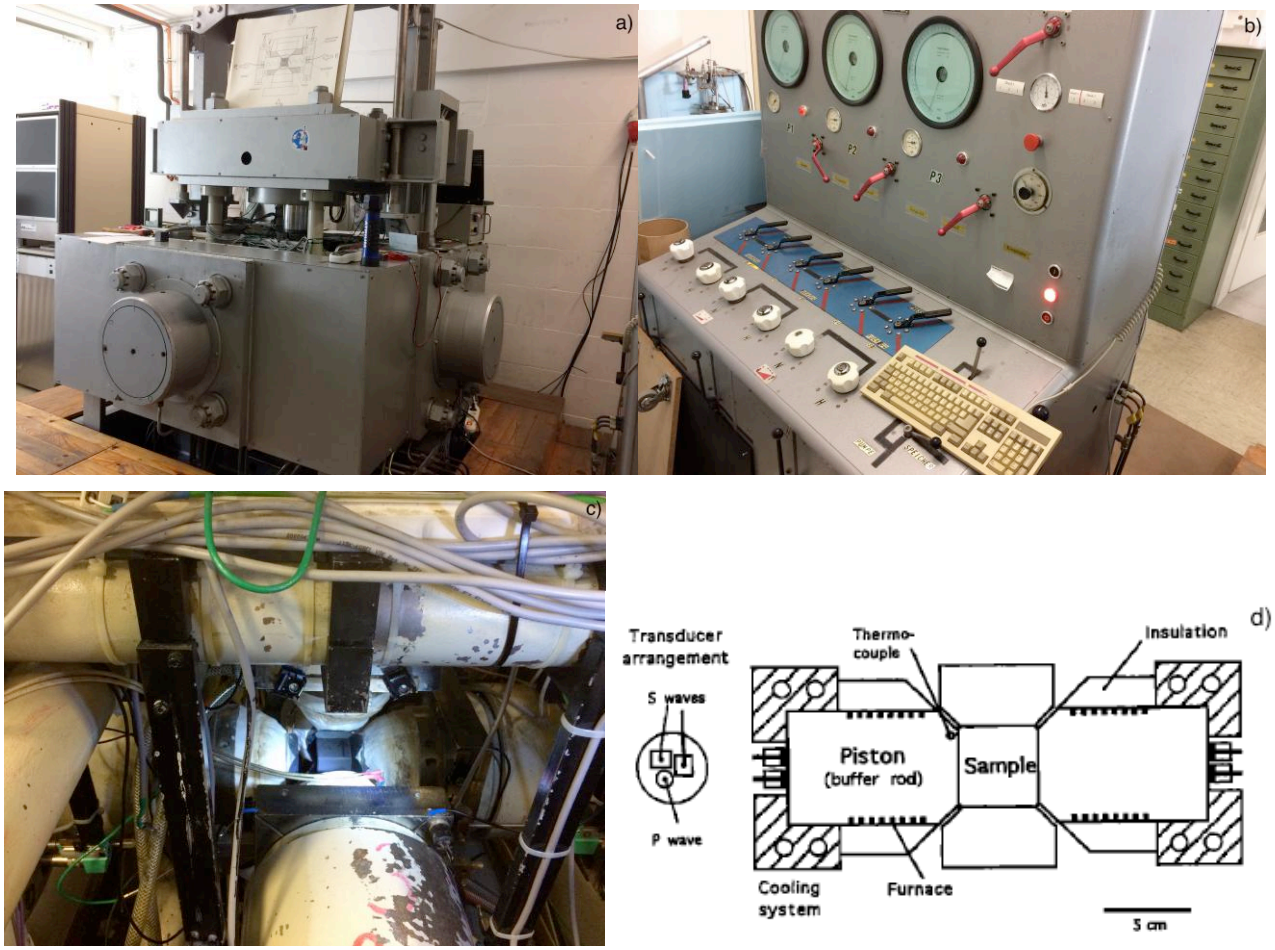

Figure 19: Equipment at the Christian-Albrechts University of Kiel a) Triaxial press; b) Pressure pump; c) Pistons; d) Schematic of the pistons.

3.2. Method

Experiments were made on three specimens applying the following differential stress: 80 120 and 140 for sample 1B, 1A and 1C respectively. Each experiment comprises four steps: deviatoric loading and unloading, hydrostatic loading and unloading.

During deviatoric loading, σ_1, σ_2, σ_3 were increased to 15 MPa in three steps (5, 10, 15 MPa), then σ_2, σ_3 were held at 15 MPa while increasing σ_1 from 15 Mpa to 95 MPa for sample 1B, to 135 MPa for sample

1A and to 155 MPa for sample 1C. During deviatoric unloading σ_1 is reduced to 15 MPa in steps of around 20 MPa and then σ_1, σ_2, σ_3 are reduced to zero.
The hydrostatic loading consists in increase σ_1, σ_2, σ_3 to 15 MPa in three steps of 5 MPa and then increase them in steps of 10 MPa until 105 MPa for sample 1B, 185 MPa for sample 1A and 205 MPa for sample 1C. During the hydrostatic unloading σ_1, σ_2, σ_3 reduced reversing the loading in steps of 20 MPa. V_p-V_s measurements are made at each step.

3.3. Results

The results from the three experiments were compared according to stress vs strain relationship, P-wave velocity, P- and S-wave anisotropy for both deviatoric and hydrostatic stress.

3.3.1. Deviatoric stress stage

3.3.1.1. Stress vs strain

The diagrams in Figure 20-21-22 show that the samples had permanent deformation in all the three experiments. In general, deformation results bigger in X (σ_3-e_3) and Y (σ_2- e_2) direction and smaller in Z direction (σ_1-e_1), as expected.

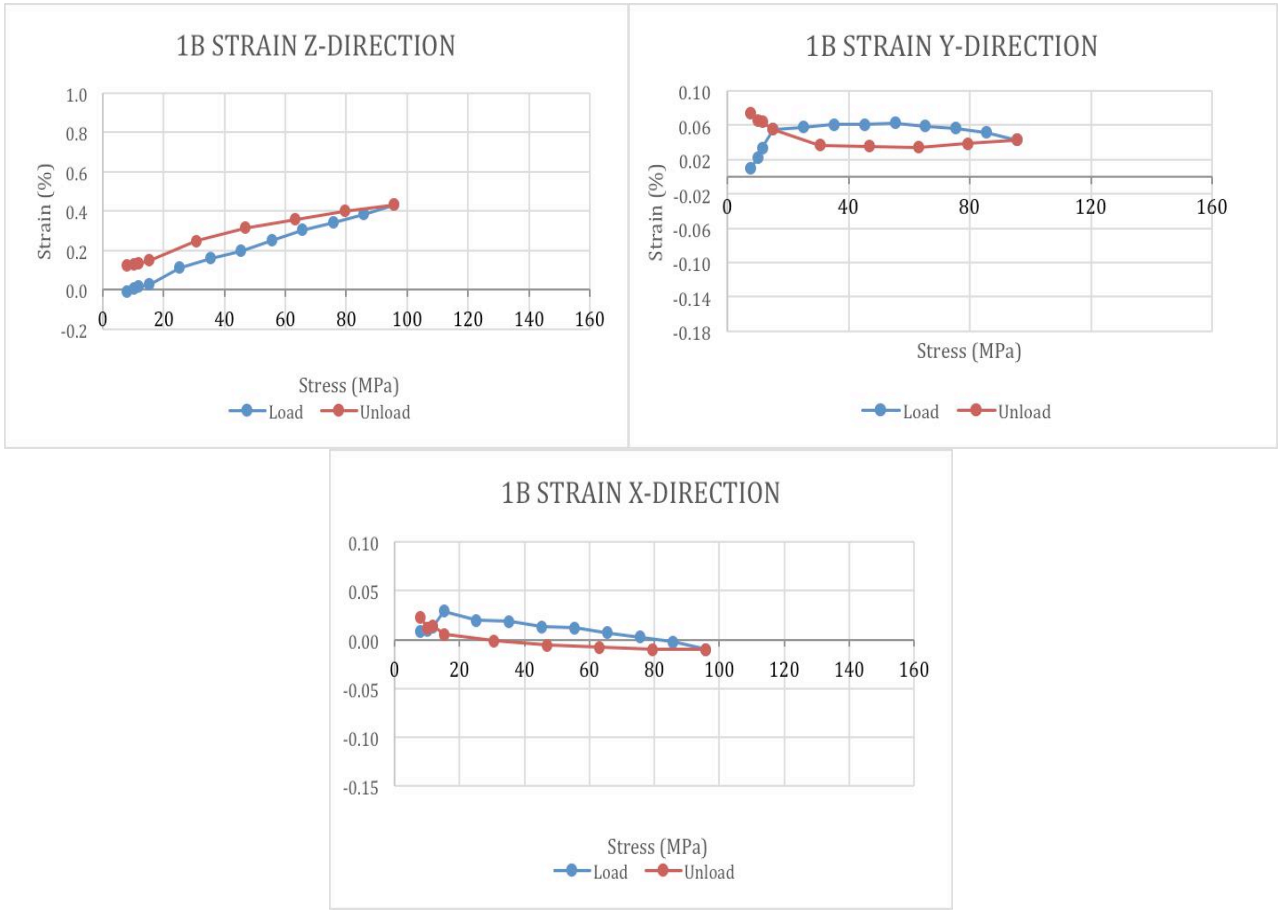

Figure 20: Strain-stress relationship in the three different directions (Z: σ_1-e_1, Y: σ_2- e_2, X: σ_3-e_3) for samples 1B, deviatoric stress.

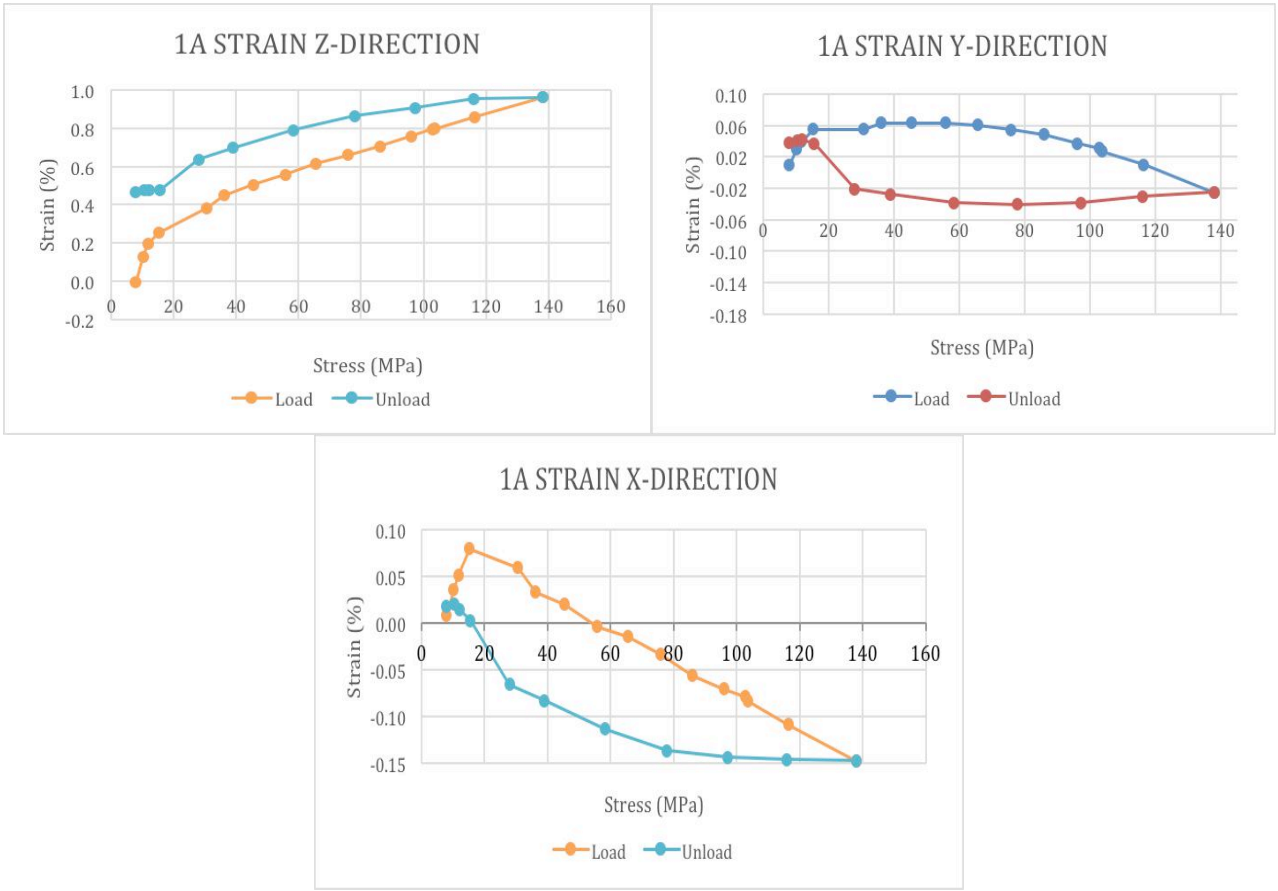

Figure 21: Strain-stress relationship in the three different directions (Z: σ_1-e_1, Y: σ_2- e_2, X: σ_3-e_3) for samples 1A, deviatoric stress.

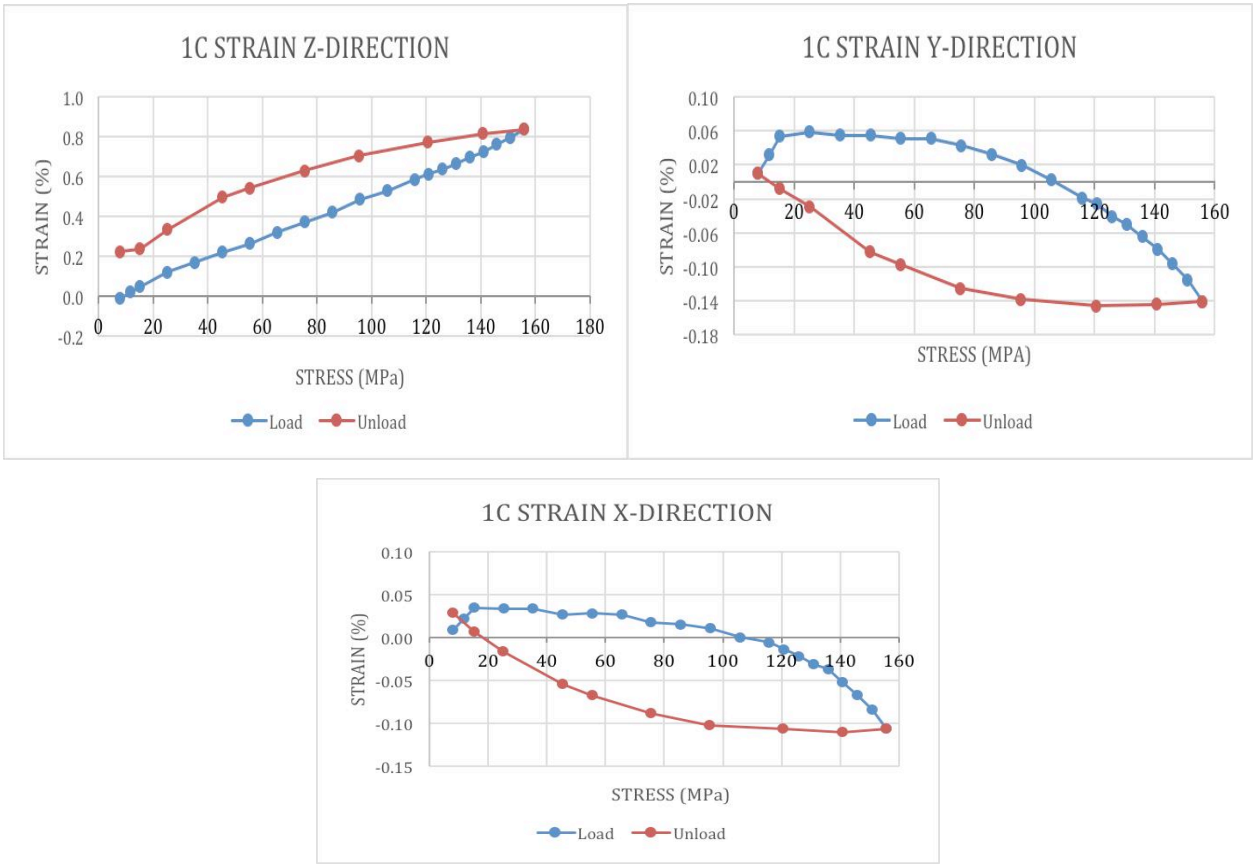

Figure 22: Strain-stress relationship in the three different directions (Z: σ_1-e_1, Y: σ_2- e_2, X: σ_3-e_3) for samples 1C, deviatoric stress.

3.3.1.2. P-wave velocity

P-waves show a non linear increase in velocity with the increasing of σ_1 until around 15 MPa, due to the progressive closure of existing cracks; after that, crack reopening is highlighted by a linear increase in V_p. Samples 1A and 1C show a decrease in V_p, around 98 and 115 MPa respectively, in X (σ_3) and Y (σ_2) directions and the unloading shows a different behaviour; while in Z (σ_1) direction loading and unloading result quite consistent. This behaviour in X and Y directions might be due to the opening of new cracks (around 98 MPa for 1A and 115 MPa for 1C) that seems to remain open during the unloading.

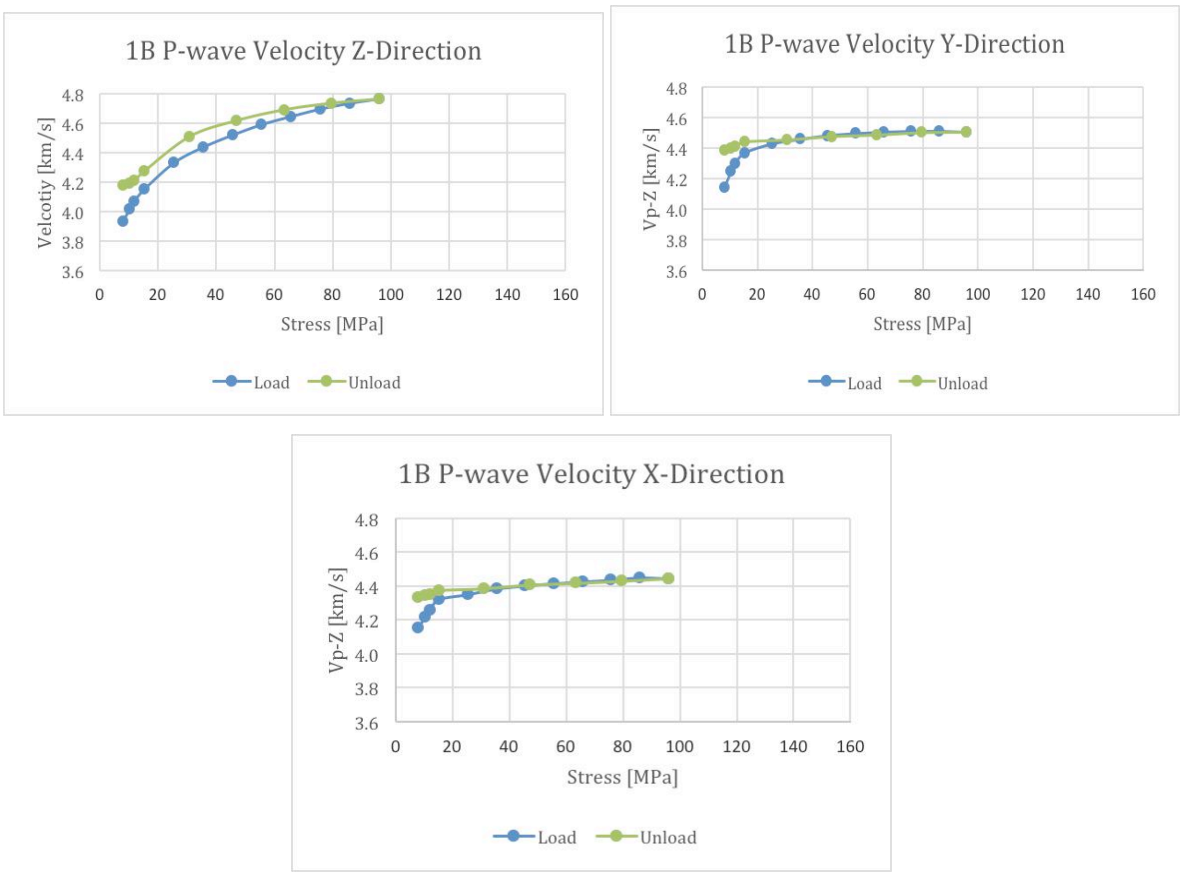

Figure 23: P-wave velocity in the three different directions (Z: σ_1, Y: σ_2, X: σ_3) for samples 1B, under deviatoric stress.

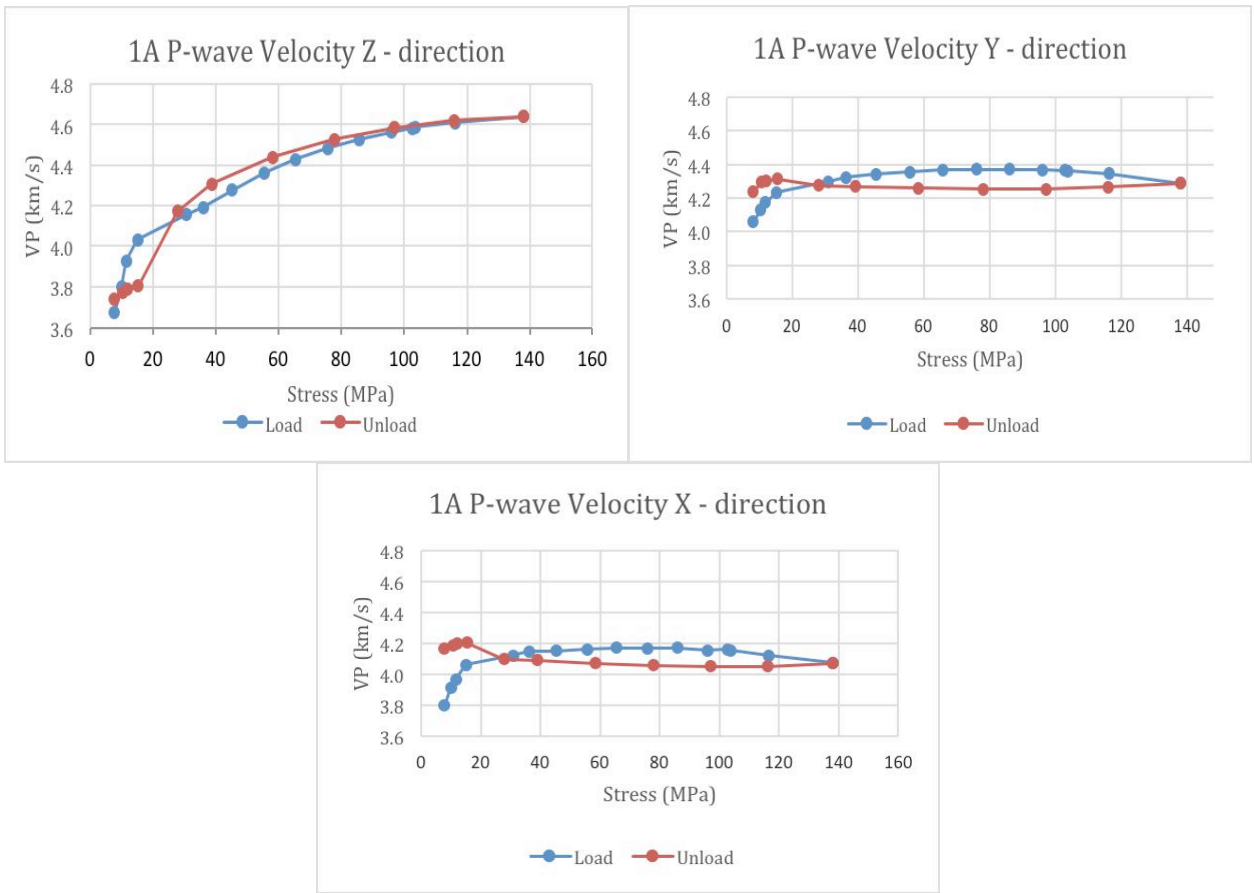

Figure 24: P-wave velocity in the three different directions (Z: σ_1, Y: σ_2, X: σ_3) for samples 1A, under deviatoric stress.

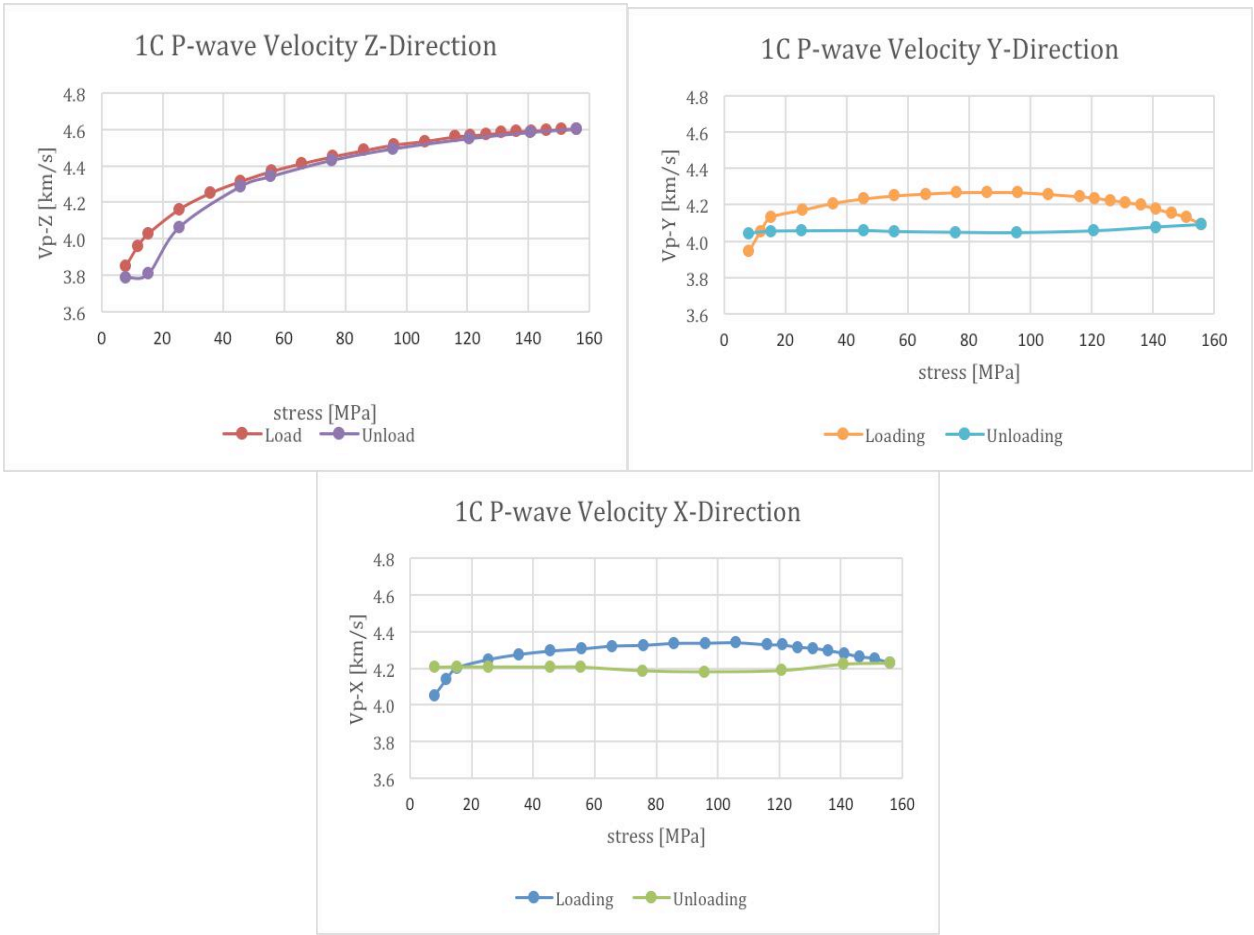

Figure 25: P-wave velocity in the three different directions (Z: σ_1, Y: σ_2, X: σ_3) for samples 1C, under deviatoric stress.

3.3.1.3. Anisotropy

Anysotropy of P-wave velocity results higher at low pressure due to the effect of the crystallographic preferred orientation that appear readuced with the increasing stress until its lowest value (around 35 MPa), when all the cracks are closed. The new increase in anisotropy, after the lowest value, might be due to crack reopening. Anisotropy of S-wave velocity increase with the increasing pressure until 15 MPa for sample 1B and 1A and until around 25 MPa for sample 1C, then the trend remains linear.

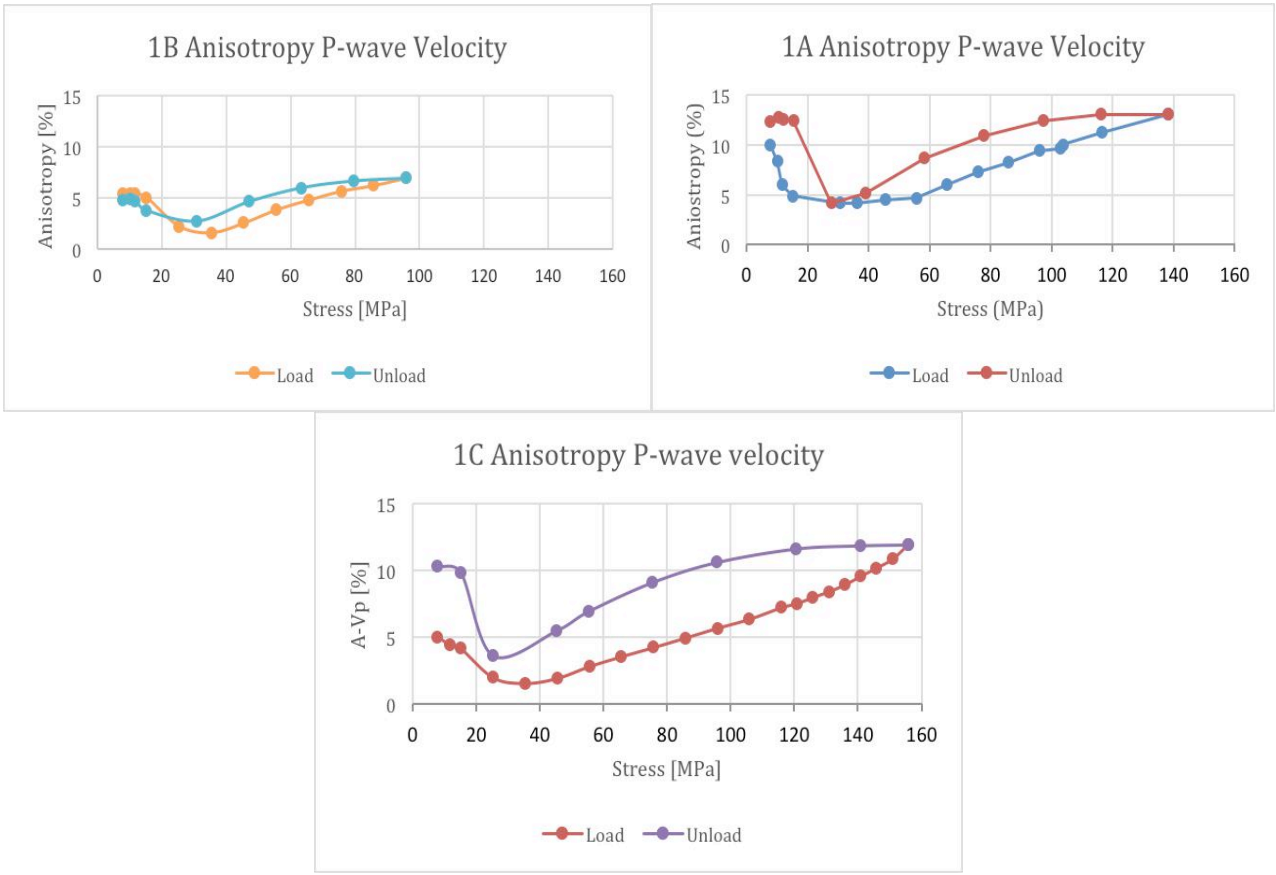

Figure 26: Anisotropy of P-waves for samples 1B-1A-1C under deviatoric stress.

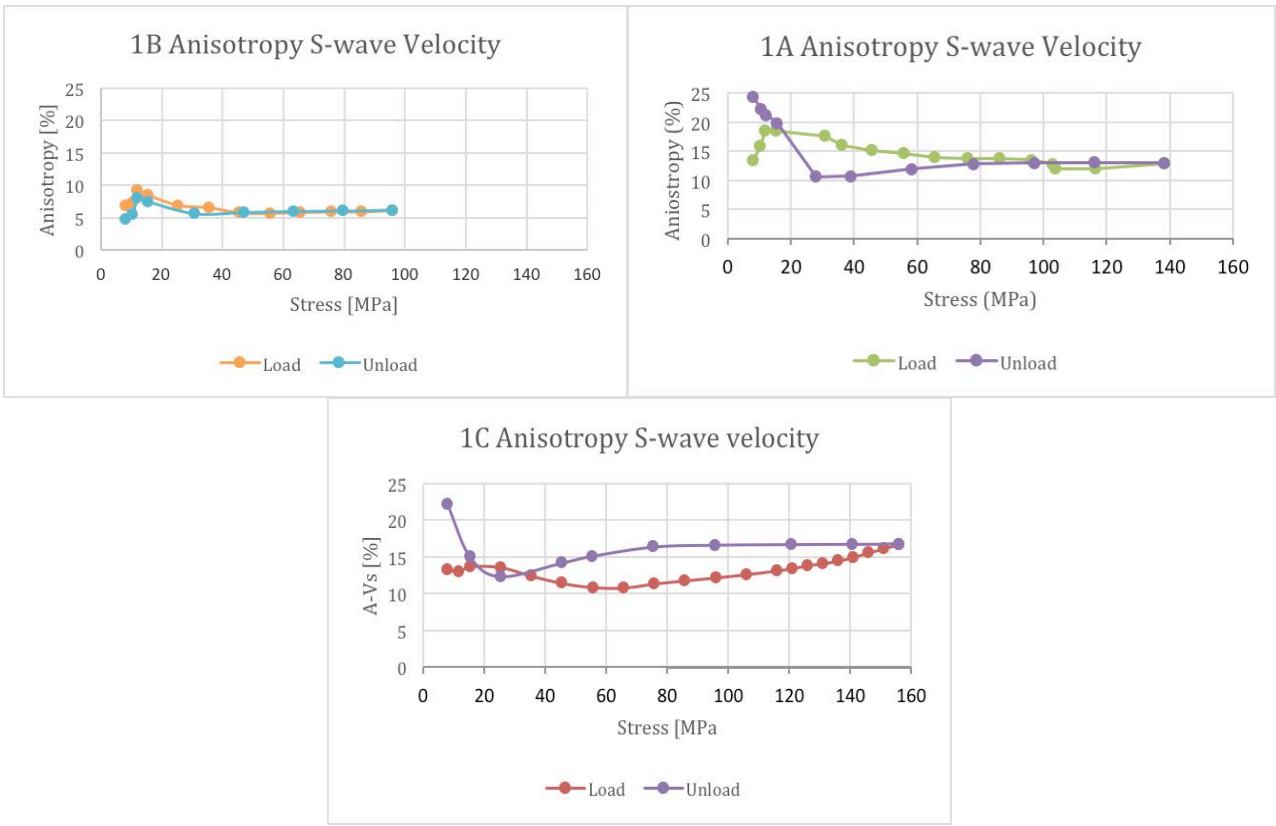

Figure 27: Anisotropy of S-waves for samples 1B-1A-1C under deviatoric stress.

3.3.2. Hydrostatic stress stage

3.3.2.1. Stress vs strain

In this case the loading-unloading in relation to stress vs strain result quite consistent in respect to the case of deviatoric stress applied to the samples; however, it is possible to notice deformation within the samples. In fact, permanent deformation is clearly visible in sample 1C and 1A in X direction (σ_3-e_3) more than in the other two; while in sample 1B Y direction (σ_2- e_2) seems to be the one subjected to deformation.

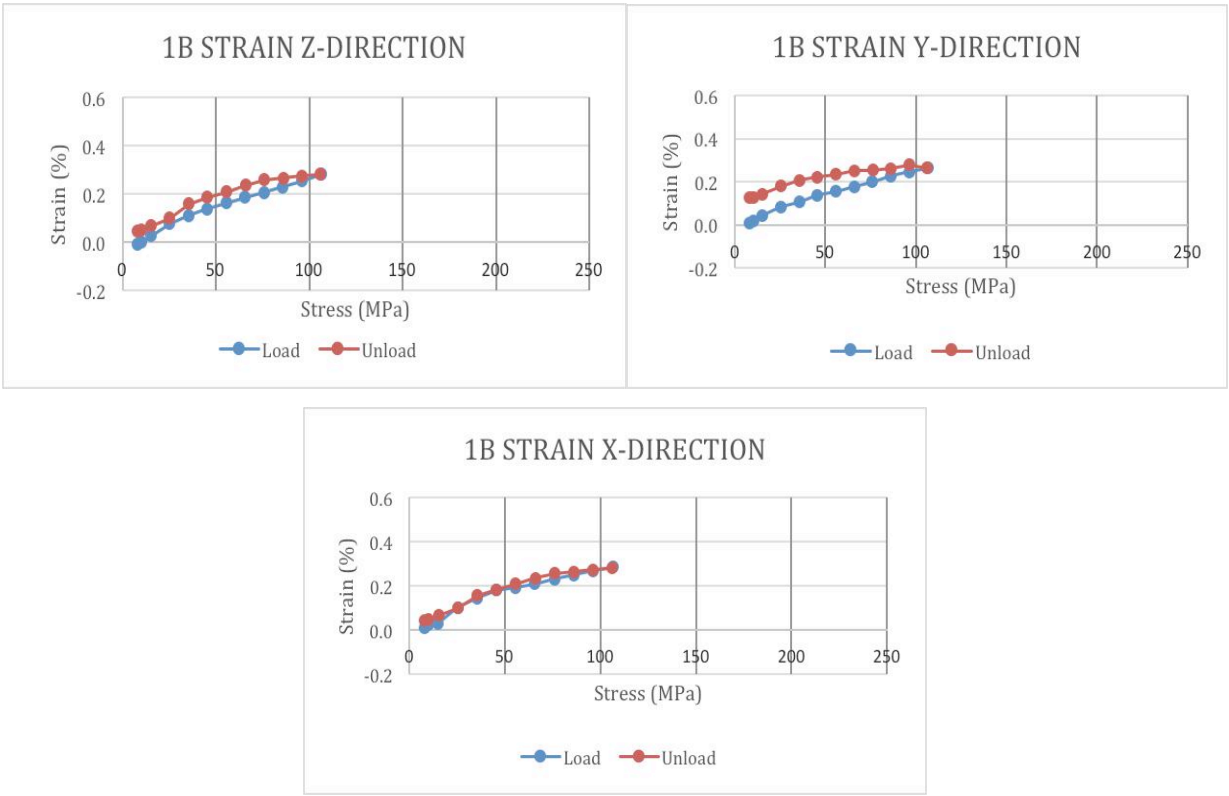

Figure 28: Strain-stress relationship in the three different directions (Z: σ_1-e_1, Y: σ_2- e_2, X: σ_3-e_3) for samples 1B, under hydrostatic stress.

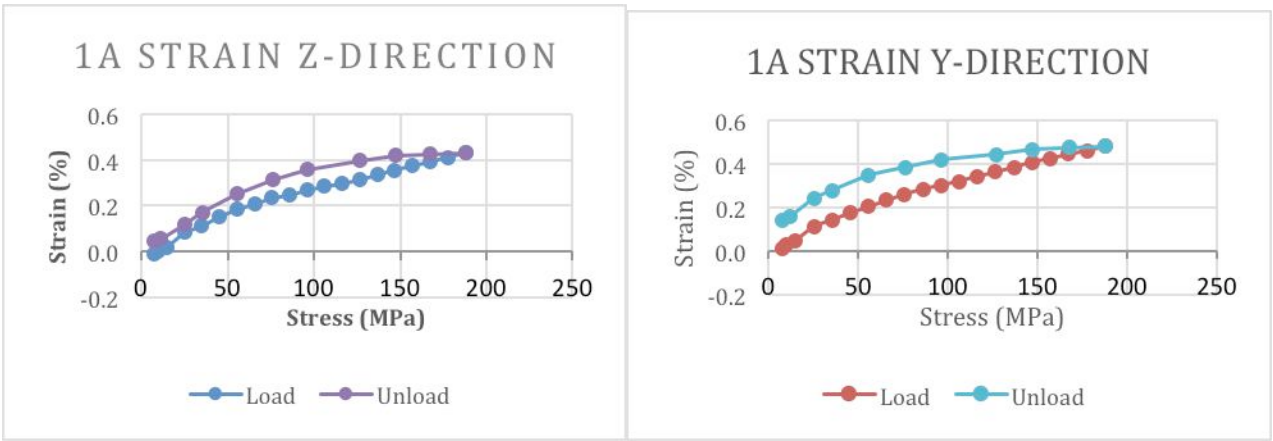

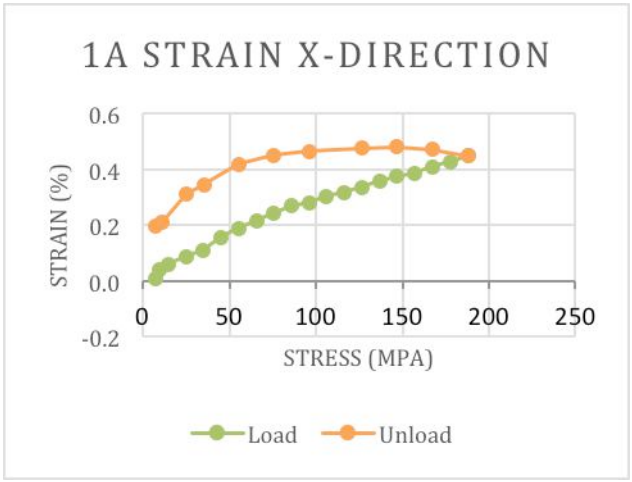

Figure 29: Strain-stress relationship in the three different directions (Z: σ_1-e_1, Y: σ_2- e_2, X: σ_3-e_3) for samples 1A, under hydrostatic stress.

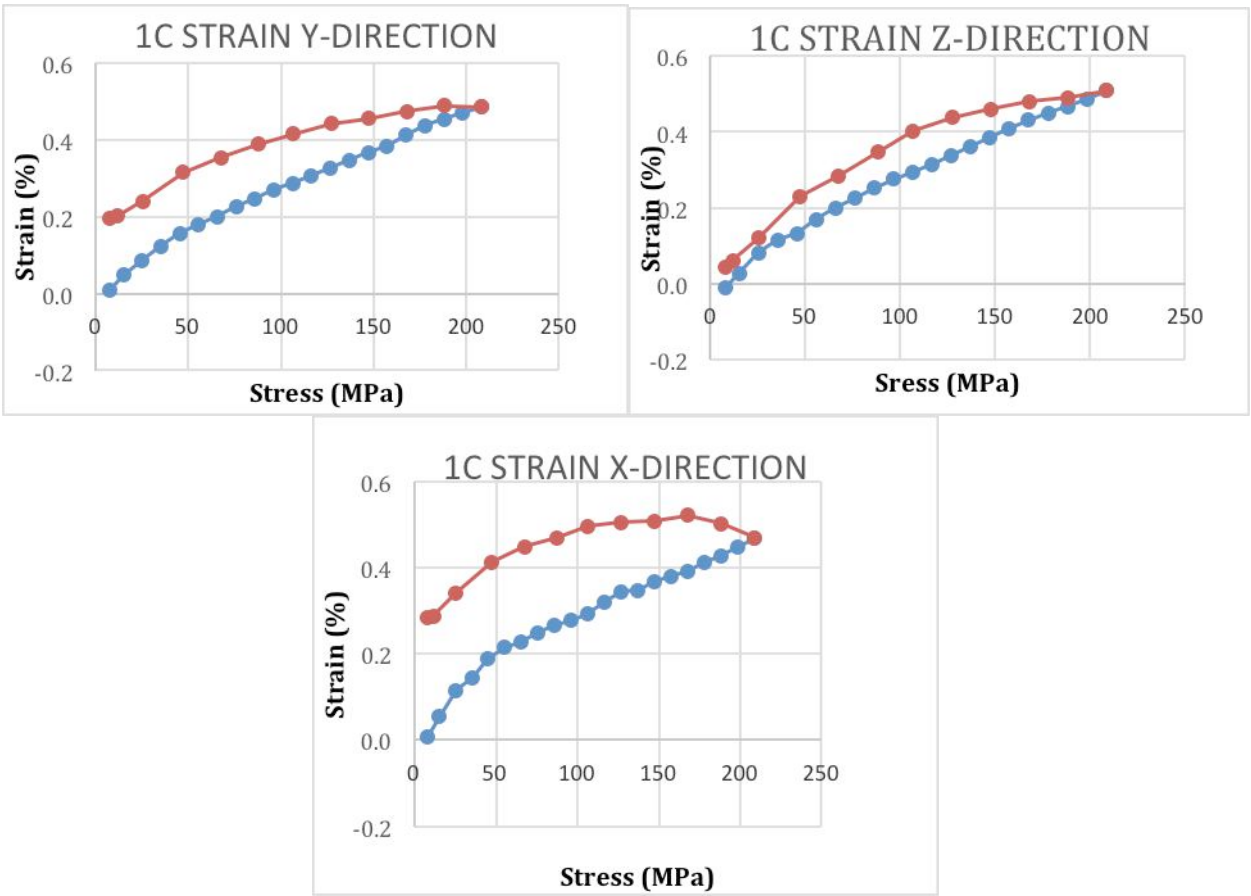

Figure 30: Strain-stress relationship in the three different directions (Z: σ_1-e_1, Y: σ_2- e_2, X: σ_3-e_3) for samples 1C, under hydrostatic stress.

3.3.2.2. P-wave velocity

Velocity of P-waves show a non linear behaviour at low pressure within 40 MPa for sample 1B and around 50 MPa for samples 1A and 1C. As discussed before, this behaviour is due to the closure of exsisting cracks and it is followed by a linear increase in velocity due to their reopening. In this case,

decreasing of wave velocity at higher stresses is not present and development of new cracks might be excluded.

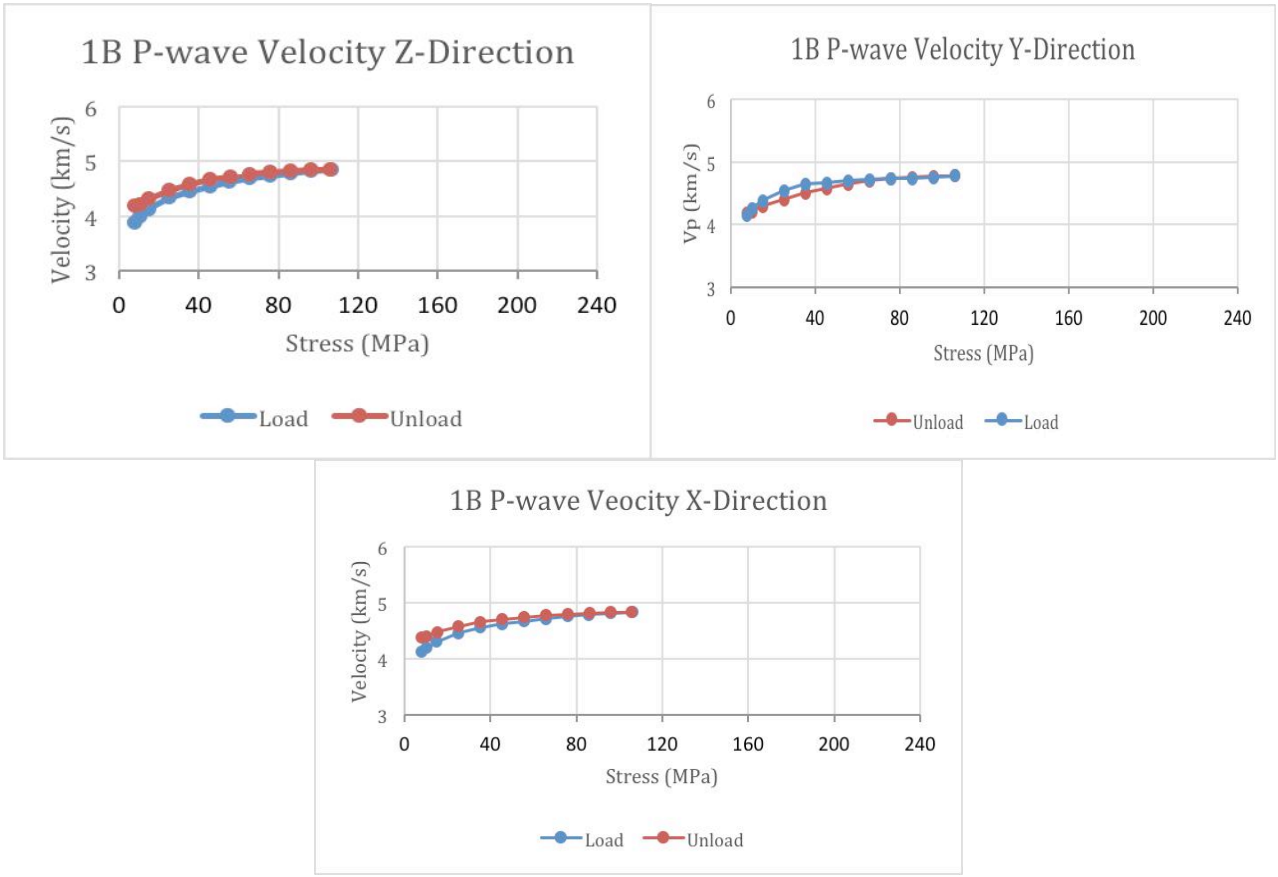

Figure 31: P-wave velocity in the three different directions (Z: σ_1, Y: σ_2, X: σ_3) for samples 1B, under hydrostatic stress.

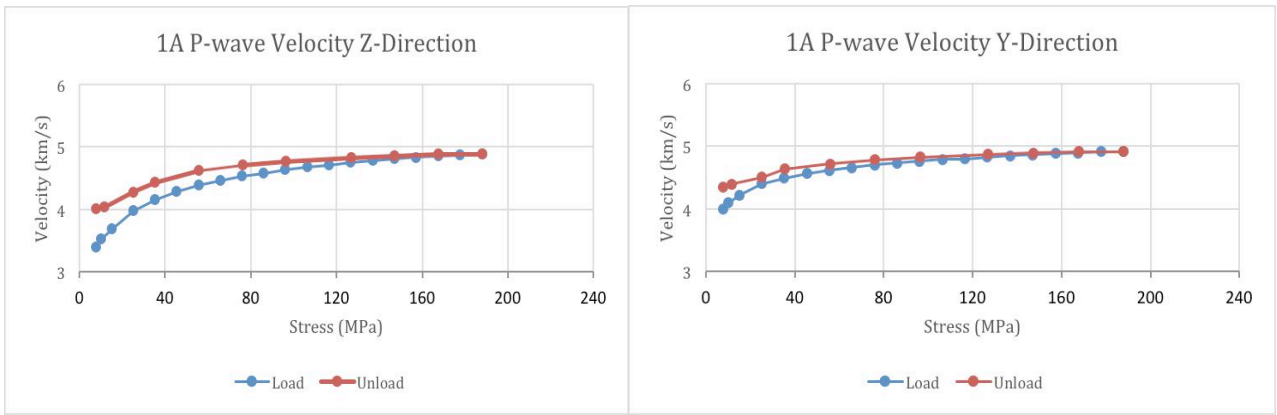

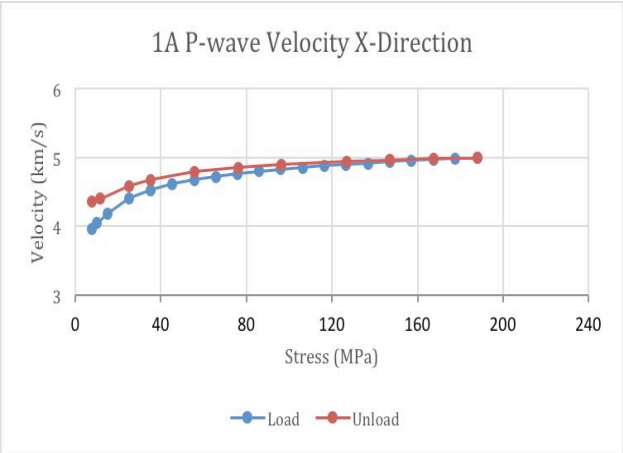

Figure 32: P-wave velocity in the three different directions (Z: σ_1, Y: σ_2, X: σ_3) for samples 1A, under hydrostatic stress.

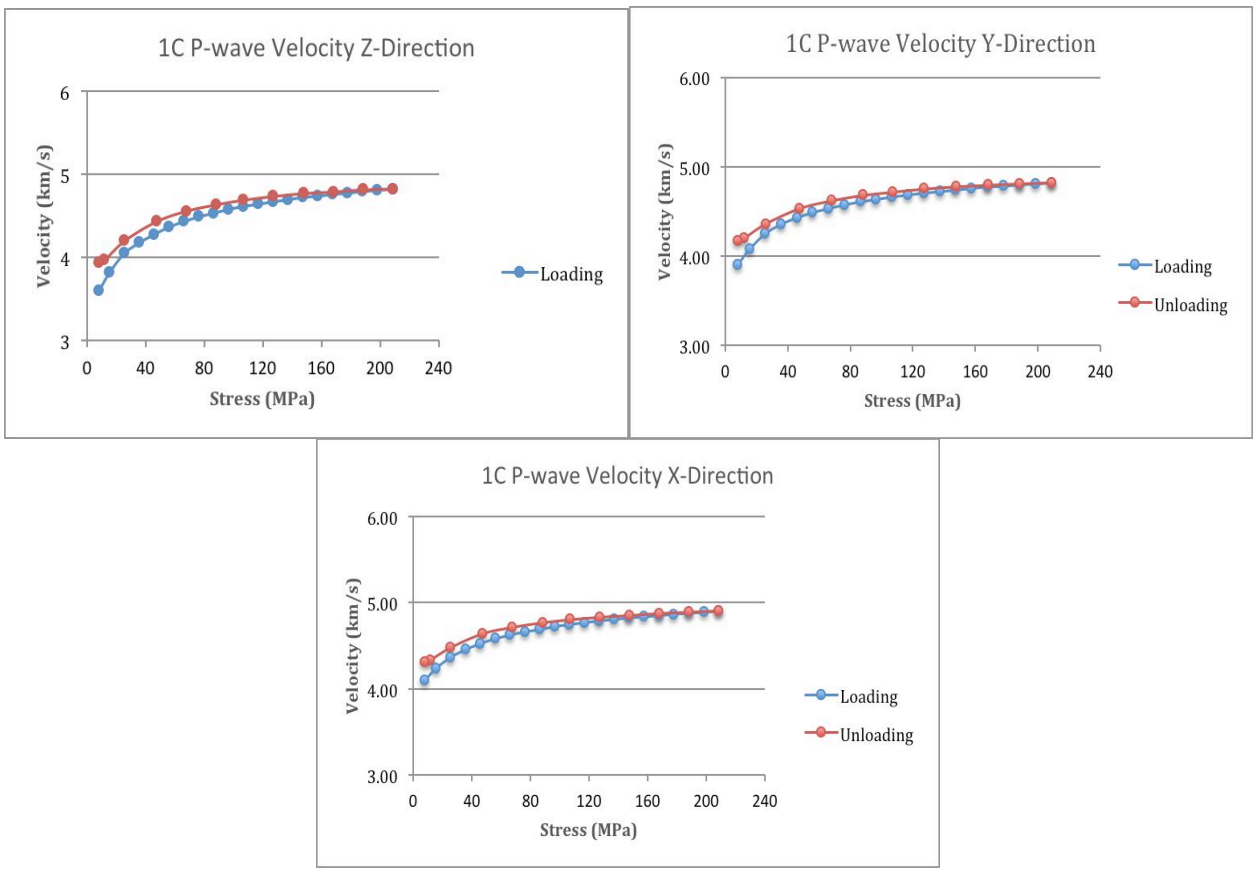

Figure 33: P-wave velocity in the three different directions (Z: σ_1, Y: σ_2, X: σ_3) for samples 1C, under hydrostatic stress.

3.3.2.3. Anisotropy

The behaviour of anisotropy results quite consistent with the one obtained during the first step of the experiments (under deviatoric stress). High anisotropy of P-wave velocity at the beginning of the experiment decreasing with the increasing pressure, that in this case results linear and with no further increase. The trend of anisotropy confirms the results obtained for P-wave velocity excluding the

development of new cracks. Anisotropy of S-wave velocity increases until around 10 MPa in sample 1B, while for sample 1A and 1C deacrease non-linearly until 40 MPa followed by a linear decrease with the increasing pressure in all the three experiments.

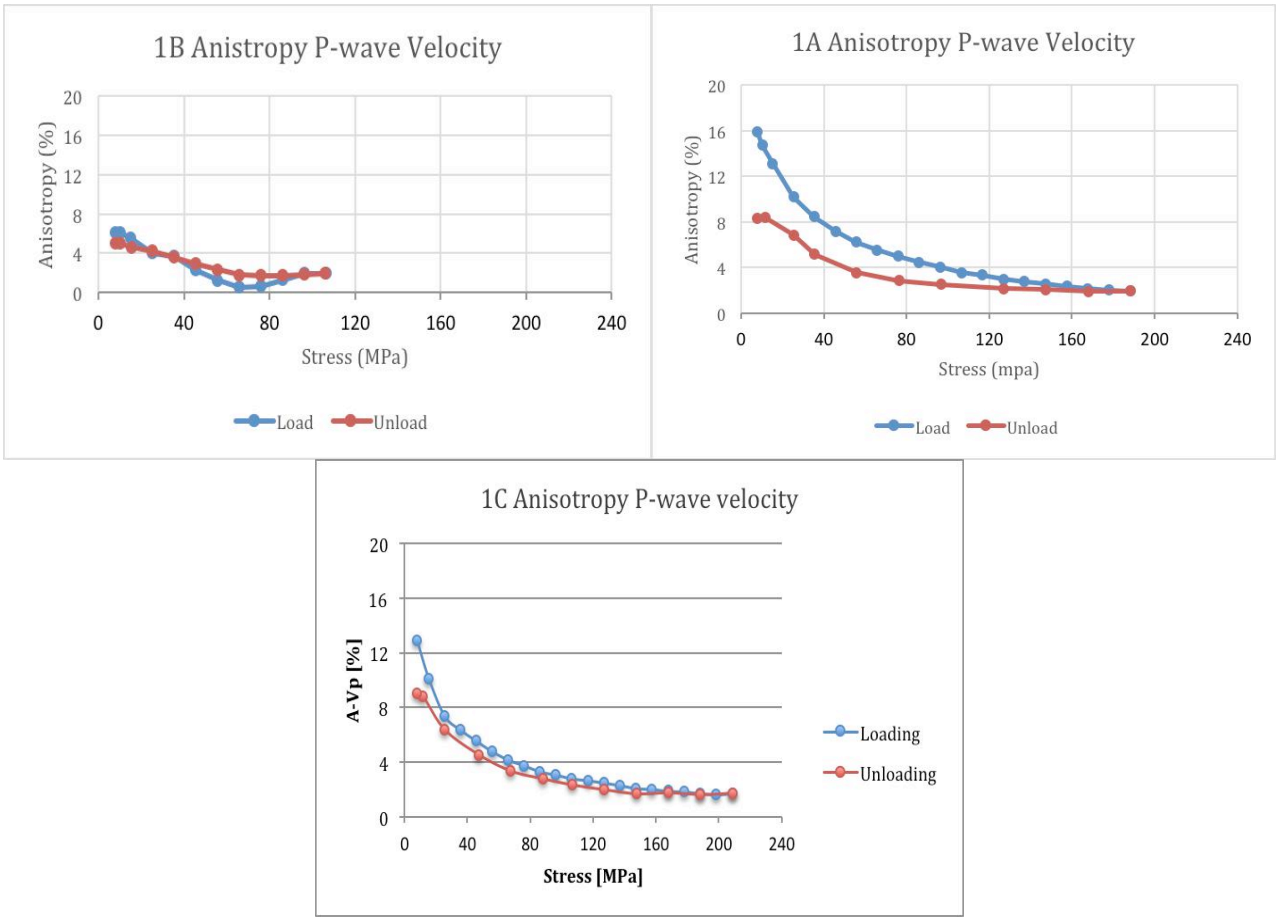

Figure 34: Anisotropy of P-waves for samples 1B-1A-1C under hydrostatic stress.

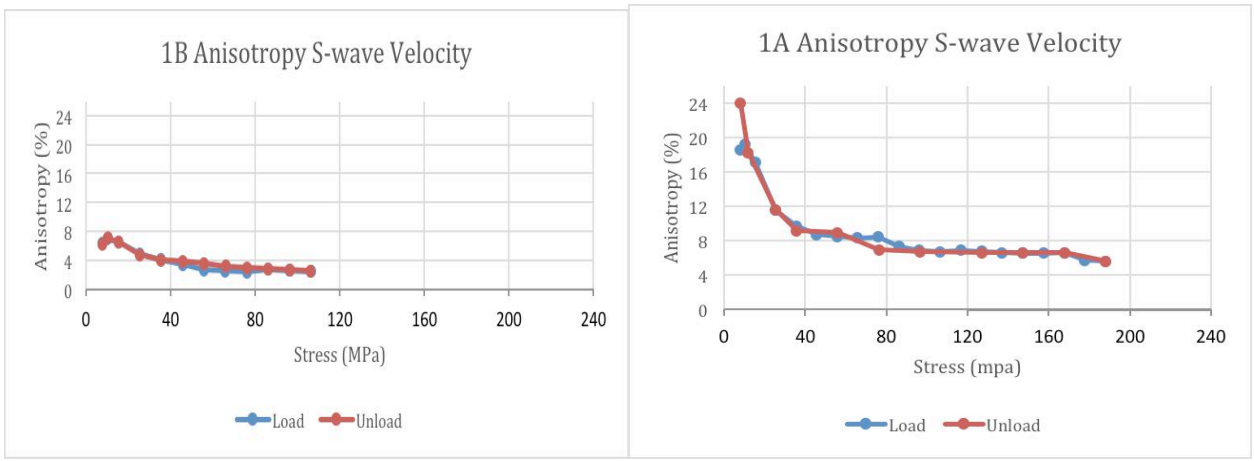

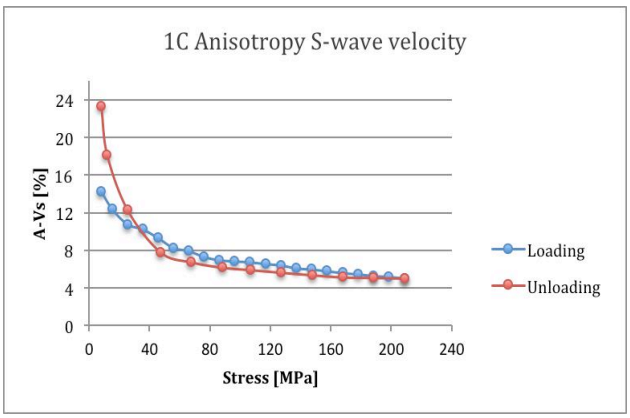

Figure 35: Anisotropy of S-waves for samples 1B-1A-1C under hydrostatic stress.

3.4. Discussion

The experiments provided interesting results in V_p-V_s measurements for sandstone under triaxial stress, in both the condition of deviatoric and hydrostatic stress. The trend of P- and S-wave velocities is consistent with the results obtained in the pre-esisting literature. In fact, previous studies hightlight the characteristic of wave velocities to be affected by two different processes: compaction/crack closure and grain crushing/opening of new cracks (Fortin et al., 2005; Fortin et al., 2006; Fortin et al., 2007). In particular, at low confining pressure (until around 50 MPa) seismic wave velocities increase with pressure due to the closure of pre-existing cracks and pores, while at greater pressure the rate of increase is smaller (Fortin et al., 2006; Fortin et al., 2007; Browning et al., 2017). At greater pressure, wave velocities might slightly decrease (as in our case of deviatoric stress for sample 1A and 1C) due to the nucleation and propagation of new cracks that appear at high pressure (Fortin et al., 2007; Browning et al., 2017), until a point in witch wave velocities might increase again due to the closure of the new cracks (not visible in our case) (Fortin et al., 2007). The general behaviour of seismic velocities is consistent with the information obtained from acoustic emission measurements by Browning et al. (2017), showing a dilatant cracking from around 40 MPa.
Due to time issues, it was not possible to apply the method to salt rock samples and consequently to include new experiments in this work. Moreover, it is important to notice that this experiment on salt rock might include issues due to its properties; in fact, its sensitivity to moisture might effect the prepararation of the samples for the experiments that need to be prepared by hand.

However, the results obtained on sandstone reveal that the experiment could represent a great tool to investigate the behaviour of salt rock under 3D stress, providing important information on crack damage/evolution and consequently crack healing. For this reason, further experiments on rock salt under deviatoric stress, in addiction with acoustic measurements, are suggested for future researches.

4. Monitoring crack healing in wet rock salt: Time lapse CT-scanning

CT-scan experiments were done on compacted aggregates of granular rock salt to monitor cracks and investigate its healing. Prior to CT-scanning, we investigate diffusion controlled mass transport in salt rock, starting from the model by Houben et al. (2013) and simulate the progress of crack healing by using different values of diffusion coefficient in relationship with the thickness of the fluid film.

4.1. Diffusion controlled mass transport: the model

At high stresses, creep is controlled by dislocation mechanisms that act through the crystal lattice of the rock salt. However, at lower stresses, under conditions of long-term deformation, grain boundary dissolution-precipitation processes play a significant role (Urai and Spiers, 2007). In fact, processes as solution-precipitation creep, followed by mass transport, take place at the grain boundaries and result especially effective when a fluid phase is present.

To explain the diffusion controlled mass transport in rock salt and, consequently, the change in shape of its inclusions, we consider a fluid inclusion within a halite crystal. In particular, we consider half of a fluid inclusion assuming a V-shape opening with planar walls (Figure 36). Mass transport of material includes three main processes going from the point with the higher to the point with the lower chemical potential (Figure 37). Starting from the walls (point B), dissolution at the solid-fluid interface will occur, followed by diffusion through the fluid inclusion and precipitation of the material at the cusp (point A). Furthermore, the area of precipitation at the cusp is smaller than the area of dissolution at the walls, so that the precipitation velocity will be faster than the dissolution velocity (Houben et al., 2013) meaning that precipitation is the controlling mechanism.

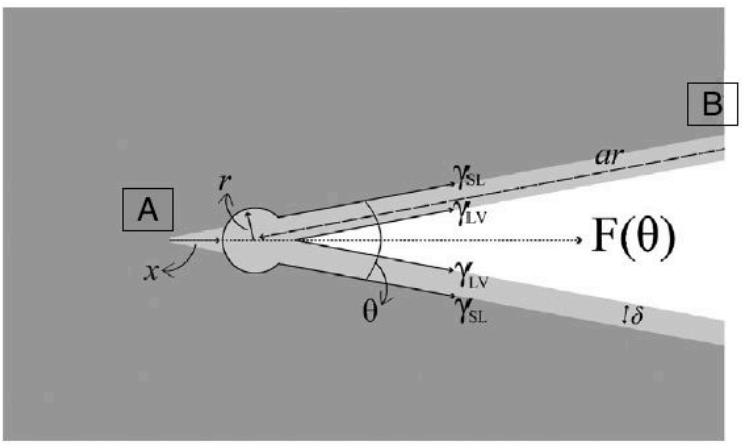

Figure 36: Half fluid inclusion. (modified from Houben et al., 2013).

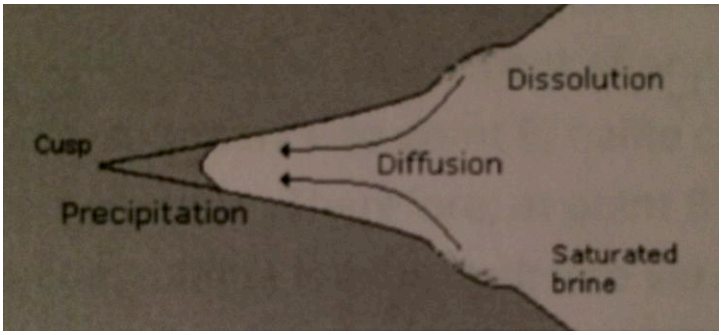

Figure 37: Processes of mass transport.

Gradient in surface curvature between crack walls and cusp lead to a gradient in chemical potential at the solid surface (Houben et al., 2012). The chemical potential of the solid at a free surface is given by

$$\mu = f + (p + \Delta p)\Omega \qquad \text{[J/mol]}$$

with $\Delta p = \gamma_{SL}(\frac{1}{r_1} + \frac{1}{r_2})$ results to be

$$\mu = f + p\Omega + \Omega\gamma_{SL}(\frac{1}{r_1} + \frac{1}{r_2}) \qquad \text{[J/mol]}$$

where ƒ is the free energy in the solid, p the pressure of the solution phase, Ω the molar volume of the solid and γ_{SL} the solid-liquid interfacial energy.

As we assumed that the inclusion is almost a sphere, $r_1 \approx r_2 = r$ and the chemical potential can be rewritten as

$$\mu = f + p\Omega + \frac{2\Omega\gamma_{SL}}{r}$$

Since the chemical potential at the crack walls is different from the one at the cusp, we need to know the driving force:

$$\Delta\mu = \mu_B - \mu_A$$

At the cusp, the chemical potential can be described in terms of the surface force F(θ) acting on the cusp due to the surface tension of the two converging crack surfaces (Houben et al., 2013):

$$\mu_A = f_A + p\Omega_A - F(\theta)\Omega(\frac{1}{r_1} + \frac{1}{r_2})$$

and since we consider $r_1 \approx r_2 = r$ and the chemical potential can be written as

$$\mu = f_A + p\Omega_A - \frac{F(\theta)\Omega}{2r}$$

For the case of an aqueous film adsorbed at the crack surfaces (Houben et al., 2013): $F(\theta)=2(\gamma_{SL}+\gamma_{LV})\cos\frac{\theta}{2}$, so that

$$\mu_A = f_A + p\Omega_A - \frac{\Omega(\gamma_{SL}+\gamma_{LV})\cos\theta/2}{r}$$

At the crack walls the potential results to be

$$\mu_B = f_B + p\Omega_B - \Omega\gamma_{SL}(\frac{1}{r_1}+\frac{1}{r_2})$$

in this case, the walls are almost flat, so that the radii of curvature tend to infinitive (i.e. $\Omega\gamma_{SL}(\frac{1}{r_1}+\frac{1}{r_2})=0$) and we obtain

$$\mu_B = f_B + p\Omega_B$$

So that the driving force result to be

$$\Delta\mu = \mu_B - \mu_A = (f_B + p\Omega_B) - (f_A + p\Omega_A - \frac{\gamma_{SL}\Omega_A}{r})$$

After few simplifications the differential potential can be rewritten as

$$\Delta\mu = \frac{\Omega(\gamma_{SL}+\gamma_{LV})\cos\theta/2}{r} \qquad [\text{J/mol}]$$

According to Houben et al. (2012), the diffusion of the solid is a slow process, while precipitation and dissolution appear to be considerably rapid (i.e. diffusive transport is not controlled by precipitation and dissolution). For this reason, to describe the diffusive flux of the dissolved material arriving at the point A, we can apply the Fick's first law:

$$J = -D\frac{\Delta C}{\Delta x} \qquad [\text{mol}/(\text{m}^2\text{s})]$$

where D is the diffusion coefficient of the solute in the solution [m^2/s], C the average concentration of the solid dissolved in the fluid phase [mol/m^3] and Δx the transport distance [m].

Making use of the definition for an ideal solution (Giacomel et al., 2015/16): $\Delta\mu = \mu_0 + 2RT\ln(\frac{\gamma C}{\gamma_0 C_0})$, we obtain

$$\frac{d\mu}{dC} = \frac{2RT}{C}$$

$$\frac{d\mu}{dx} = \frac{2RT}{C}\frac{dC}{dx}$$

$$\frac{dC}{dx} = \frac{C}{2RT}\frac{d\mu}{dx}$$

So that the Fick's law become

$$J = -\frac{dC}{RT}\frac{\Delta\mu}{\Delta x} \qquad [\text{mol}/(\text{m}^2\text{s})]$$

where R is the gas constant [J/(molK)] and T the temperature [K].

We can consider the transport distance from the crack to the cusp $\Delta x = ar$ and knowing that $\Delta\mu = \frac{\Omega(\gamma_{SL} + \gamma_{LV})\cos\theta/2}{r}$ we obtain:

$$J = -\frac{DC}{2RT}\frac{\Omega(\gamma_{SL} + \gamma_{LV})\cos\theta/2}{ar^2} \qquad [\text{mol}/(\text{m}^2\text{s})]$$

The total flux of the material is obtained multiplying the flux J by the area of transport, that represents the area in which diffusion occur: $A_t = 2\delta l$, where δ represent the thickness of the fluid film and l the extent of the cusp normal to the plane (Figure 26).

Hence:

$$J = -\frac{DC}{RT}\frac{\delta l\Omega(\gamma_{SL} + \gamma_{LV})\cos\theta/2}{ar^2} \qquad [\text{mol/s}]$$

In this process, we are interested in a better understanding of the velocity of the shrinking of the inclusions in rock salt. To that end, we compute the total volume arriving at the cusp (point A) per second:

$$V_t = J_{tot}\Omega \qquad [\text{m}^3/\text{s}]$$

$$V_t = \frac{DC}{RT}\frac{\delta\Omega^2(\gamma_{SL} + \gamma_{LV})\cos\theta/2}{\pi ar^2}$$

hence, the velocity of the migration at the cusp will be

$$v = \frac{J_{tot}\Omega}{A_{prec}} \qquad [\text{m/s}]$$

Knowing that $A_{prep} = \pi rl$ is the area in which precipitation of dissolved material occur, we obtain

$$v = \frac{DC}{RT}\frac{\delta\Omega^2(\gamma_{SL} + \gamma_{LV})\cos\theta/2}{\pi ar^3} \qquad [\text{m/s}]$$

So far we considered the average concentration of the solid dissolved in the fluid phase (C) in the unit of [mol/m³], to obtain an non-dimensional value we need to divide C by the molar volume Ω; so that

$$v = \frac{DC}{RT}\frac{\delta\Omega(\gamma_{SL}+\gamma_{LV})\cos\theta/2}{\pi a r^3} \qquad [m/s]$$

At this point, we can compute the time in which the cusp will migrate from the original point A toward the walls by a migration distance x:

$$t = \frac{\pi RT}{DC\Omega(\gamma_{SL}+\gamma_{LV})}\frac{a}{\delta}\int_0^x \frac{r(x)^3}{\cos\theta/2}dx \qquad [s]$$

Taking $r(x)=\alpha x$ (where α is the crack opening parameter) and cosθ/2=constant and solving the integral:

$$t = \frac{\pi RT}{DC\Omega(\gamma_{SL}+\gamma_{LV})}\frac{a}{\delta}\frac{\alpha^3 x^4}{4\cos\theta/2} \qquad [s]$$

$$t = \frac{\pi RT\alpha^3}{4DC\Omega(\gamma_{SL}+\gamma_{LV})}\frac{a}{\delta}\frac{x^4}{\cos\theta/2}$$

This can be rewritten using logarithms and using the properties of logs:

$$\log t = \log AB$$

$$\log t = \log A + \log B$$

$$\log t - \log A = \log B$$

$$\log\frac{t}{A} = B$$

where $A = \frac{\pi RT\alpha^3}{4DC\Omega(\gamma_{SL}+\gamma_{LV})}$ and $B = \frac{a}{\delta}\frac{x^4}{\cos\theta/2}$

So that become

$$\log t\frac{4DC\Omega(\gamma_{SL}+\gamma_{LV})}{\pi RT\alpha^3} = \log\frac{a}{\delta}\frac{x^4}{\cos\theta/2}$$ or better

$$\log x = \frac{1}{4}\log t + \frac{1}{4}\log\frac{4DC\Omega(\gamma_{SL}+\gamma_{LV})}{\pi RT\alpha^3} - \frac{1}{4}\log\frac{a}{\delta\cos\theta/2}$$

and again, using the properties of logs we reduce the last as

$$x = \frac{4t\delta DC\Omega(\gamma_{SL}+\gamma_{LV})\cos\theta/2}{a\pi RT\alpha^3} \qquad [m]$$ where x represent the migration distance of the cusp.

4.2. Simulating the progress of crack healing in wet rock salt

To be able to predict the expected changes during the time lapse CT scanning and to validate whether or not healing can be measured (i.e. to recognise the healing process) values of the crack opening parameter have been computed using the three values of alpha in respect time used from Houben et al. (2012). Table 1 and Figure 38 show the chosen value for the time and the corresponding values of alpha, interpolated from data obtained by Houben et al (2013).

Time [days]	Time [s]	α
1	8,64E+04	1,162E-03
2	1,73E+05	1,140E-03
5	4,32E+05	1,075E-03
7	6,05E+05	1,032E-03
9	7,78E+05	9,870E-04
12	1,04E+06	9,250E-04
14	1,21E+06	8,800E-04
30	2,59E+06	5,35E-04

Table 1: computed alpha.

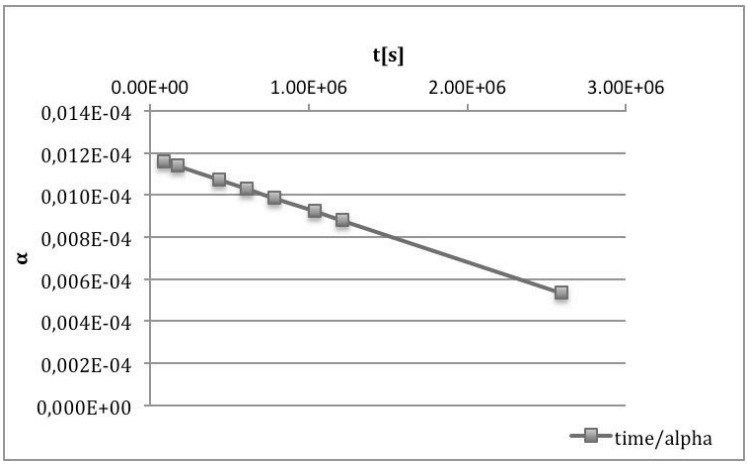

Figure 38: Values of alpha.

Previous studies (Watanabe and Peach, 2002; de Meer et al., 2005; Koelemeijer et al., 2012) provide several values for diffusion coefficient and thickness of fluid film, showing a connection between the two parameters. For this reason, four different values of diffusion coefficient were used in relationship with the thickness of the fluid film to understand the sensitivity of the model to the parameter $\frac{DC\delta}{a}$ considering C= 0,1675 (Table 2).

	δ/a [m]	DCδ/a [m³/s]
D=10E-9 [m²/s] δ=280E-9 [m]	9,00E-13	1,96E-22
D=10E-12 [m²/s] δ=90E-9 [m]	2,89E-13	6,30E-23
D=10E-15 [m²/s] δ=50E-09 [m]	1,61E-13	3,50E-23
D=10E-18 [m²/s] δ=1E-09 [m]	3,21E-15	7,00E-25

Table 2: Diffusion coefficient in relation with the thickness of the fluid film.

These are used to predict the cusp migration with time (parameter x). The values used for the constants are: γ_{SL}= 0,129 [J/ m²]; γ_{Lv} = 0,064 [J/ m²]; Ω= 2,70E-5 [m³/mol]; R= 8,314 [K/Kmol]; T= 296 [K]. Value of x, as function of DCδ/a, are calculated to be:

	DCδ/a=1,96E-22	DCδ/a=6,30E-23	DCδ/a=3,50E-23	DCδ/a=7,00E-25
t [s]	x [µm]	x [µm]	x [µm]	x [µm]
8,64E+04	73,5	55,3	47,7	18
1,73E+05	88,6	66,7	57,6	22
4,32E+05	116	87,7	75,7	29
6,05E+05	131	98,8	84,9	32
7,78E+05	144	108	93,5	35
1,04E+06	162	122	105	40
1,21E+06	175	132	114	43
2,59E+06	308	232	200	75

Table 3: Different values for DCδ/a.

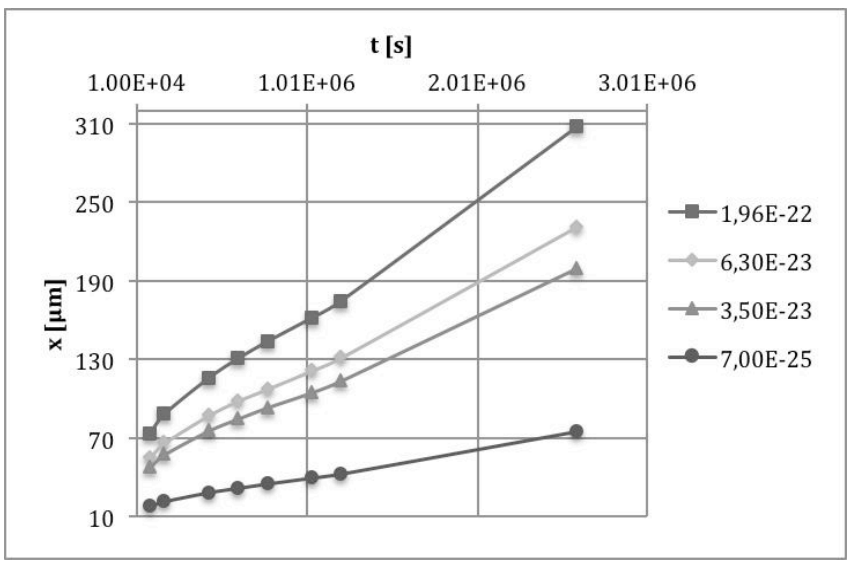

Figure 39: Diagram distance versus time obtained using different values for DCδ/a.

The diagrams show that using bigger values of D and δ (10E-9 and 280E-9 respectively) it is possible to obtain higher values of migration distance, meaning that the healing process would be faster. At the contrary, smaller value of $\frac{DC\delta}{a}$ lead to a smaller value for the migration distance and consequently to a slower healing process (Figure 40).

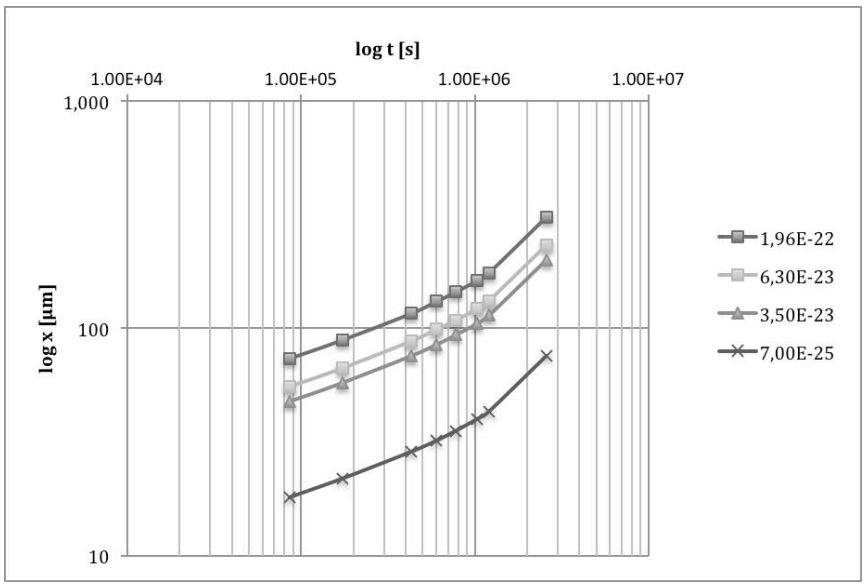

Figure 40: Summary of distance versus time in log scale for a crack with a thickness around 3 µm.

4.3. Comparison between the best fit for the model by Houben and the data obtained by varying DCδ/a

Using $\log t \frac{4DC\Omega(\gamma_{SL}+\gamma_{LV})}{\pi RT\alpha^3} = \log \frac{a}{\delta} \frac{x^4}{\cos\theta/2}$ it was possible to compare the values of x obtained using the range of values for DCδ/a found in the literature (Watanabe and Peach, 2002; de Meer et al., 2005; Koelemeijer et al., 2012) with the values of DCδ/a used by Houben et al (2013) in their experiments. We obtained a diagram cusp migration versus time (Figure 41) using, once again, different values for diffusion coefficient and thickness (Table 4). The red line represent the model by Houben, indicating that their model is valid and give the best fit of 9E-13 for δ/a, with a value of 1,96E-22 for DCδ/a.

DCδ/a=1,96E-22		DCδ/a=6,30E-23		DCδ/a=3,50E-23		DCδ/a=7,00E-25	
t/A	a/δ*x4	t/A	a/δ*x4	t/A	a/δ*x4	t/A	a/δ*x4
3,23E-05	3,20E-11	3,23E-05	1,03E-11	3,23E-05	5,72E-12	3,23E-05	1,14E-13
6,85E-05	6,78E-11	6,85E-05	2,18E-11	6,85E-05	1,21E-11	6,85E-05	2,42E-13
2,04E-04	2,02E-10	2,04E-04	6,50E-11	2,04E-04	3,61E-11	2,04E-04	7,22E-13
3,23E-04	3,20E-10	3,23E-04	1,03E-10	3,23E-04	5,71E-11	3,23E-04	1,14E-12
4,75E-04	4,70E-10	4,75E-04	1,51E-10	4,75E-04	8,40E-11	4,75E-04	1,68E-12
7,69E-04	7,62E-10	7,69E-04	2,45E-10	7,69E-04	1,36E-10	7,69E-04	2,72E-12
1,04E-03	1,03E-09	1,04E-03	3,32E-10	1,04E-03	1,84E-10	1,04E-03	3,69E-12
9,94E-03	9,84E-09	9,94E-03	3,16E-09	9,94E-03	1,76E-09	9,94E-03	3,52E-11

Table 4: Different values for DCδ/a.

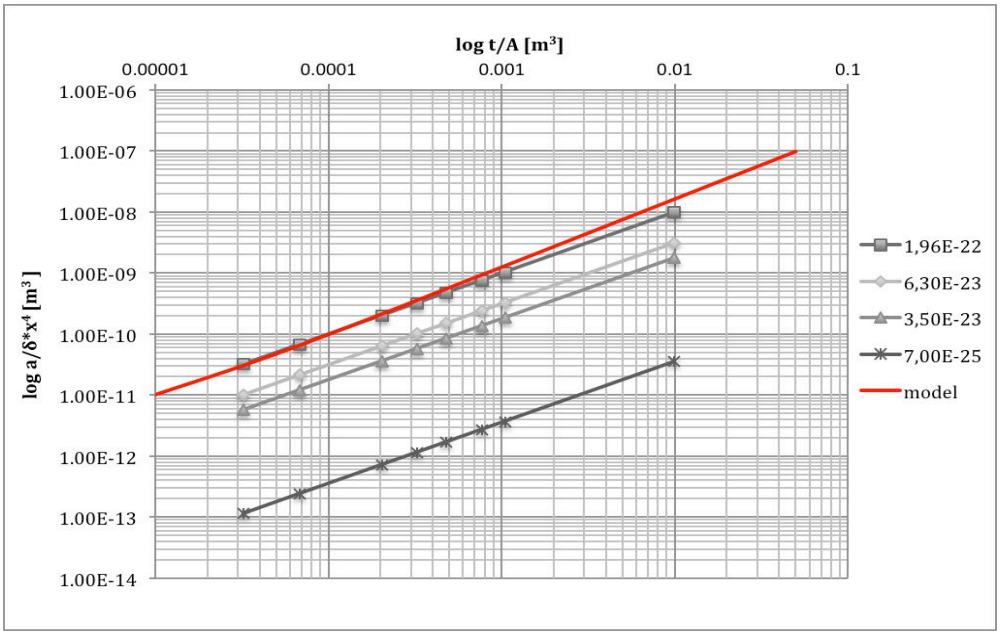

Figure 41: Model from Houben et al, 2013 (in red), compared to the results obtained varying DCδ/a for a crack with a thickness around 3 µm.

4.4. Experiment

4.4.1. Preparation

Samples were prepared from salt powder with a grain size of >1mm and for each samples were used ~0.5 g of NaCl, saturated brine and a maximum applied stress of ~230 MPa (in ~5 minutes). The specimens were then compacted wet with sufficient pore fluid to fill the remaining porosity after compaction, but only partially saturated prior to compaction (4-8 drops of saturated brine: 0.02-0.04 ml). During compaction, fluid was expelled from each sample, suggesting that the pore volume was

completely filled with brine. Graphite coating was applied to sample VD13 and VD10 to reduce friction during compaction, but proved to have little effect, therefore it was not used further.

All samples were compacted to ~4.5 kN force and frozen for 45-90 minutes. The shrinkage of the salt during freezing, which was more than that of the steel container, helped to remove the sample from the container. After freezing, the samples were carefully pressed out at a minimum force of 1.5-2 kN, which gradually decreases at the sample slides out of the compaction vessel. Porosity was estimated based on the volume of the sample (length and diameter) and the known mass of salt used to prepare the samples, assuming no mass loss. Note that the porosity is only an average estimate of the whole sample, though porosity may be distributed heterogeneously. Almost all samples appeared to be more porous on one end, after visual inspection.

The cylindrical salt samples were then immediately glued into a section of heat shrink tube, coated internally with Araldite resin, and sealed on both ends with more resin to keep the water present within the samples contained. Table 5 shows the information on all the prepared samples with VD00 as a reference sample (dry).

Scans were made at 160 kV scanning voltage and 2 mm Al filter with a total scanning area of 2000x2000 pixels and a resolution of 2.6 μm. The number of scans is 2400, but edges were discarded due to distortion so that 1600 scans were analysed for each sample.

Sample name	Sample length at start [mm]	Sample length after compaction [mm]	Fluid volume [drops]	Estimated porosity [%]	Date created	Age when scanned [days]
VD00	22.60	12.75	4	7.5		1
VD14	22.65	12.30	6	4.2	8/8/2017	1, 2, 3
VD12	22.00	12.25	6	3.8	7/8/2017	3
VD13	22.60	12.75	4	7.5	8/8/2017	1, 3
VD10	22.55	12.50	6	5.7	4/8/2017	7
VD07	22.90	12.30	6	4.2	31/7/2017	10, 11
VD08	21.60	11.80	4	<1	31/7/2017	11
VD06	21.95	12.10	8	2.6	28/7/2017	12
VD01	22.60	11.85	4	<1	10/7/2017	30

Table 5: Samples used for CT-scan imaging.

4.4.2. Results

4.4.2.1. Sample description

Scans were analysed using the image sequence in ImageJ to have an overview of the characteristic of each sample. Note that in the images salt rock is in greyish, cracks are black and the resin in dark grey. Due to the highly hydrophilic nature of salt, the resin easily penetrated any cracks connected to the outer surface of the sample.

- The reference sample, *VD00* (Figure 42), shows a higher porosity in respect the other scanned samples. The resin used during preparation seems to be within the cracks and air bubbles are trapped in the pores. In general the cracks appear wider than in the wet samples.

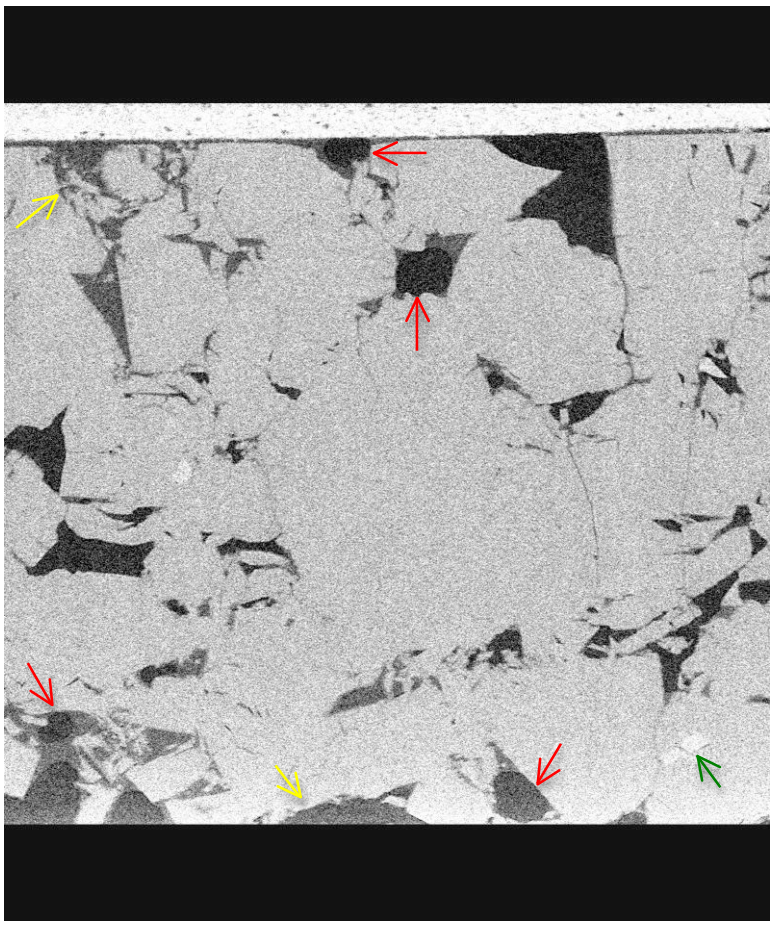

Figure 42: Orthogonal view of VD00 (dry reference sample, no healing expected with time). Presence of air bubbles (red arrows), resin within the cracks (yellow arrow) and impurities (green arrow). Measured horizontal length of the sample is 4 mm.

- *VD14* was scanned at day 1, day 2 and day 3. In general, the scans show a lower porosity then the reference dry sample and cracks look irregular and with air bubbles within the pores. Furthermore the top of the sample seems to have wider cracks than the bottom. Figure 43 show cracks evolution from day 1 to day 3; differences of scans at day 1-2-3 were analysed in section 4.4.2.2.

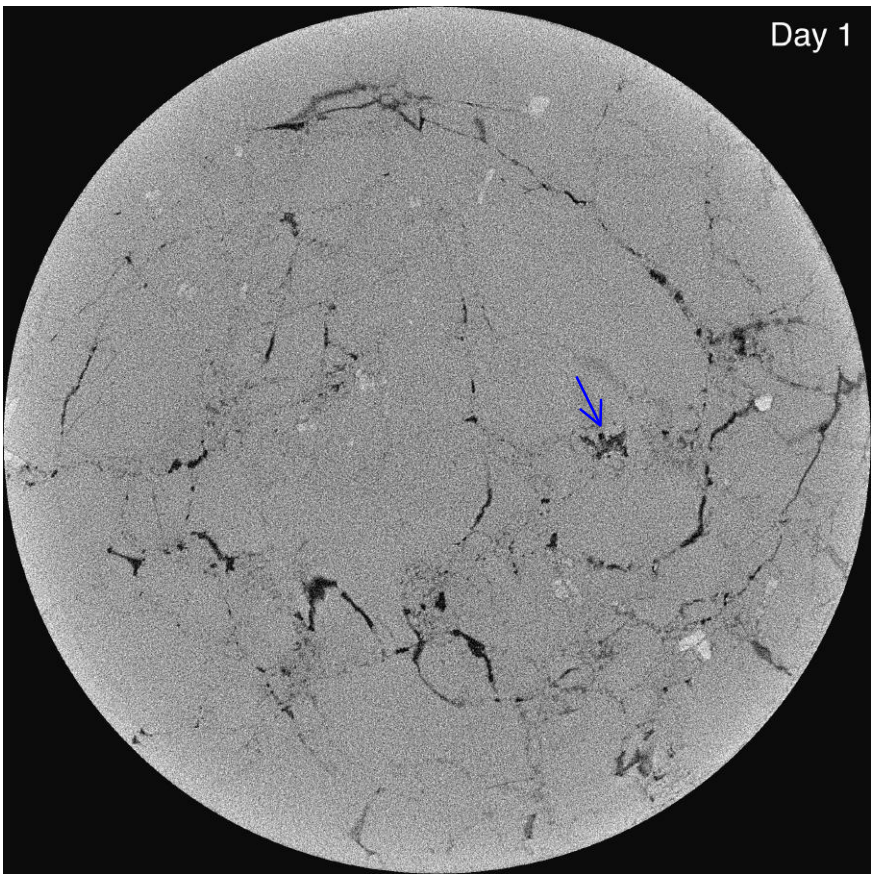

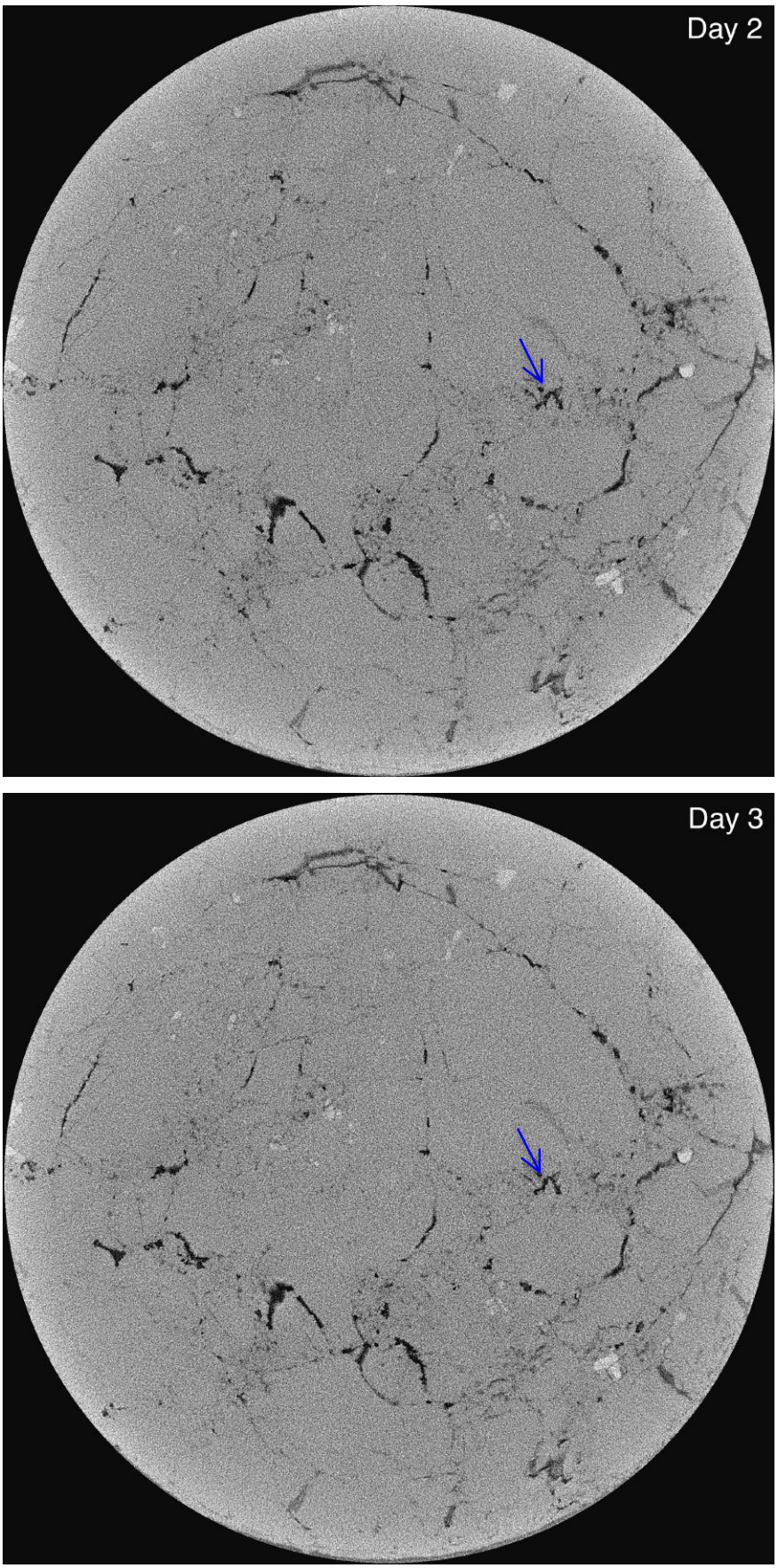

Figure 43: Cracks evolution in sample VD14. Note the crack highlighted by the blue arrow. Measured diameter of the sample is 5mm.

- In VD12 (3 days after preparation) the top part of the sample seems less porous than the bottom and there is no presence of air bubbles. In general cracks appear thinner then in VD14, probably due to a lower estimated porosity (Figure 44).

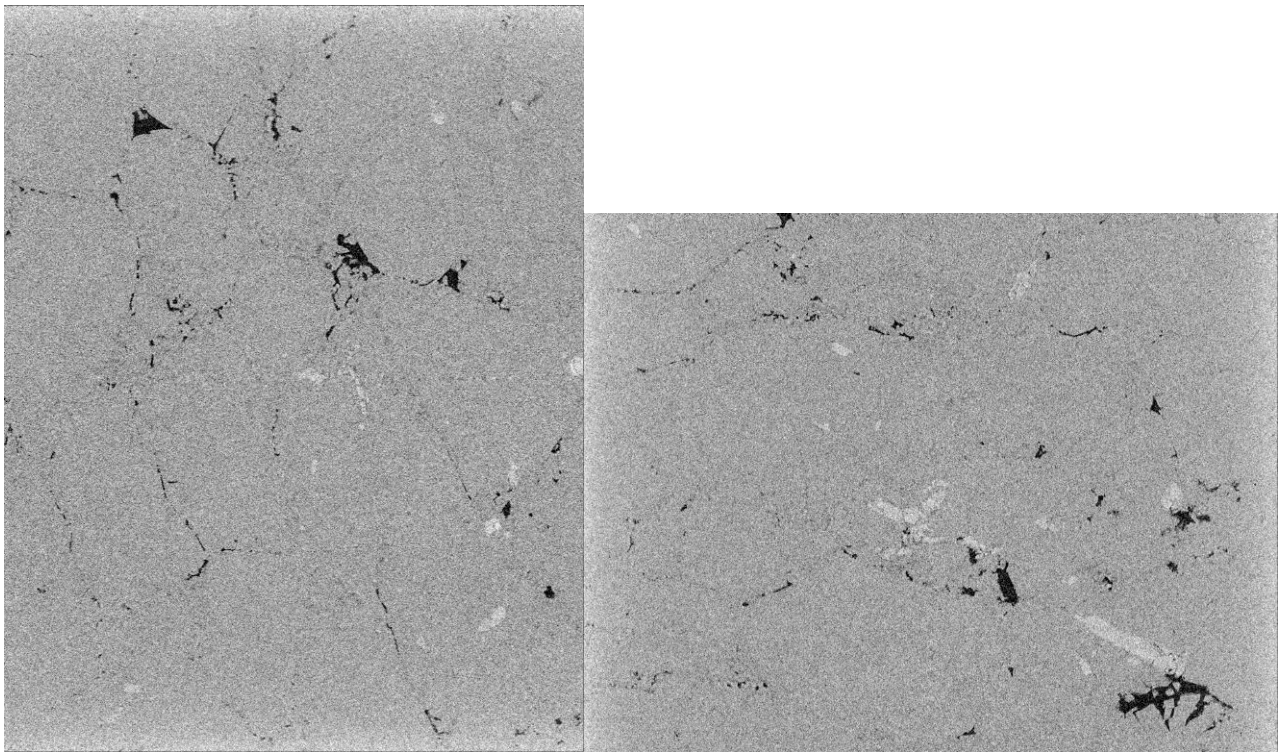

Figure 44: Orthogonal view of VD12 (3 days after preparation). Image on the left: measured horizontal length is 4 mm; image on the right: measured horizontal length is 5.2 mm.

- *VD07* was scanned at day 10 and 11 (i.e. the time of potential healing). Cracks look more irregular and not really connected between each other. The sample seems characterized by thinner cracks in most of the scans and the remaining seems to have thicker cracks with a sub-polygonal shape. Air bubbles within the pores seem absent and in general the amount of cracks seems to be less then VD14 (1-2-3 days after preparation, but with the same estimated porosity). Figure 45 show cracks evolution from day 10 to day 11.

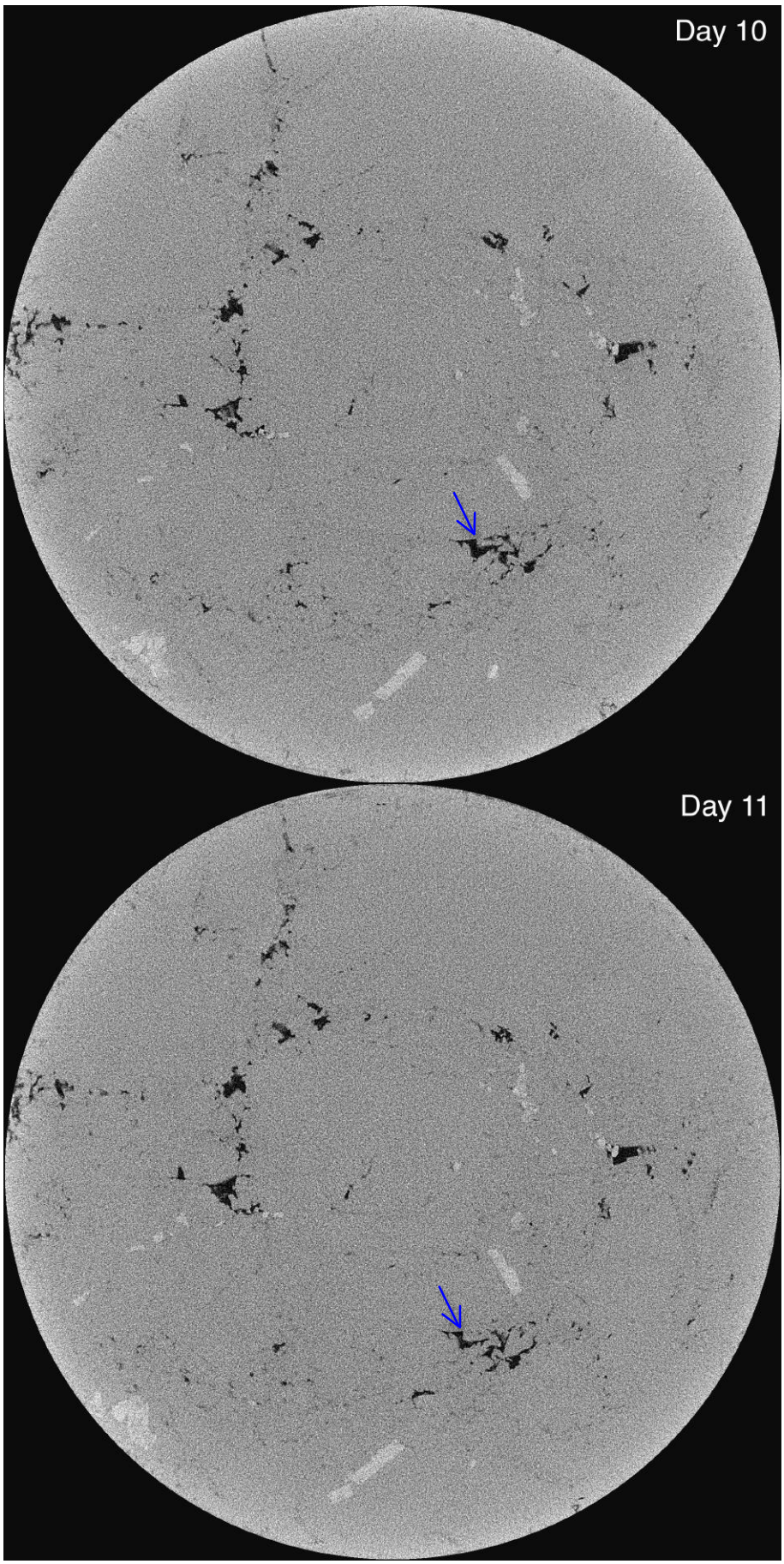

Figure 45: Cracks evolution in sample VD07. Note the crack highlighted by the blue arrow. Measured diameter of the sample is 5mm.

- *VD08* (11 days since preparation) results to be less porous then the previous samples, in particular in the middle scans. As in sample VD07 air bubbles are absent but the resin within the pores is still noticeable (Figure 46). In general, cracks look irregular but some of them have a tubular or polygonal shape.

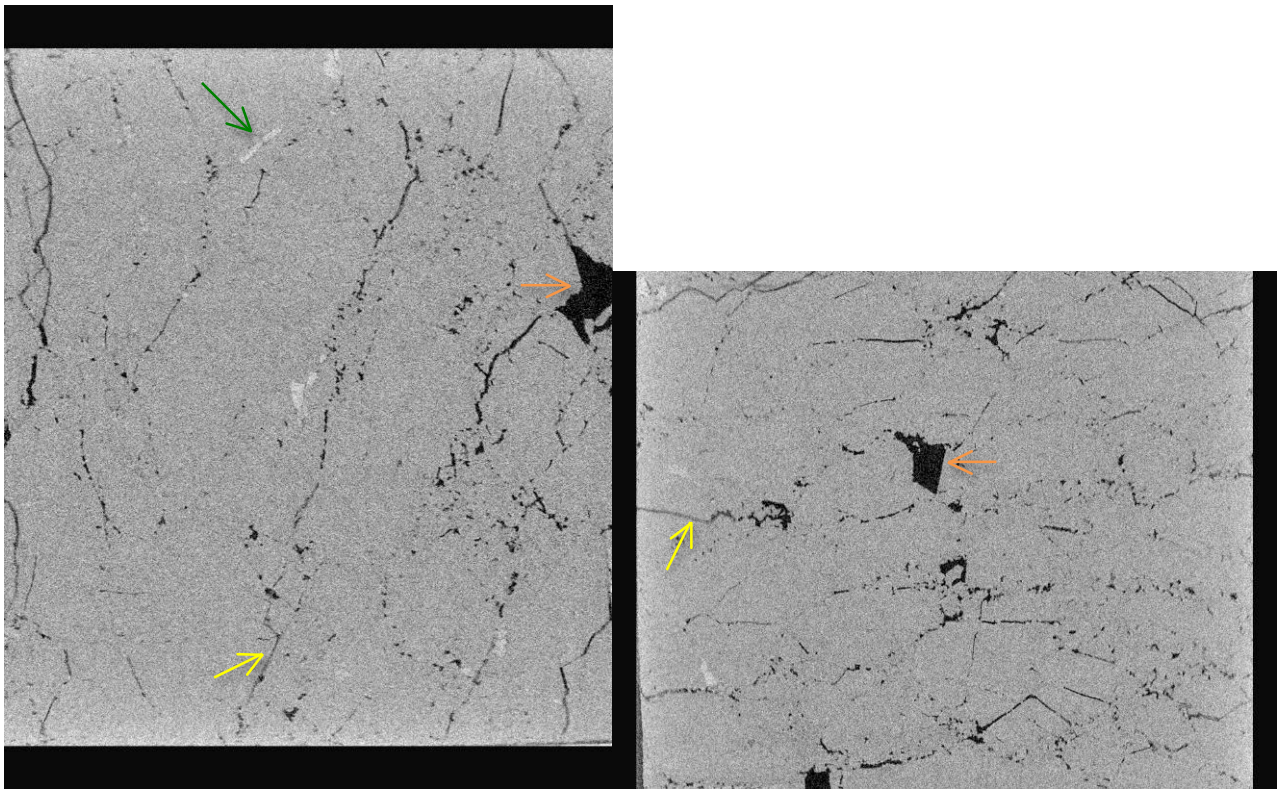

Figure 46: Orthogonal view of VD08 (11 days after preparation). Resin still present within the pores (yellow arrows); few impurities (green arrow) and most of the crack are irregular and tubular-shaped, few of them have a subpoligonal shape (orange arrows). Image on the left: measured horizontal length is 4 mm; image on the right: measured horizontal length is 5.2 mm.

- In sample *VD06* (12 days after preparation) air bubbles are not visible, cracks look again thinner and irregular compared to samples scanned at day 1-2-3 (Figure 47).

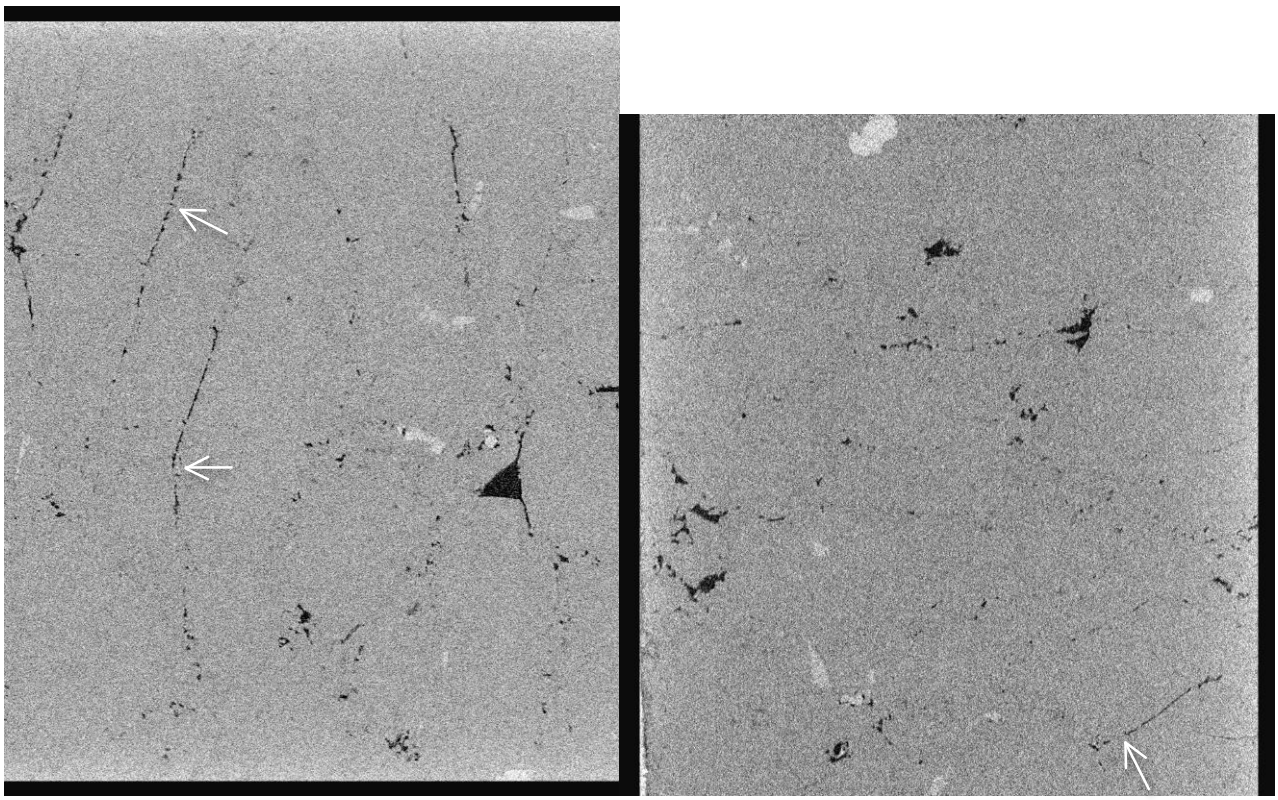

Figure 47: Orthogonal view of VD06 (12 days after preparation). Thin and non-continuous cracks (white arrows); note the absence of air bubbles within the pores. Image on the left: measured horizontal length is 4 mm; image on the right: measured horizontal length is 5.2 mm.

- *VD01* (30 days after preparation) has very low porosity in respect to the other samples and more similar to sample VD08. The amount of cracks is lower in respect to VD08 and they look really thin and irregular and in some points not connected between each other (Figure 48).

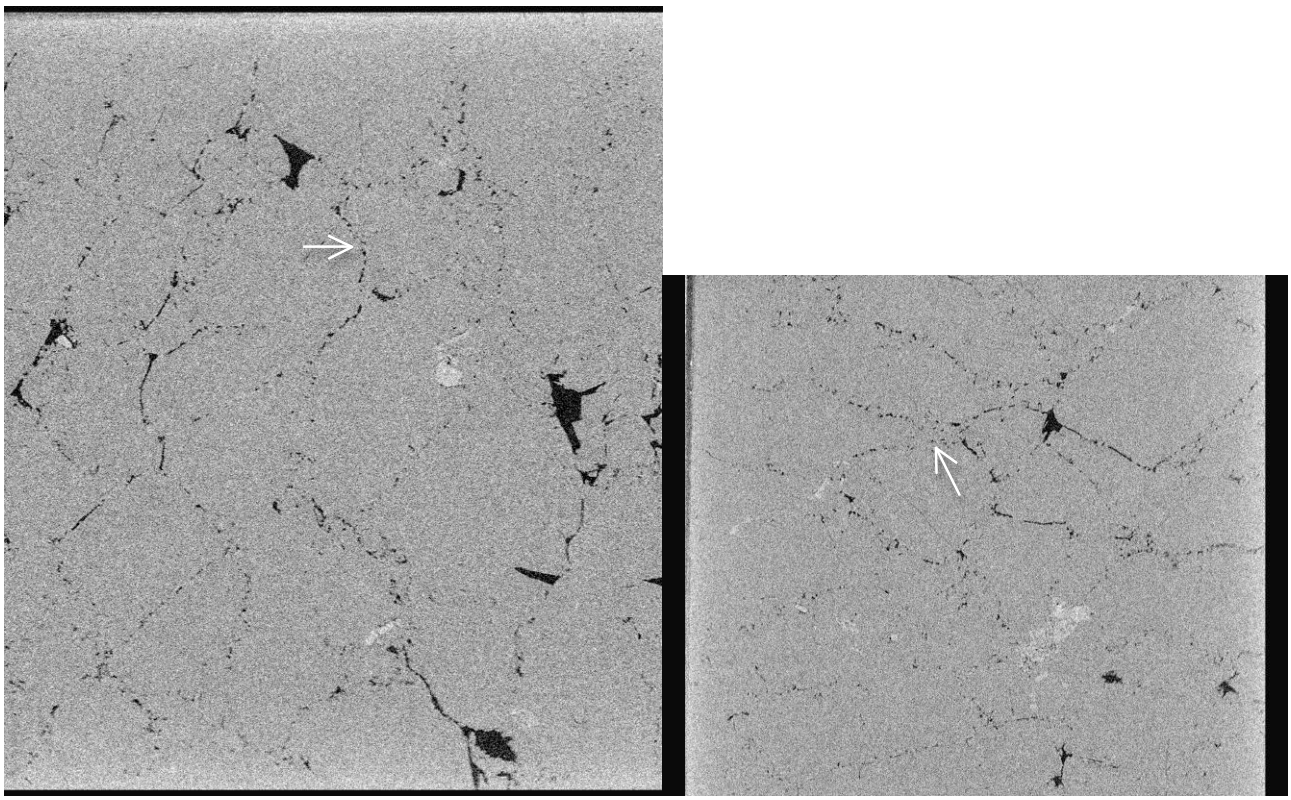

Figure 48: Orthogonal view of VD01 (30 days after preparation). Thin cracks that seem disconnected between each other (white arrows). No sign of resin or air bubbles within the pores. Image on the left: measured horizontal length is 4 mm; image on the right: measured horizontal length is 5.2 mm.

In general, samples scanned at day 1, 2 and 3 seem to contain air bubbles and resin within the cracks, except for VD12 probably due to its lower porosity; while they are absent in samples scanned at day 10, 11, 12 and 30 in which the estimated porosity is lower. The estimated porosity of most of the samples is different so direct comparison is not possible, but it is clear that samples scanned at later days are characterized by thinner cracks, the network connection between them seems weaker and grain boundaries are difficult to identify.

4.4.2.2. Sample comparison and measurements

With the aim of investigating cracks evolution and healing in salt rock, sample VD14 was used to measure the cracks and estimate the progress of crack healing for a time period of 3 days (1-3 days after sample preparation). Furthermore, samples VD08 (11 days since preparation) and VD01 (30 days after preparation) and samples VD14 (one day after preparation) and VD07 (11 days since preparation) were used for a more general comparison due to their similar estimated porosity. Cracks measurements were done on images from orthogonal views of each sample using ImageJ. Due to issues with the orthogonal view (even using the same images and orthogonal views a match between them was not possible) crack measurements of VD14 at day one and VD07 at day 10 and 11 were not possible. However, we present crack measurements for images of VD14 scanned at day 2-3.

4.4.2.2.1. VD14 (day 2-3)

Crack measurements (Figure 49-53 and Table 6-10) were done selecting and comparing representative orthogonal views of scans made at day 2-3 and using the ROI manager of ImageJ to obtain a measurement of crack length for resin-free cracks. Furthermore, for cracks with a more polygonal shape, width measurements were taken together with the length (Figure 49 for a magnified view of the width measurements). The estimated error for crack measurements is around 0.2 E^{-4}-0.4E^{-4} m.

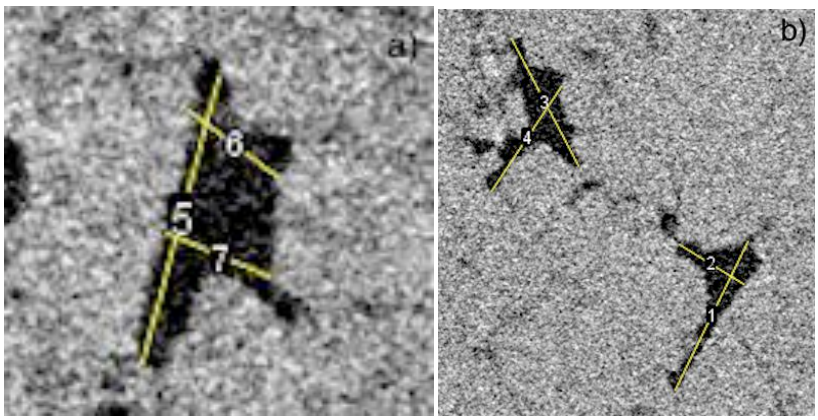

Figure 49: View of a) crack measurements on stack 1 and b) crack measurements on stack 2.

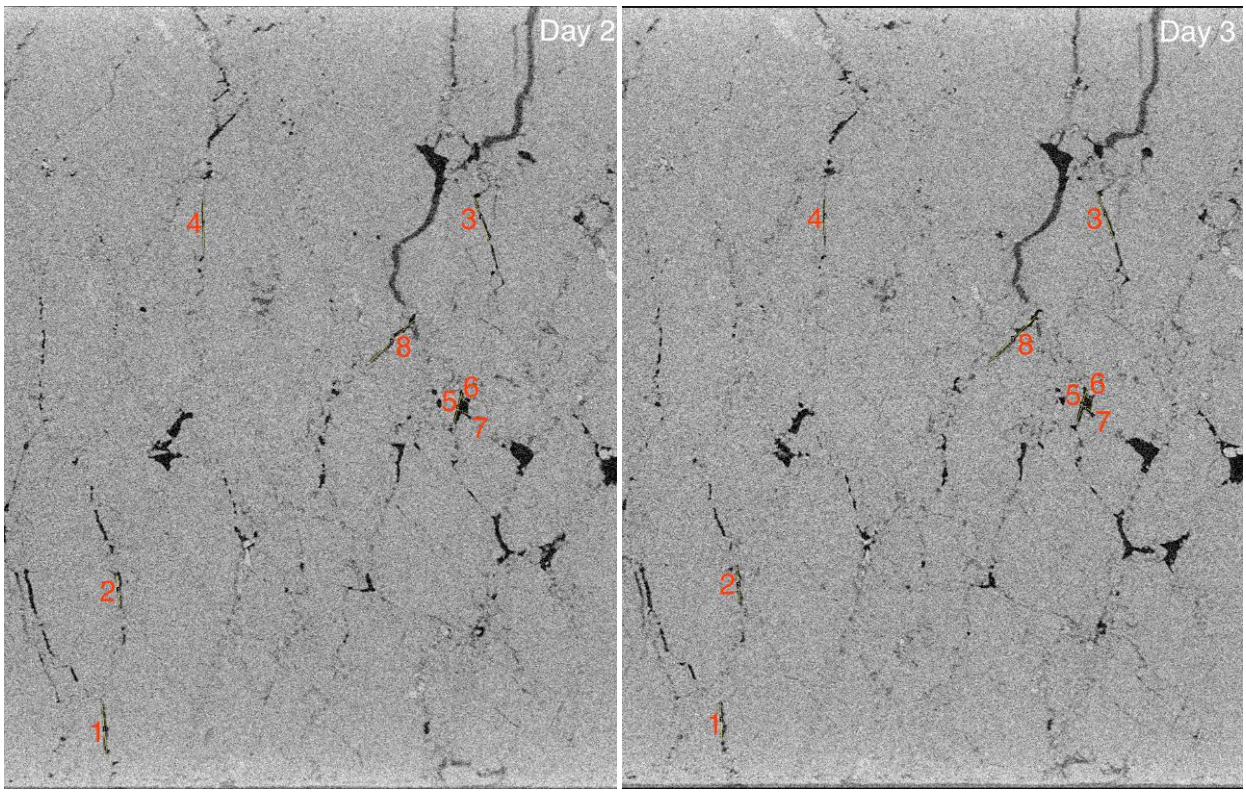

Figure 50: Location of crack measurements, stack 1 VD14. Measured horizontal length is 4 mm.

Stack 1 XZ 1000-YZ100	VD14 day 2 Length [m]	VD14 day 3 Length [m]	Difference [µm]
1	3.422E-4	2.355E-4	112
2	2.482E-4	2.44E-4	4
3	3.240E-4	3.232E-4	1
4	3.237E-4	2.88E-4	35
5	2.203E-4	2.196E-4	1
6 (width)	7.657E-5	6.890E-5	7.67
7 (width)	7.810E-5	7.590E-5	2.2
8	4.346E-4	4.327E-4	2

Table 6: Crack length, and occasionally width, measurements, stack 1 VD14.

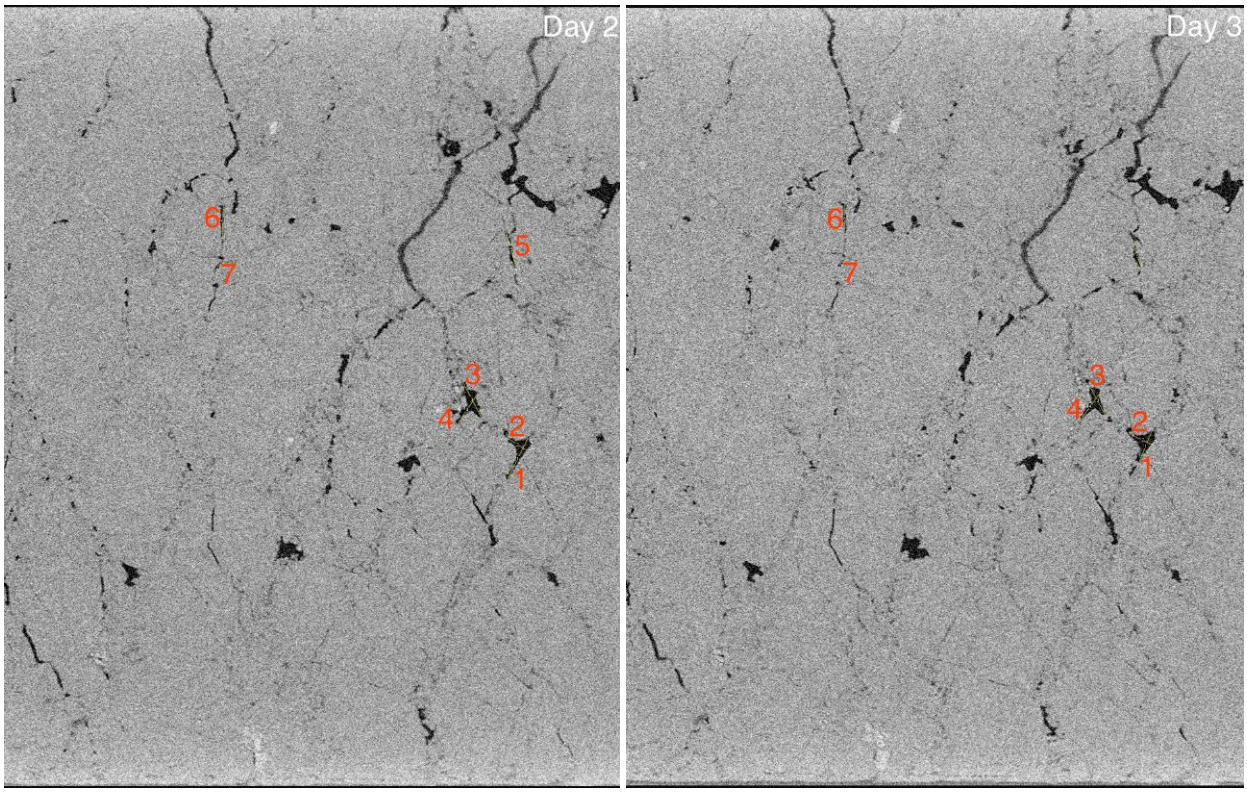

Figure 51: Location of crack measurements, stack 2 VD14. Measured horizontal length is 4 mm.

Stack 2 XZ 510-YZ 1083	VD14 day 2 Length [m]	VD14 day 3 Length [m]	Difference [µm]
1	3.041E-4	2.255E-4	79
2 (width)	1.371E-4	1.279E-4	10
3 (width)	2.628E-4	2.070E-4	56
4	2.307E-4	1.999E-4	32
5	2.424E-4	1.508E-4	92
6	2.115E-4	1.924E-5	192
7	7.828E-5	5.440E-5	23

Table 7: Crack length, and occasionally width, measurements, stack 2 VD14.

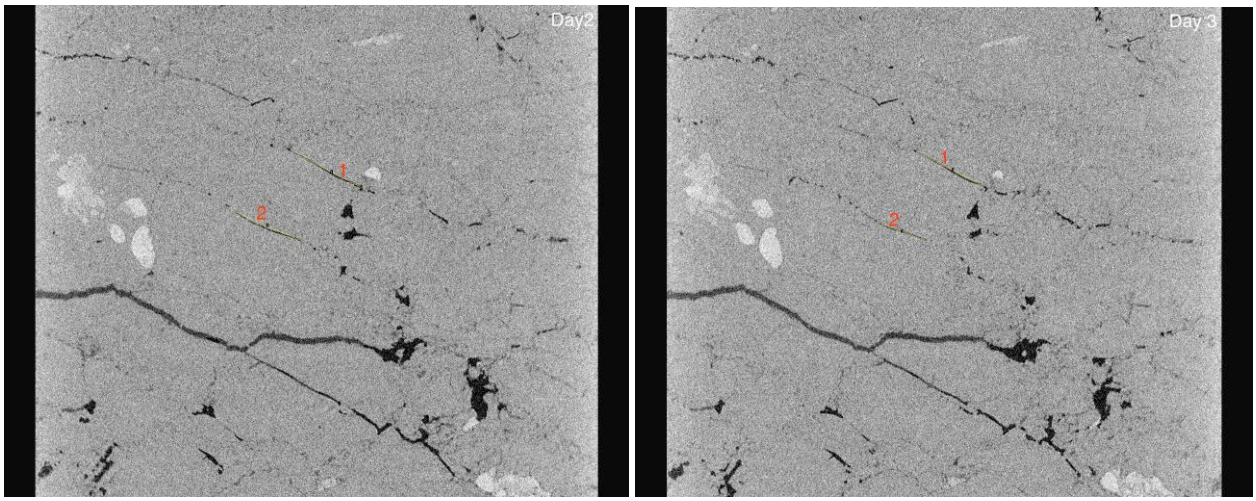

Figure 52: Location of crack measurements, stack 3 VD14. Measured horizontal length is 5.2 mm.

Stack 3 XZ 567-YZ 381	VD14 day 2 Length [m]	VD14 day 3 Length [m]	Difference [µm]
1	5.773E-4	5.357E-4	42
2	5.849E-4	4.217E-4	163

Table 8: Crack length, and occasionally width, measurements, stack 3 VD14.

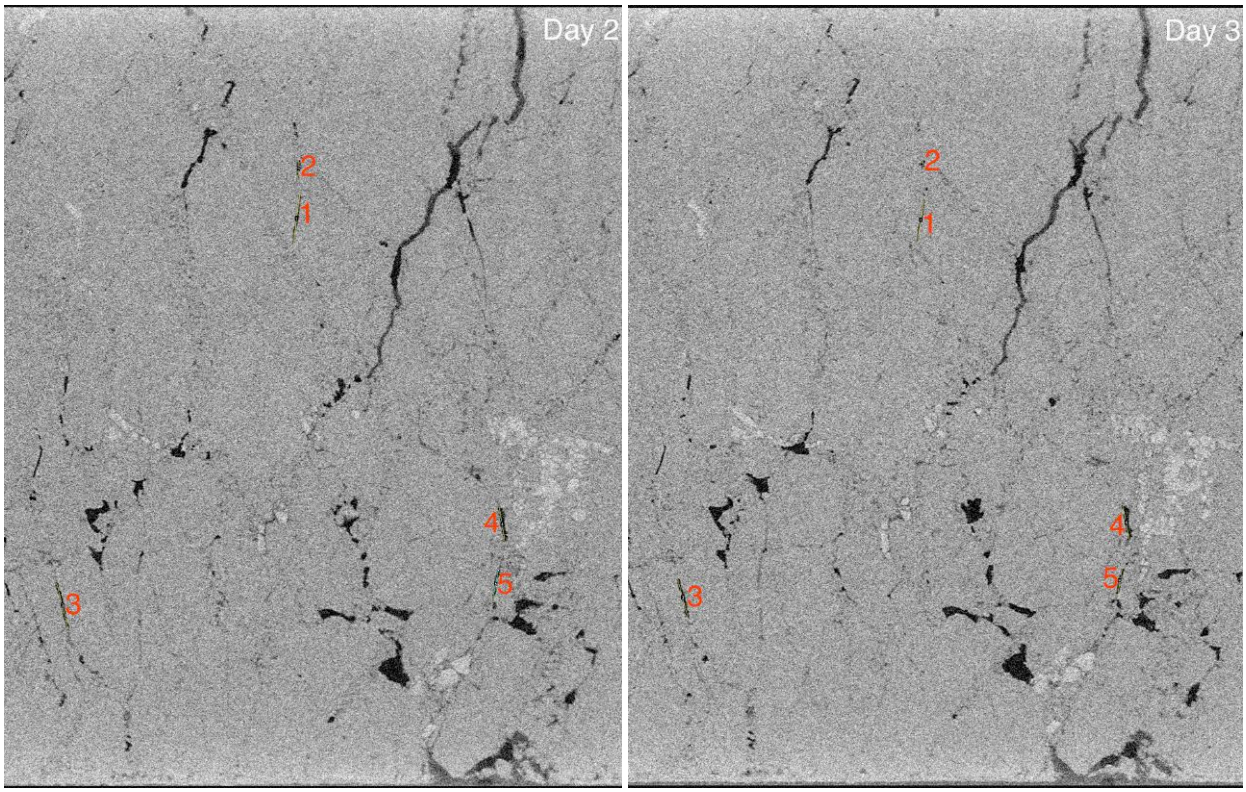

Figure 53: Location of crack measurements, stack 7 VD14. Measured horizontal length is 4 mm.

Stack 7 XZ 1644-YZ 918	VD14 day 2 Length [m]	VD14 day 3 Length [m]	Difference [µm]
1	3.322E-4	2.645E-4	68
2	1.267E-4	4.942E-5	77
3	3.058E-4	2.589E-4	47
4	2.396E-4	2.292E-4	10
5	1.800E-4	1.609E-4	19

Table 9: Crack length, and occasionally width, measurements, stack 7 VD14.

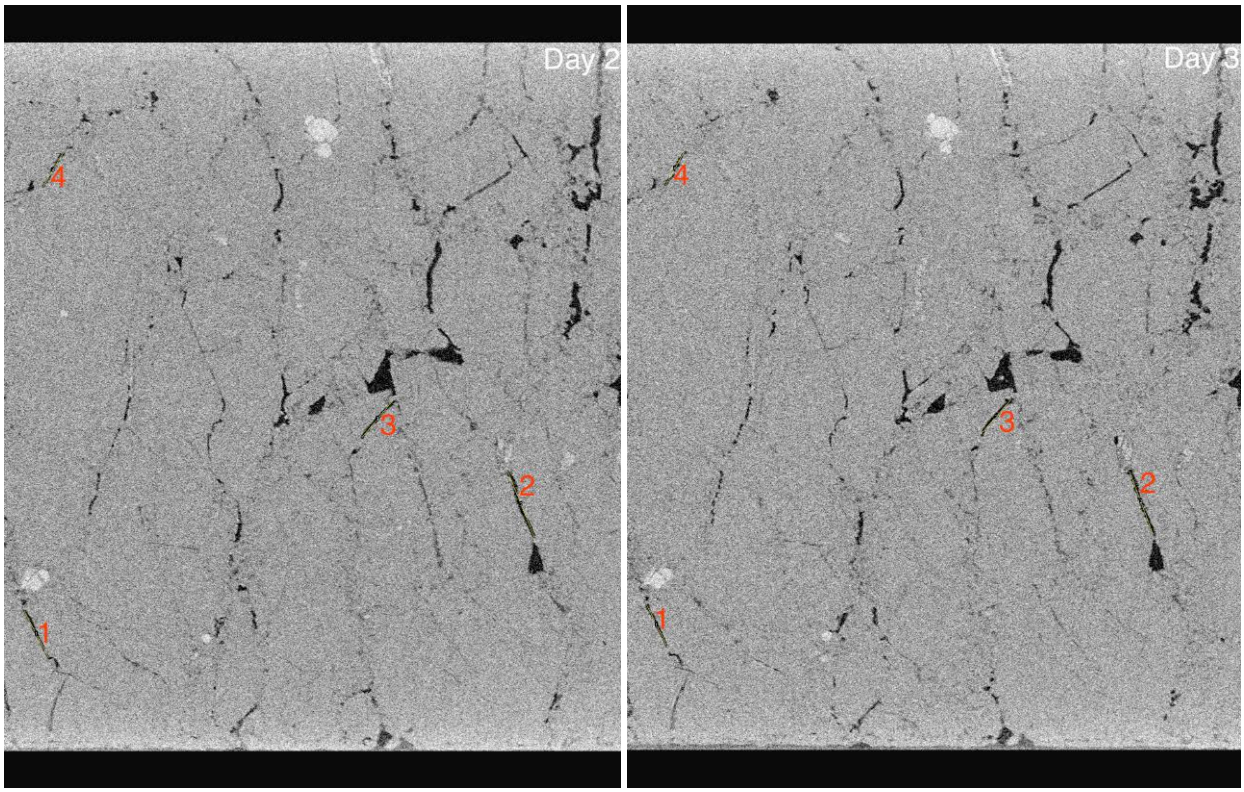

Figure 54: Location of crack measurements, stack 9 VD14. Measured horizontal length is 4 mm.

Stack 9 XZ 264-YZ 1422	VD14 day 2 Length [m]	VD14 day 3 Length [m]	Difference [µm]
1	3.551E-4	2.861E-4	69
2	4.590E-4	4.317E-4	27
3	3.174E-4	3.004E-4	17
4	2.586E-4	2.492E-4	9.4

Table 10: Crack length, and occasionally width, measurements, stack 9 VD14.

4.4.2.2.2. VD08 and VD01: similar estimated porosity, different ages

As already said in the previous section, sample VD08 and VD01, scanned at day 11 and 30 respectively, have similar estimated porosity and even if a direct comparison is not possible, the two samples might give qualitative information about crack healing on a longer period of time. Orthogonal views of both

the samples are shown in Figure 55-56, where a different amount of cracks and change in crack size is clearly visible. Cracks in sample VD08 (11 days) look thicker and elongated and show a pattern that is not really noticeable in sample VD01 where the orientation seems random and cracks look discontinuous and not connected between each other.

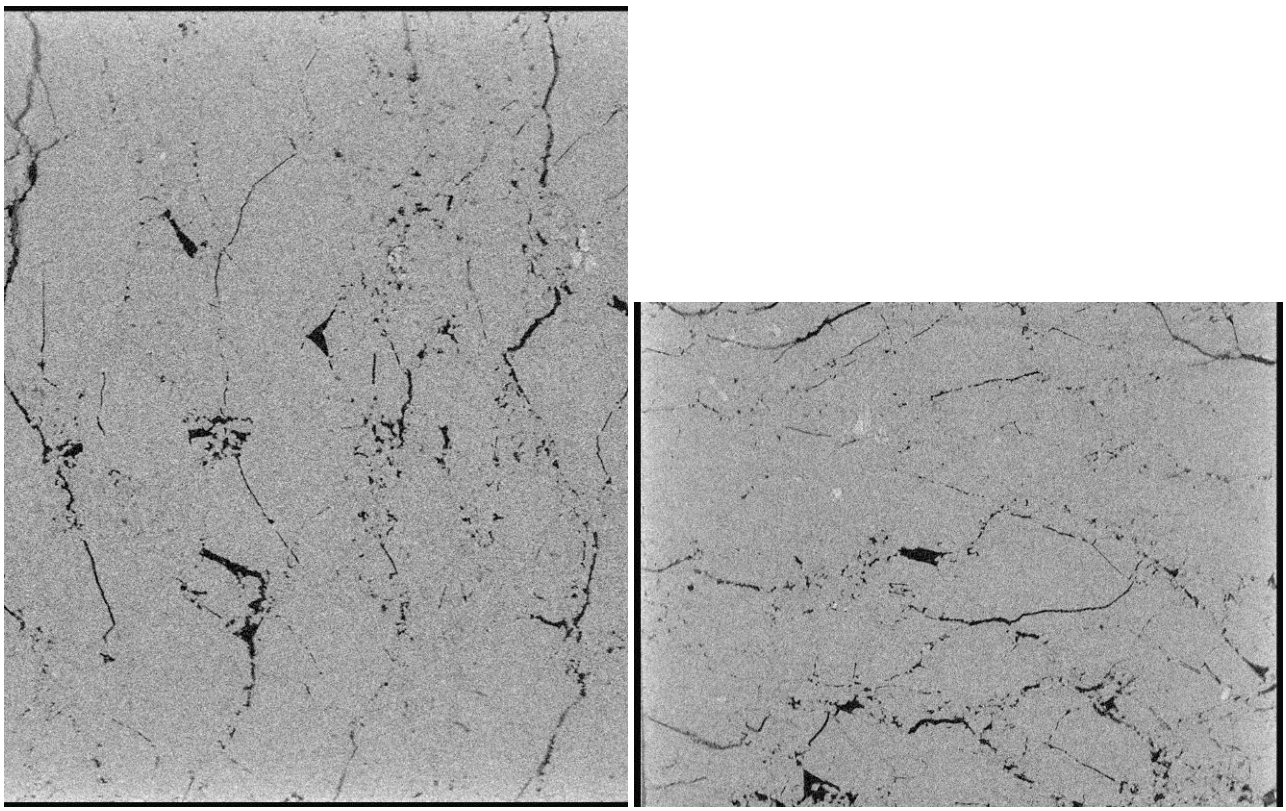

Figure 55: Orthogonal view of VD08. Image on the left: measured horizontal length is 4 mm; image on the right: measured horizontal length is 5.2 mm.

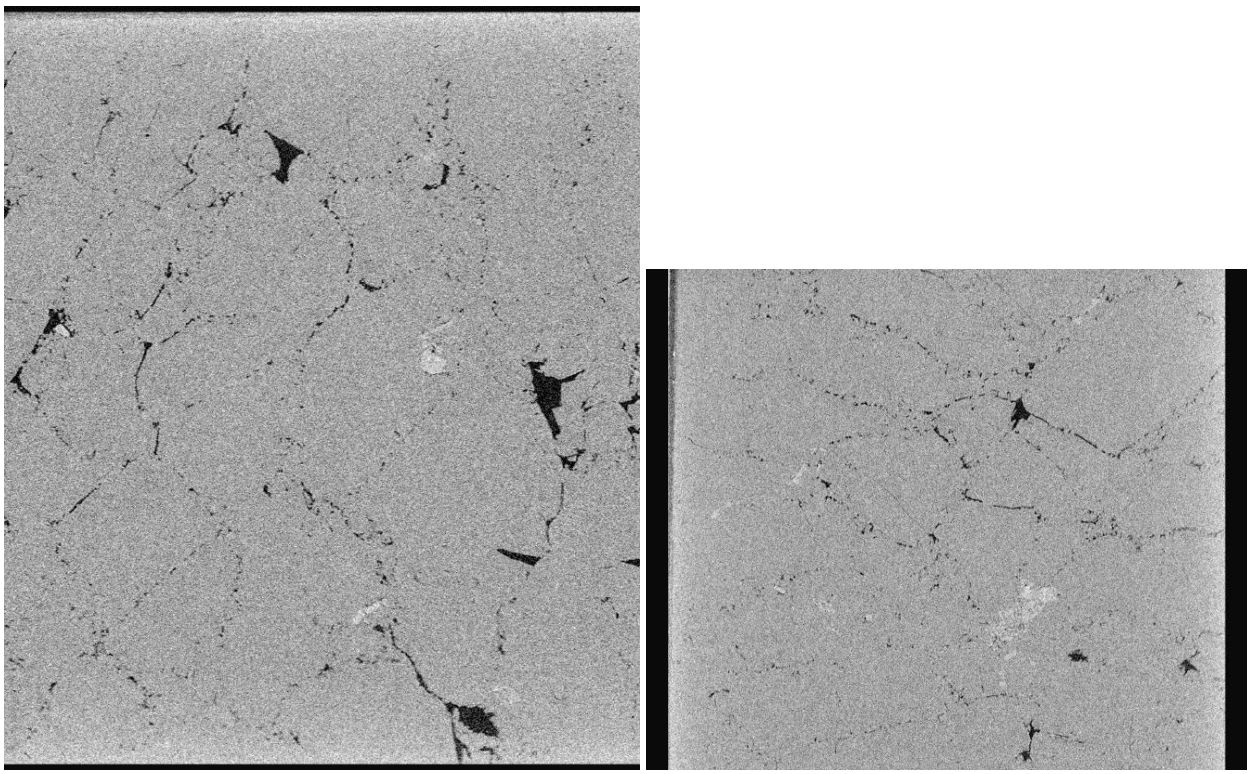

Figure 56: Orthogonal view of VD01. Image on the left: measured horizontal length is 4 mm; image on the right: measured horizontal length is 5.2 mm.

4.4.2.2.3. VD14 and VD07: similar estimated porosity, different ages

For this comparison, orthogonal views from VD14 day 1 and VD07 day 11 were chosen to examine crack evolution, as they had similar estimated initial porosity. As shown in Figure 57-58, the sample are characterized by different crack size, VD14 shows wider cracks that seem to form a network, original salt grains are clearly visible and grain boundaries are sharp; while in VD07 crack are thinner, non-continuous and without a pattern, with less-defined grain boundaries. Furthermore, sample VD14 shows clear resin-filled cracks, which will not display crack-healing with time.

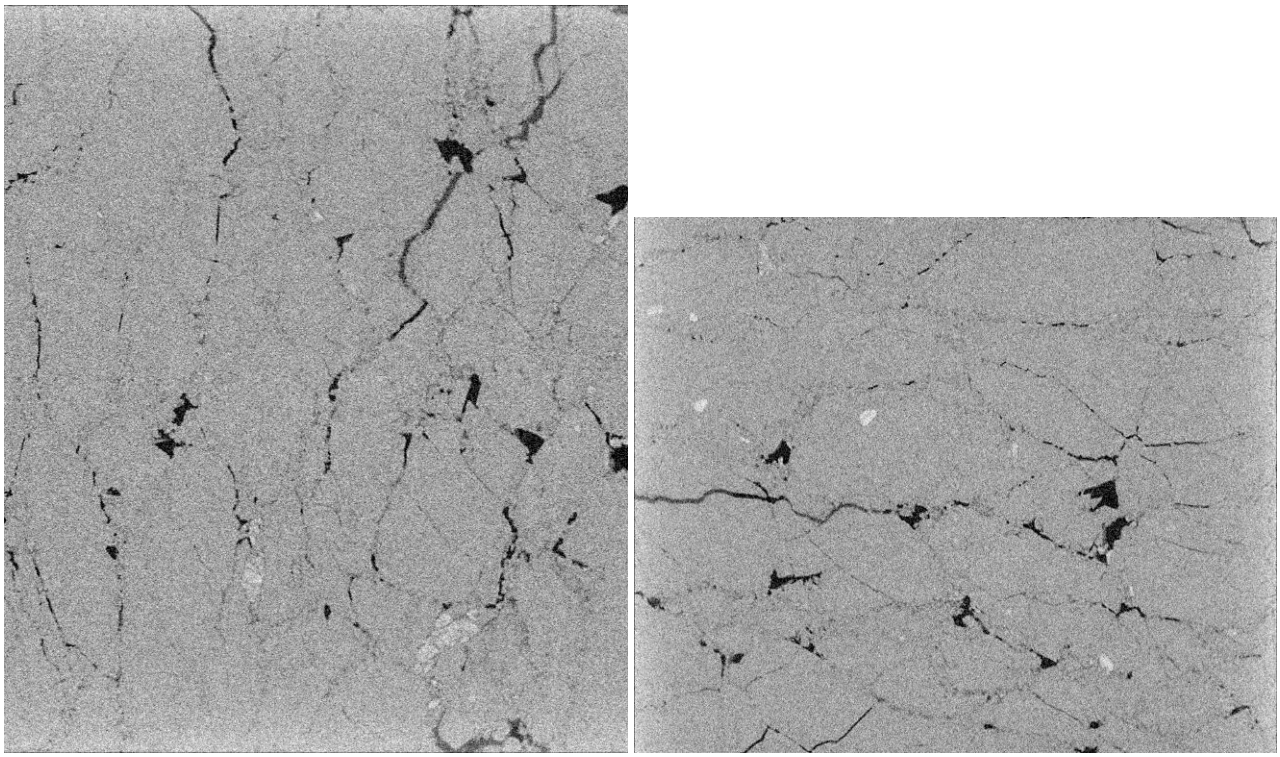

Figure 57: Orthogonal view of VD14 day 1. Image on the left: measured horizontal length is 4 mm; image on the right: measured horizontal length is 5.2 mm.

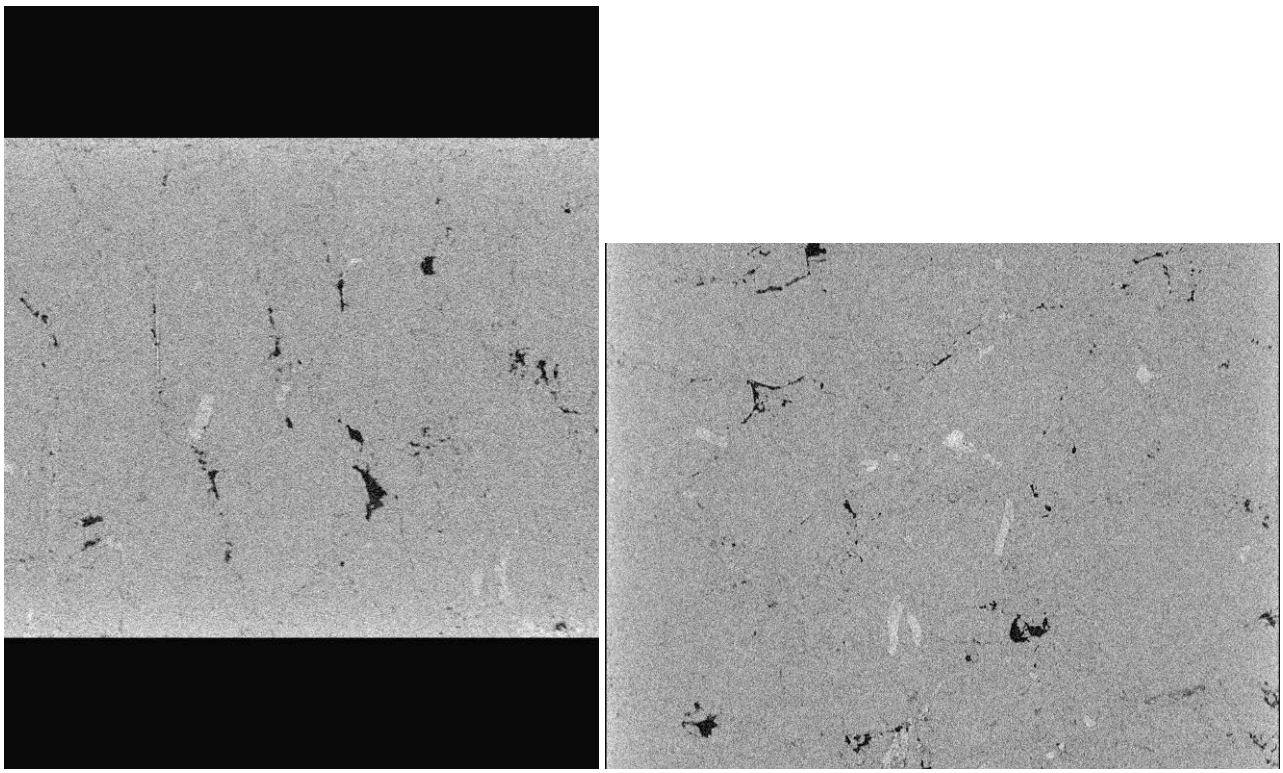

Figure 58: Orthogonal view of VD07 day 11. Image on the left: measured horizontal length is 4 mm; image on the right: measured horizontal length is 5.2 mm.

4.4.3. Discussion

Samples examined with CT-scanning offer a good insight on characteristics of cracks and their evolution and healing in salt rock. Due to technical issues, quantitative measurements were possible only on VD14 scanned at day 2 and 3 that were then compared with data obtained from the physical model. Considering the different estimate porosity of each sample, a more general overview about crack network was obtained from the remaining scans. In samples scanned at day 1-2-3 cracks are wide and irregular, some with a sub-polygonal shape and other with a more tubular shape. Grain boundaries are well developed and salt grains are clearly visible. In most of the scans and orthogonal views air bubbles and glue (used during the preparation stage) trapped in pores are clearly visible and affect the possibility of healing processes. In fact, cracks that contain glue will undergo reduction/freezing of the healing process. Different characteristics seem to dominate samples scanned at day 10-11-12 and 30, where grain boundaries are blurry and cracks look thinner, more irregular and mostly with tubular shape. In general air bubbles are absent and in few samples glue within the pores is still noticeable, but in different amount in respect to the previous. A crack network is not clearly noticeable due to the fact that cracks seem non-continuous and in some cases not connected between each other leading to think that diffusion healing might be occurred at this stage occluding pores to form more disconnected tubular inclusions and eventually isolate sub-spherical inclusions (as explained by Houben et al., 2013).

In section 4.2 we simulated the progress of crack healing in wet salt rock to estimate the velocity of the shrinking of the inclusions in rock salt, using different values for diffusion coefficient and thickness of fluid film (taken from pre-existing literature). This process gives an idea of the time in which the cusp of inclusions will migrate from the original point toward the walls by a migration distance. As shown in Table 3, the migration distance is strictly dependent on diffusion coefficient and thickness of fluid film that might enhance or reduce the crack healing. The measurements of crack healing obtained from VD14 day 2-3 provide in some cases lower values than the one obtained from the theoretical prediction using 1,96E-22 as value for DCδ/a (the best fit for the model by Houben et al., 2013, based on their crack healing experiments) and more similar to the results using a value of 7,00E-25 for DCδ/a (obtained by Koelemeijer et al., 2012). This behaviour might be due to different amount brine and consequently a different thickness of fluid film within the pore that, as said before, might enhance or reduce healing processes.

The experiments gave a good overview of crack network and crack healing in salt rock, but a deep study of the progression of the healing and its velocity during a period of 30 days was not possible. Further research is suggested to examine in deep the evolution of crack healing on compacted aggregates of granular rock salt. As a suggestion, scanning the same sample at day 1, day 10 and day

30 will give complete information about crack evolution in a period of one month. Furthermore using samples with different porosity might highlight differences in the healing process.

5. Conclusions

The aim of this project has been to explore crack evolution and healing on salt rock to estimate the timescale at which damage-induced crack porosity will seal again, and by which processes, with the purpose of using salt rock formations as storage locations for compressed air, hydrogen, natural gas and nuclear waste. Firstly, typical microstructure of intact and damaged rock salt were analysed to understand the impact of deformation on cracks within salt rock. Since salt mining induces damage to the formation and may impact the cavern sealing integrity, the thin sections were chosen in a way to have a representative example of both the undisturbed formation and the damaged area one would expect in the excavation damaged or disturbed zone (EDZ). The microstructures reveal a more dilatant behaviour in the undeformed material, proved by the presence of intergranular cracks, grain boundaries intersecting at triple junction (often at 120°) and fluid inclusions present in the whole section forming a network within the grain boundaries. Once high confining pressure is applied to the sample, the behaviour of salt rock move to non-dilatant; intergranular cracks disappear and cracks look dilated and empty as a consequence of fluid escaping. The sample developed a strong subgrain structure, showing overprints of inclusions within the grain that prove grain boundary migration. It is noticeable a general recrystallization of the grains that modified the original microstructure showing relict of old grains replaced by new recrystallized grain. The sample deformed at low pressure shows a transitional behaviour between dilatant and non-dilatant, with well-developed subgrain structure and presence of intergranular cracks and triple junctions.

The true-triaxial control experiment with wave velocity measurements on Beberthal sandstone gave an insight of microcrack development and progressive healing analysing the behaviour of wave velocities during compression. The results are consistent with previous studies and confirm that wave velocities are affected by two different processes: compaction/crack closure proved by an increase in seismic velocities and grain crushing/opening of new cracks proved by a slight decrease and a more linear behaviour. The method represents a great tool to investigate the evolution of cracks under 3D stress, but need more accuracy due to the properties of salt rock and the difficulty to operate with machines during the preparation procedure.

Insight of microcrack healing were investigated with time-lapse X-ray tomography using aggregates of granular rock salt to monitor crack healing in compacted (i.e. cracked) salt aggregates. Complementary to the CT-imaging of the salt aggregates, a model of diffusion mass transport was investigated to simulate the progress of crack healing and compare the data with the results obtained from the experiment. Scans show a different evolution of cracks: in particular, samples scanned at day 1-2-3 show wider cracks and air bubbles and resin within the pores; while samples scanned at day 10-11-12 and 30 days show non-continuous thinner cracks. A comparison between the progress of crack healing obtained from theoretical results (Table 3, section 4.2) and the ones from crack measurements from

sample VD14 (Section 4.4.2.2.1) was made to be able to recognise healing processes during CT-scanning. The comparison shows, in some cases, a lower values for crack healing that do not entirely match with theoretical values obtained using 1,96E-22 as value for DCδ/a (the best fit for the model by Houben et al., 2013), but are more similar with the results obtained using 7,00E-25 as a value for DCδ/a (used by Koelemeijer et al., 2012). Since the dependence of diffusion coefficient and thickness of fluid film on crack healing, the difference in values might be due to the different amount of brine present in pores and cracks that in some cases enhanced or reduced the healing progression.

In order to estimate with more precision the evolution and self-healing of cracks in salt rock formations, more research is needed to obtain a set of cracks measurements that can be fully compared with theoretical models. A more understanding on fluid inclusions is needed to see if and how cracks are still connected after mechanical closure and if they can still develop a network for fluid transport.

6. References

Alkan, H., Cinar, Y. and Pusch, G., 2007. Rock salt dilatancy boundary from combined acoustic emission and triaxial compression tests. *International Journal of Rock Mechanics and Mining Sciences*, *44*(1), pp.108-119.

Browning, J., Meredith, P.G., Stuart, C.E., Healy, D., Harland, S. and Mitchell, T.M., 2017. Acoustic characterization of crack damage evolution in sandstone deformed under conventional and true triaxial loading. *Journal of Geophysical Research: Solid Earth*.

Chen, J., Ren, S., Yang, C., Jiang, D. and Li, L., 2013. Self-healing characteristics of damaged rock salt under different healing conditions. *Materials*, *6*(8), pp.3438-3450.

de Meer, S., Spiers, C.J. and Nakashima, S., 2005. Structure and diffusive properties of fluid-filled grain boundaries: An in-situ study using infrared (micro) spectroscopy. *Earth and Planetary Science Letters*, *232*(3), pp.403-414.

Ding, J., Chester, F.M., Chester, J.S., Xianda, S. and Arson, C., 2017. Microcrack Network Development in Salt-Rock During Cyclic Loading at Low Confining Pressure. Georgia Institute of Technology.

Dubey, R.K. and Gairola, V.K., 2008. Influence of structural anisotropy on creep of rocksalt from Simla Himalaya, India: An experimental approach. *Journal of structural Geology*, *30*(6), pp.710-718.

Drury, M.R. and Urai, J.L., 1990. Deformation-related recrystallization processes. *Tectonophysics*, *172*(3-4), pp.235-253.

Fortin, J., Schubnel, A. and Guéguen, Y., 2005. Elastic wave velocities and permeability evolution during compaction of Bleurswiller sandstone. *International Journal of Rock Mechanics and Mining Sciences*, *42*(7), pp.873-889.

Fortin, J., Stanchits, S., Dresen, G. and Guéguen, Y., 2006. Acoustic emission and velocities associated with the formation of compaction bands in sandstone. *Journal of Geophysical Research: Solid Earth*, *111*(B10).

Fortin, J., Guéguen, Y. and Schubnel, A., 2007. Effects of pore collapse and grain crushing on ultrasonic velocities and Vp/Vs. *Journal of Geophysical Research: Solid Earth*, *112*(B8).

Hackl, K. and Ilić, S., 2005. Solution-precipitation creep—continuum mechanical formulation and micromechanical modelling. *Archive of Applied Mechanics*, *74*(11), pp.773-779.

Houben, M.E., ten Hove, A., Peach, C.J. and Spiers, C.J., 2013. Crack healing in rocksalt via diffusion in adsorbed aqueous films: Microphysical modelling versus experiments. *Physics and Chemistry of the Earth, parts A/B/C*, *64*, pp.95-104.

Hunsche, U. and Hampel, A., 1999. Rock salt—the mechanical properties of the host rock material for a radioactive waste repository. *Engineering geology*, *52*(3), pp.271-291.

Kern, H., Liu, B. and Popp, T., 1997. Relationship between anisotropy of P and S wave velocities and anisotropy of attenuation in serpentinite and amphibolite. *Journal of Geophysical Research: Solid Earth*, *102*(B2), pp.3051-3065.

Kern, H., 2011. Measuring and modeling of P-and S-wave velocities on crustal rocks: a key for the interpretation of seismic reflection and refraction data. *International Journal of Geophysics*, *2011*.

Kern, H., Popp, T., Gorbatsevich, F., Zharikov, A., Lobanov, K.V. and Smirnov, Y.P., 2001. Pressure and temperature dependence of V P and V S in rocks from the superdeep well and from surface analogues at Kola and the nature of velocity anisotropy. *Tectonophysics*, *338*(2), pp.113-134.

Kern, H., Lokajicek, T., Svitek, T. and Wenk, H.R., 2015. Seismic anisotropy of serpentinite from Val Malenco, Italy. *Journal of Geophysical Research: Solid Earth*, *120*(6), pp.4113-4129.

Koelemeijer, P.J., Peach, C.J. and Spiers, C.J., 2012. Surface diffusivity of cleaved NaCl crystals as a function of humidity: Impedance spectroscopy measurements and implications for crack healing in rock salt. *Journal of Geophysical Research: Solid Earth*, *117*(B1).

Liedtke, L. and Bleich, W., 1985. Convergence calculations for back-filled tunnels in rock salt. *Computers & Structures*, *21*(1-2), pp.353-378.

Peach, C.J., Spiers, C.J. and Trimby, P.W., 2001. Effect of confining pressure on dilatation, recrystallization, and flow of rock salt at 150 C. *Journal of Geophysical Research: Solid Earth*, *106*(B7), pp.13315-13328.

Schulze, O., Popp, T. and Kern, H., 2001. Development of damage and permeability in deforming rock salt. *Engineering Geology*, *61*(2), pp.163-180.

Spiers, C.J., Urai, J.L., Lister, G.S., Boland, J.N. and Zwart, H.J., 1986. *The influence of fluid-rock interaction on the rheology of salt rock* (No. EUR--10399). Commission of the European Communities.

Ter Heege, J.H., De Bresser, J.H.P. and Spiers, C.J., 2005. Rheological behaviour of synthetic rocksalt: the interplay between water, dynamic recrystallization and deformation mechanisms. *Journal of Structural Geology*, *27*(6), pp.948-963.

Tsang, C.F., Bernier, F. and Davies, C., 2005. Geohydromechanical processes in the Excavation Damaged Zone in crystalline rock, rock salt, and indurated and plastic clays—in the context of radioactive waste disposal. *International Journal of Rock Mechanics and Mining Sciences*, *42*(1), pp.109-125.

Urai, J.L. and Spiers, C.J., 2007, May. The effect of grain boundary water on deformation mechanisms and rheology of rocksalt during long-term deformation. In Proc. 6th Conf. Mech. Beh. of Salt (pp. 149-158).

Urai, J.L., Schléder, Z., Spiers, C.J. and Kukla, P.A., 2008. Flow and transport properties of salt rocks. *Dynamics of Complex Intracontinental Basins: The Central European Basin System*, pp.277-290.

Watanabe, T. and Peach, C.J., 2002. Electrical impedance measurement of plastically deforming halite rocks at 125 C and 50 MPa. *Journal of Geophysical Research: Solid Earth*, *107*(B1).

Wenk, H.R., Voltolini, M., Kern, H., Popp, T. and Mazurek, M., 2008. Anisotropy in shale from Mont Terri. *The Leading Edge*, *27*(6), pp.742-748.

Wong, Th.E, Batijes, D.A.J, de Jager, J, 2007. Geology of the Netherlands, pp.283-294.

Yan, F., Han, D.H., Yao, Q. and Chen, X.L., 2016. Seismic velocities of halite salt: Anisotropy, heterogeneity, dispersion, temperature, and pressure effects. *Geophysics*, *81*(4), pp.D293-D301.